

**An experimental investigation into the ‘fate’ of entrained peritectic minerals in I-type granite magmas intruded at below 2kbar.**

**By  
Sara Kathryn Zarrebini**

*Thesis presented in partial fulfilment of the requirements for the Degree of Master of Science  
at Stellenbosch University.*



Supervisor: Prof. Gary Stevens  
Faculty of Science  
Department of Earth Sciences

March 2016

## **Declaration**

By submitting this thesis/dissertation electronically, I declare that the entirety of the work contained therein is my own, original work, that I am the sole author thereof (save to the extent explicitly otherwise stated), that reproduction and publication thereof by Stellenbosch University will not infringe any third party rights and that I have not previously in its entirety or in part submitted it for obtaining any qualification.

**Date:** March 2016

## Abstract

Entrainment of a peritectic mineral assemblage, formed through the incongruent melting of biotite and hornblende in a source of intermediate composition, has been proposed to account for the fact that I-type granites are commonly more mafic in composition than the melts from which they are derived. Magma consisting of variable proportions of melt and a distinct peritectic assemblage (PI + Cpx + Opx + Ilm  $\pm$  Grt) has been proposed to explain the substantial compositional range of I-type granitic rocks. Geochemical evidence to support the entrainment of a peritectic assemblage includes the strong, positive correlation between Ti vs maficity (atomic Fe + Mg) (with correlation coefficients typically higher than 0.9 for suites from individual plutons), as well as the very weak correlation between K and maficity in all granitic rocks. Despite this compelling geochemical evidence for the entrainment of a peritectic mineral assemblage, there is distinct lack of both mineral textural and mineral compositional evidence of these peritectic phases within I-type granites. In order to ascertain the 'fate' of the proposed entrained peritectic phases; the mechanisms and reactions by which these phases equilibrate with the surrounding magma, as well as the corresponding rates of these reactions needs to be established. This research used experimental techniques to determine the kinetic processes involved in the digestion of a high-pressure peritectic assemblage within a granodioritic magma under plutonic conditions within the upper crust (~2kbar and 763 to 720°C). A synthetic silicate gel (representative of the melt fraction) was mixed with a hypothetical, natural peritectic mineral assemblage (13.1PI + 9.3Cpx + 1.1Opx + 0.8Ilm  $\pm$  5.7Grt) in a 7:3 ratio to form the experimental starting material. The peritectic mineral assemblage comprised of natural minerals of suitable compositions that were crushed and sieved to produce crystals with an average 200 $\mu$ m - 600 $\mu$ m size range. The 1.60 wt. % water within the starting composition was accommodated as kaolinite, which was added to the completed silicate gel in the correct stoichiometric proportions. The overall mineral-melt mixture was intended to represent the bulk composition of an I-type granodioritic magma produced by the fluid-absent melting of biotite and hornblende within an intermediate source composition at 10kbar and 850 - 900°C. The starting material (melt + mineral mixture) was loaded into gold capsules, which were then welded shut. The material was then reacted at pressures of 1.90kbar and 1.40kbar and at temperatures of 763 – 723°C within a cold-seal pressure vessel, with each experiment lasting 10 days. The findings of this research identified two principal reaction processes by which the high-pressure peritectic minerals react out within the experimental run products, namely; dissolution-precipitation and mineral-melt reactions. A coupled dissolution-precipitation mechanism is proposed to account for the rapid re-equilibration of 'peritectic' phases that are predicted (by phase equilibrium modelling) to be

## ABSTRACT

stable, but out of compositional equilibrium with the surrounding magma at the investigated PT conditions. 'Peritectic' plagioclase was seen to dissolve completely and reprecipitate a more albitic composition across all experimental pressure and temperature conditions, and within the experimental run-time (10 days). Consequently, a coupled dissolution-precipitation mechanism is inferred to be a sufficiently rapid and efficient process to account for the predominantly magmatic origin of feldspathic crystals within natural granitic rocks. At corresponding PT conditions, unstable mineral phases were seen to change both compositionally and texturally according to a separate reaction process, i.e. reaction with the surrounding melt portion. High pressure and temperature ferromagnesian minerals, such as garnet and orthopyroxene, which were not stable phases in the magma at the condition of the experiments were seen to react with the melt to produce reaction rims of biotite, which was a stable phase in the magma. The rapid growth rate of biotite resulting from this process suggests phaneritic textural features typically associated with granite bodies do not require long residency times to form within upper crustal magma chambers. The persistence of both garnet and orthopyroxene at the low pressure (1.40 – 1.90kbar) and temperature (763 - 720°C) conditions of experimentation indicates that at these conditions the mineral-melt reactions were too 'sluggish' to completely digest these phases. The rapid dissolution-precipitation rates of plagioclase within the experiments suggests that where garnet and orthopyroxene crystals are evident in natural granitic rocks these minerals bear no compositional or textural resemblance to the originally entrained 'peritectic' phases. The findings of this research corresponds well with the theory that I-type granites' compositional trends form as a consequence of a peritectic mineral assemblage (Pl + Cpx + Opx + Ilm ± Grt) being entrained within a leucocratic melt. However, this research has far-reaching implications in terms of other formational theories, such as; fractional crystallization, magma mixing at depth and restite entrainment, that similarly involve the production of crystal-rich magmas at depth. Regardless of which process is responsible for generating the vast compositional heterogeneity of I-type granitic rocks, if the temperature conditions of the granitic magmas remain sufficiently high (>700°C) the magma will have the propensity to either partially or fully equilibrate any crystal component that is not in equilibrium with the surrounding magma.

**Keywords:** *I-type granite, Peritectic Entrainment, Dissolution-Precipitation, Experimental*

## Uittreksel

Optel-en-meevoer van 'n peritektiese mineraal versameling gevorm deur die ongelykvormige smelting van biotiet en hornblende in 'n bron van intermediêre samestelling, was voorgestel om die I-tiepe graniet in ag te neem. Die I-tiepe graniet is oor die algemeen meer mafies in samestelling as wat smelt is. Magma bestaan uit verskillende hoeveelhede van smelt en 'n spesifieke peritektiese versameling (Pl + Cpx + Opx + Ilm ± Grt) was voorgestel om die aansienlike komposisionele reeks van I-tiepe graniet smelt te verduidelik. Geochemiese bewyse om die optel-en-meevoer van die peritektiese versameling te ondersteun sluit in 'n sterk, positiewe korrelasie tussen die Ti vs mafiese (atomies Fe + Mg) (met 'n korrelasiekoëffisiënt wat gewoonlik hoër as 0.9 is vir rock groepe van individuele plutone) asook die baie swak korrelasie tussen K en mafiese in alle graniet klippe. Ten spyte van hierdie geochemiese bewyse van die optel-en-meevoer van die peritektiese mineraal versameling, is daar 'n duidelike gebrek van bewyse vir beide mineraal tekstuur en mineraal komposisie van hierdie peritektiese fases in die I-tiepe graniet. Om die 'lot' van die voorgestelde optel-en-meevoer peritektiese fases te bepaal, moet die meganismes en reaksies van hierdie ewewigsfasies, sowel as die magma in die omliggende en hul ooreenstemmende tempos, bepaal word. Hierdie navorsing het van eksperimentele tegnieke gebruik gemaak om die kinetiese prosesse te bepaal. Die prosesse is betrokke in die vertering van 'n hoë druk perifere mineraal versameling in 'n granodioritiese magma onder plutoniese omstandighede in die boonste kors (~2kbar en 763 tot 720°C). 'n Sintetiese silikahouende gel (verteenwoordiger van die smelt fraksie) was gemeng met 'n hipotetiese, natuurlike peritektiese mineraal versameling (13.1Pl + 9.3Cpx + 1.1Opx + 0.8Ilm ± 5.7Grt) in 'n 7:3 verhouding om die eksperimentele begin materiaal te vorm. Die peritektiese mineraal versameling bestaan uit natuurlike minerale van geskikte komposisies wat vergruis en gesif was sodat die kristalle 'n gemiddeld grootte van 200µm - 600µm het. Die 1.6 wt. % water in die begin komposisie was geakkommodeer as kaoliniet, wat bygelas was om die silikahouende gel in die regte stoïgiometriese proporsies volledig te maak. Die hele mineraal mengsel was bedoel om die mederheid komposisies van 'n I-tiepe granodiorite magma voor te stel en was geproduseer by die vloeistof-afwesige smelting van biotiet en hornblende in 'n intermediêre bron komposisie by 10 kbar en 850 - 900°C. Die begin materiaal (smelt + mineraal mengsel) was in 'n goue capsule gelaai, wat dan toe gesweis was. Die materiaal het gereageer by 'n druk van 1.9 kbar en 1.4 kbar en by die temperatuur van 763 - 720°C wat in 'n koue geseëde drukvat geplaas was met elke eksperiment wat 10 dae lank geduur het. Die resultate van hierdie navorsing identifiseer twee beginsel reaksie prosesse, ontbinding-neerslag en minerale-smelt hidrasie reaksies, waar die hoë druk peritektiese minerale reageer in die eksperimentele resultate. 'n Gekoppelde oplossings-presipitasie meganisme is voorgestel om die vinnige herewegingsproses van peritektiese fases in ag te neem wat voorspel is (deur fase ewewig modellering) om stabiel te wees, maar uit komposisionele ewewig saam met die magma in die omliggende gebied by die ondersoekte PT

## UITTREKSEL

omstandighede. Peritektiese plagioklaas was gesien en het heeltemal opgelos en neerslag 'n meer albeitiese komposisie oor al die eksperimentele druk en temperatuur omstandighede, asook in die eksperimentele looptyd (10 dae). Gevolglik is 'n gekoppelde oplossings-presipitasie meganisme afgelei as 'n effektiewe proses teen voldoende tempo om die oorwegende magmatiese oorsprong van feldspatiese kristalle in natuurlike graniet klip waar te neem. By ooreenkomstige PT omstandighede was daar onstabiele mineraal fases gesien wat volgens die afsonderlike reaksie fase in beide komposisionele en teksturele minerale verander het, bv. reaksies met die omgewind smelt proporsies. Hoë druk en temperatuur minerale met hoë Fe en Mg konsentrasies, soos granaat en ortopirokseen, was nie in stabiele fases in die magma by die omstandighede van die eksperiment nie en waargeneem dat dit reageer met die smelt om reaksie rande van 'n stabiele biotiet fases te vorm. Dit was waargeneem dat ortopirokseen in laer druk eksperimente (1.40 kbar) reageer met die omliggende smelt proporsie om biotiet vervang ortopirokseen te vorm teen 'n spoed van omtrent vier keer stadiger as die herewewig van peritektiese plagioklaas by die oplossings-presipitasie proses. Die vinnige groeitempo van biotiete, as gevolg van hierdie proses, stel voor dat 'phaneritic' teksturele funksies wat tipies geassosieer word met graniet liggame, vereis nie lang verblyf tye om te vorm in die boonste kristal magma kamers nie. Die volharding van beide granaat en ortopirokseen by die lae druk (1.40 – 1.90kbar) en temperatuur (763 - 720°C) omstandighede van eksperimentasie toon dat by hierdie omstandighede van eksperimentasie die mineraal-smelt hidrasie reaksies was te traë om volledig te verteer in hierdie fases. Die vinnige oplossings-presipitasie tempos van plagioklaas in die eksperimente dui duidelik aan dat granaat en ortopirokseen kristalle in natuurlike graniet klippe is. Hierdie minerale hou geen komposisionele of teksturele ooreenkoms met die oorspronklike opgetel en weggedra peritektiese fases nie. Die resultate van die navorsing stem goed ooreen met die teorie dat I-tiepe graniete komposisionele tendense vorm as 'n gevolg van 'n peritektiese mineraal versameling (Pl + Cpx + Opx + Ilm ± Grt) wat opgetel en weggedra is in 'n leukokratiese smelt. Maar hierdie navorsing het verreikende gevolge in terme van ander magmatiese teorieë, bv. fraksionele kristallisering, magma vermenging in diepte en die optel-en-meevoer van die oorblywende minerale uit die bron, wat soortgelyk die produksie van kristalryk magmas in diepte insluit. Ongeag van watter van hierdie prosesse verantwoordelik is vir die generering van die oorgrote komposisionele heterogeniteit van I-tiepe graniet klippe, as die temperatuur omstandighede van die graniet magmas by voldoende hoë hoeveelhede bly (>700°C), dan sal die magma die geneigdheid hê om gedeeltlik of heeltemal ewewig te bereik met enige kristal komponent wat nie in komposisionele ewewig met die omliggende magma is nie.

**Sleutelwoorde:** *I-tipe granaat, Peritektiese Optel-en-Meevoer, Oplossings – Presipitasie, Eksperimentele*

## **Acknowledgements**

This research was funded by the South African National Research Foundation (NRF) in the form of grant funding to Professor Gary Stevens via the SARChI programme and an MSc bursary to Sara Zarrebini. Gautier Nicoli provided the Limpopo granulite samples from which the 'peritectic' minerals utilized within this research were obtained.

I would like to extend my sincerest thanks and appreciation to my supervisor, Professor Gary Stevens for guiding me through the last three years of my academic career. Your mentorship, patience, and insights into the granite topic were paramount in the completion of this thesis.

## Table of Contents

Declaration.....	i
Abstract.....	ii
Uittreksel.....	iv
Acknowledgements.....	vi
List of Figures .....	ix
List of Tables .....	ix
List of Abbreviations.....	x
Chapter 1: Introduction.....	1
Chapter 2: I- vs. S-type Granites .....	4
2.1 A Geochemical Perspective.....	5
2.1.1 Major Element Chemistry.....	10
2.1.2 Trace Element Chemistry.....	12
2.2 Geodynamic Environments.....	14
Chapter 3: Explaining Granite Geochemistry.....	16
3.1 Compositional Variation of Granitic Melts .....	16
3.1.1 Chemical Heterogeneity in the Source .....	16
3.1.2 Pulsed Melt Extractions from a Progressively Melted Source.....	16
3.2 Models of Formation .....	17
3.2.1 Source Inheritance Models .....	17
3.2.2 Magma-Mixing .....	24
3.2.3 Assimilation .....	26
3.2.4 Fractional Crystallization .....	27
3.3 Concluding Remarks .....	28
Chapter 4: Experimental Design.....	29
4.1 Analytical Techniques.....	30
4.2 Phase Equilibrium Modelling – <i>A Rationale of Experimental Techniques</i> .....	31
4.3 Experimental Methodology .....	38



Chapter 5: Results.....	47
5.1 Mineral and Melt Compositions.....	48
5.2 Textures in the Experimental Run Products.....	61
5.3 Mineral and Textural Descriptions.....	67
Higher Pressure Experiments (1.90kbar) .....	67
Lower Pressure Experiments (1.40kbar) .....	74
Chapter 6: Discussion and Interpretation.....	78
6.1 Non-Equilibrium Studies .....	78
6.2 Mineral Kinetic Processes .....	80
6.2.1 Dissolution-Precipitation Mechanism.....	80
6.2.2 Mineral-Melt Reactions.....	89
6.3 Melt Compositions .....	98
6.4 Phase Equilibrium Modelling vs. Experimental Findings .....	101
6.5 Implications for Natural Systems .....	111
Chapter 7: Conclusions and Recommendations.....	115
7.1 Conclusions.....	115
7.2 Summary of Contributions .....	115
7.3 Future Research.....	116
References .....	117
Appendix.....	123

## List of Figures

Figure 1 - Major and Trace Element Compositional Arrays for I- and S-type Granitic Rock Suites .....	7
Figure 2 - Chondrite Normalized REE Plots .....	8
Figure 3 - Trace Element Spidergram .....	9
Figure 4 - Pseudosection 1 .....	34
Figure 5 - Pseudosection 2 .....	35
Figure 6 - Photograph of the Experimental Machinery.....	42
Figure 7 - Schematic of the Standard Cold-Seal Pressure Vessel Set-up.....	43
Figure 8 - Cross-section of Inconel vessel (Calibration Experiment – Test 2).....	45
Figure 9 - Side profile of Inconel vessel base (Calibration Experiment – Test 2) .....	46
Figure 10 - BSE SEM Images Experiment 1 (1.90kbar; 733°C).....	62
Figure 11 - BSE SEM Images Experiment 2 (1.90kbar; 763°C).....	63
Figure 12 - BSE SEM Images Experiment 3 (1.90kbar; 723°C).....	64
Figure 13 - BSE SEM Images Experiment 4 (1.40kbar; 743°C).....	65
Figure 14 - BSE SEM Images Experiment 5 (1.40kbar; 730°C).....	66
Figure 15 - Schematic of Dissolution - Precipitation Mechanism in Plagioclase .....	80
Figure 16 - Plagioclase Hypersolidus Stability Fields for an Average I-type Granitic Magma Composition.....	81
Figure 17 - Clinopyroxene Hypersolidus Stability Fields for an Average I-type Granitic Magma Composition.....	85
Figure 18 - Theoretical Dissolution Rates for 'Peritectic' Plagioclase .....	87
Figure 19 - Schematic of Reaction between Garnet and Melt to Produce Biotite .....	89
Figure 20 - Garnet Hypersolidus Stability Fields for an Average I-type Granitic Magma Composition. ....	92
Figure 21 - Orthopyroxene Hypersolidus Stability Fields for an Average I-type Granitic Magma Composition.....	97
Figure 22 - Bivariate Plots of Melt Major Element Compositions .....	98
Figure 23 - Modelled vs. Experimental Mineral Assemblages .....	102

## List of Tables

Table 1 - Synthetic Silicate Melt Composition .....	39
Table 2 - Peritectic Mineral Assemblage Bulk Composition.....	40
Table 3 - Starting Bulk Composition .....	40
Table 4 - Calibration Experiment Results (Test 1).....	44
Table 5 - Calibration Experiment Results (Test 2) .....	45
Table 6 - Experimental PT Conditions and Mineral Assemblages .....	47
Table 7 - Peritectic Assemblage Mineral Compositions .....	48
Table 8 - Experiment 1 Average Mineral Compositions.....	50
Table 9 - Experiment 2 Average Mineral Compositions.....	52
Table 10 - Experiment 3 Average Mineral Compositions.....	54
Table 11 - Experiment 4 Average Mineral Compositions.....	56

<b>Table 12 - Experiment 5 Average Mineral Compositions</b> .....	<b>58</b>
<b>Table 13 - Experimental Melt Average Compositions</b> .....	<b>60</b>
<b>Table 14 - Mineral Assemblage Summary</b> .....	<b>103</b>
<b>Table 15 - Predicted vs. Experimental Mineral Volume Percentages</b> .....	<b>105</b>
<b>Table 16 - Predicted vs. Experimental Mineral Compositions (1.90kbar)</b> .....	<b>109</b>
<b>Table 17 - Predicted vs. Experimental Mineral Compositions (1.40kbar)</b> .....	<b>110</b>

## List of Abbreviations

### Mineral Abbreviations

<b>Grt</b>	Garnet
<b>Cpx</b>	Clinopyroxene
<b>Bt</b>	Biotite
<b>Cam</b>	Clinoamphibole
<b>Opx</b>	Orthopyroxene
<b>Qtz</b>	Quartz
<b>Pl</b>	Plagioclase
<b>Ilm</b>	Ilmenite
<b>Spn</b>	Sphene
<b>Rt</b>	Rutile
<b>Hbl</b>	Hornblende
<b>Alm</b>	Almandine Garnet
<b>Pyr</b>	Pyrope Garnet
<b>Grs</b>	Grossular Garnet
<b>Sps</b>	Spessartine Garnet

**\*Mineral Abbreviations based upon Whitney and Evans, 2010.**

### General Abbreviations

<b>SEM</b>	Scanning Electron Microscope
<b>XRD</b>	X-ray Diffraction
<b>XRF</b>	X-ray Fluorescence
<b>BSE</b>	Backscattered Electron Image
<b>PAE</b>	Peritectic Assemblage Entrainment

## Chapter 1: Introduction

Granitic magmas, from which granites of average to mafic compositions are derived, are undoubtedly mixtures of crystals and melt throughout their magmatic history (Clemens et al., 2011; Clemens and Stevens, 2012; Stevens et al., 2007; Villaros et al., 2009a; White and Chappell, 1977). These granitic magmas are formed by the fluid-absent, incongruent melting of hydrous minerals, such as micas and amphiboles within their lower crustal sources (Clemens, 2012; Clemens and Vielzeuf, 1987; Thompson and Connolly, 1995). The aforementioned process has enabled the melt compositions of granitic magmas to be well constrained by experiments (e.g., Stevens et al., 2007). In particular, the analysis of natural melt inclusions in peritectic minerals within anatectic granulites (Taylor and Stevens, 2010), and quenched melts from experimental studies (e.g., Montel and Vielzeuf, 1997), have shown granitic melt compositions to typically be more leucocratic in composition than average granites (Montel and Vielzeuf, 1997; Stevens et al., 2007; Taylor and Stevens, 2010). Even at the highest inferred temperatures of crustal anatexis (~1000°C), the melts produced by incongruent melting reactions would be too silicic to produce mafic granites, such as common granodiorites (Clemens et al., 2011 and references therein). This, along with the fact that granites are typically enriched in compatible elements, such as Mg, Fe, Ca, Ti etc. over experimental melts and natural melt inclusions suggests that petrogenetic processes that involve a crystal-rich granitic magma are able to account for the formation of granite compositions that lie towards the mafic end of the compositional spectrum (Clemens et al., 2011). The aforementioned is implicit in the leucocratic character of granitic melts (Montel and Vielzeuf, 1997; Stevens et al., 2007; Taylor and Stevens, 2010). Where granites are more mafic in composition than the melts from which they are derived they must exist as a combination of melt and crystals '*throughout*' their magmatic history.

Theories that revolve around the concept of deeper crustal, crystal-bearing magmas intruding to higher levels include; restite entrainment (Chappell et al., 1987), peritectic mineral entrainment (Clemens and Stevens, 2012; Clemens et al., 2011; Stevens et al., 2007; Villaros et al., 2009a), magma mixing at depth (e.g., Chappell, 1996; Karsli et al., 2010; Vernon, 2007; Zorpi et al., 1989) and fractional crystallization at depth (e.g., Soesoo, 2000). Each of these hypotheses has been met with varying levels of contention within the literature. It should be noted at this point that it is not the goal of this research to argue against the validity of any of the above hypotheses. This research is instead seen to have general applicability within all of these aforementioned petrogenetic processes, as it aims to determine the 'fate' of the high temperature mineral assemblage within an I-type magma as it cools following ascent. The peritectic assemblage entrainment (PAE) model has been utilized as the basis for this

## CHAPTER 1: INTRODUCTION

research over the other aforementioned hypotheses, because it is both simple and quantifiable in terms of the amount of entrained residuum that is required to produce a relatively mafic granite composition. Its usage is further supported by its unique ability to successfully recreate distinct geochemical trends that can be observed within all granitic rock varieties, specifically the strong positive correlation between Ti and maficity (atomic Fe+ Mg) (Clemens and Stevens, 2012; Steven et al., 2007).

It is the entrained peritectic mineral phases that are proposed to be one of the primary controls in producing the geochemical heterogeneity of granitic rocks (Clemens and Stevens, 2012; Stevens et al., 2007). In the case of I-type granitic rocks the strong positive correlation between Ti, Mg#, Ca and maficity can largely be ascribed to the entrainment of peritectic clinopyroxene, ilmenite and plagioclase (Clemens et al., 2011). And yet, there is little to no textural or compositional evidence of these high pressure and temperature minerals within the crystallized assemblages of granitic rocks (Clemens et al., 2011; Clemens and Stevens, 2012; Clemens and Wall, 1988; Vernon et al., 2009). Instead, granites appear to consist largely of crystals that are magmatic in nature (Clemens and Stevens, 2012; Vernon, 2010). This is a key observation, which raises the question as to why granitic rocks typically do not display textural or mineral compositional evidence of the entrained residuum, peritectic minerals or the early formed high temperature magmatic phases that are implied to exist by the various granite petrogenetic processes.

In order to understand the 'fate' of the entrained residuum, peritectic minerals or the early formed high temperature magmatic phases, it is essential to understand the kinetics of the reactions by which they may equilibrate. Entrained residuum is not necessarily in equilibrium with the surrounding magma at the point of magma segregation. Partial melting of the source rocks is able to produce both spatially, temporally and geochemically distinct batches of granitic melts (McLeod et al., 2012), which result from sequentially higher temperature melting reactions within the source material (Clemens and Stevens, 2012). At the point of magma segregation the effective bulk composition is altered such that equilibrated phases within the residuum are likely out of equilibrium with the segregated magma. The residuum produced in one melting episode is therefore likely to be in both major and trace element disequilibrium with the melt and residuum produced by a later melting event within the source. The system responds to this disequilibrium by attempting to reduce its Gibbs energy, and in doing so is able to spontaneously move in the direction of equilibrium (Giddings, 1991; Zhu and Anderson, 2002). Equilibrium is attained within the natural granitic system either through the complete re-equilibration of entrained minerals to the composition and pressure-temperature conditions of the surrounding magma (Clemens and Stevens, 2012; Clemens et al., 2011; Villaros et al., 2009a). According to the literature, mineral phases, such as garnet, are able to equilibrate

rapidly and efficiently within ascending granitic magmas according to a simultaneous dissolution-precipitation mechanism (Villaros et al., 2009a). Although Villaros et al., (2009) determined that as the temperatures and melt volumes of the cooling magma decreases, so does the efficiency of the dissolution-precipitation mechanism to re-equilibrate the entrained phases to the surrounding magmatic conditions. During magma ascent and corresponding crystallization the activities of both H<sub>2</sub>O and K<sub>2</sub>O are raised within the melt which allows for anhydrous minerals, such as garnet and orthopyroxene, to be partially/completely replaced by hydrous minerals; such as hornblende and biotite (Clemens et al., 2011). It is these aforementioned dissolution-precipitation and mineral-melt reaction processes that are proposed to be responsible for the textural and compositional destruction of the original, entrained residuum within granitic magmas emplaced at upper crustal levels.

In spite of granite's global presence and the abundance of research on granitic rocks, little is understood about the kinetic processes involved in their magmatic evolution during their ascent and later emplacement at higher crustal levels (Kemp et al., 2007). Furthermore, the processes and reactions that are responsible for producing the equilibrium mineral assemblages of I-type granitic rocks remain enigmatic. In order to resolve some of these outstanding uncertainties, this study takes an experimental approach to determine the 'fate' of entrained peritectic minerals within an I-type granite magma that is emplaced 'instantaneously' within an upper crustal magma chamber. The research will look to analyse and quantify the compositional and textural changes experienced by an entrained 'peritectic' mineral assemblage at the approximate granulite facies conditions of the magma's emplacement (~2 kbar and ~800°C). The appositeness of a coupled 'dissolution-precipitation' mechanism, as well as mineral-melt reactions, to either partially/fully equilibrate various entrained 'peritectic' phases within an I-type granite magma will be evaluated. Finally, comparisons between phase equilibrium modelling and experimental datasets will be made to determine the relative degree of equilibration within the experimental run products.

## Chapter 2: I- vs. S-type Granites

The term 'granite', *sensu stricto*, describes a broad group of felsic, intrusive igneous rocks that are typically characterised by mineral assemblages of quartz ( $\geq 20\%$ ) and feldspars ( $\geq 40\%$  alkali), and to a lesser degree amphiboles and micas (Clemens, 2012). However, this research defines 'granites', *sensu lato*, including more mafic varieties, such as common granodiorites, within its definition. Petrological examination of granitic rocks around the globe has shown their compositions to vary substantially on both a metre to kilometre wide scale (Clemens and Stevens, 2012). It is this substantial range in granite compositions that has prompted the development of various granitic classification systems (see Barbarin, 1999; Chappell and White, 1974).

I- and S-type granites are subsets of the alphabetical classification system developed by Chappell and White (1974) after a ground-breaking study into the Palaeozoic batholiths of the Lachlan Fold Belt (south-eastern Australia). The prefixes 'I' and 'S' denote the terms 'igneous' and 'sedimentary' respectively, and were intended by Chappell and White to describe the types of sources from which the granites formed (Chappell, 1999; Chappell and White, 1974).

Noteworthy examples of I-type granite outcrops include; the Lachlan Fold Belt (Australia), the Cape Granite Suite (South Africa), the Eastern Cordilleras (Columbian Andes) and Cordilleran granites of western North America (Sierra Nevada, California). Consequently, the locality of I-type granites appears to be largely restricted to areas associated with lithospheric subduction, such as continental arcs (Athari et al., 2007; Barbarin, 1999; Clemens and Stevens, 2012; Pearce, 1996). Accordingly, their protoliths are thought to be arc volcanic rocks of intermediate composition, such as dacites/andesites (Castro, 2014; Chappell et al., 1998; Clemens et al., 2011). In contrast, S-type granites are typically associated with syn-collisional environments (Barbarin, 1999; Pearce, 1996; Pearce et al., 1984). Their protoliths are suggested to be sedimentary in origin, such as metapelites and metagreywackes (Clemens et al., 2011).

## 2.1 A Geochemical Perspective

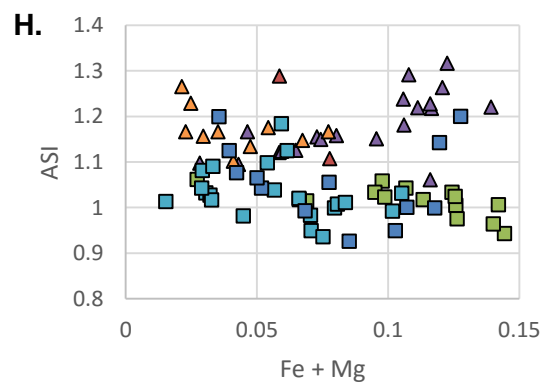
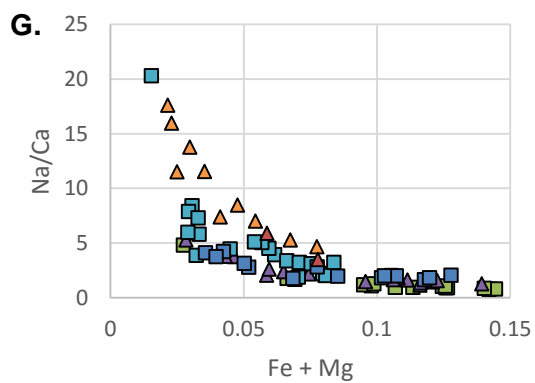
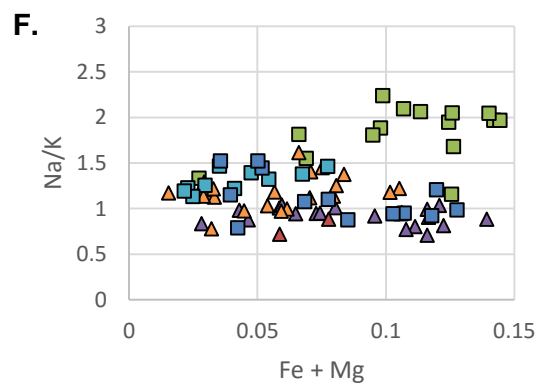
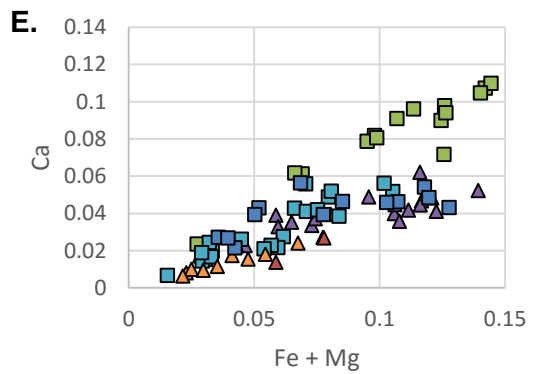
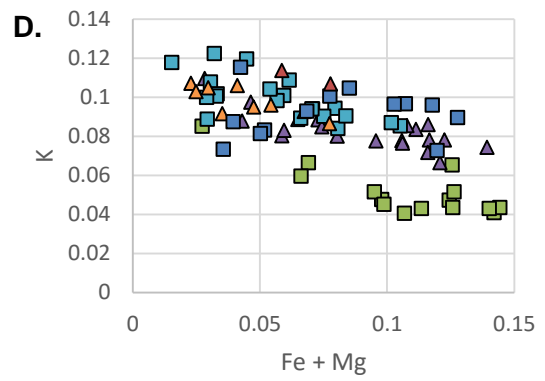
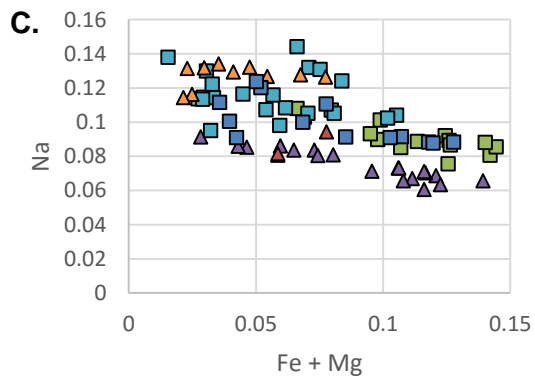
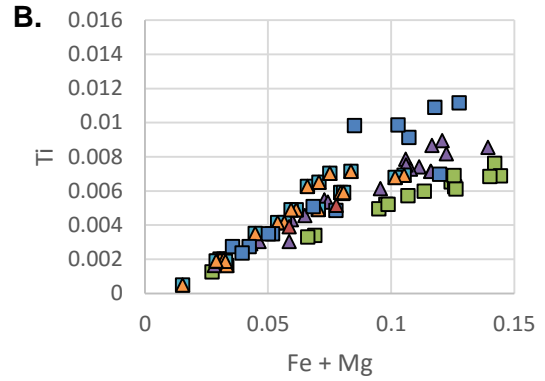
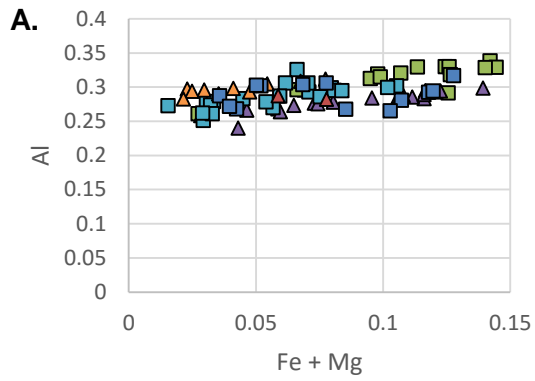
Numerous studies have been conducted on both I-and S-type granites around the world. These studies range from stable isotopic studies, field observations and petrological experiments to theoretical modelling. Each one of these studies forms an integral piece in the on-going attempt by the geological community to understand the greater puzzle that is granite genesis.

The following figures provide the reader with a visual representation of the geochemical differences between studied I- and S-type granite suites across South America, Europe and Australia. The I-type granites are represented by squares, whilst the S-type granites are denoted by triangles. The data used to create the graphs has been compiled from the literature (Almeida et al., 2007; Antunes et al., 2008; Hine et al., 1978; Villaseca et al., 2009). For the purposes of consistency attempts have been made to ensure that the majority of each suites' data is from a single source. A comprehensive discussion relating the graphical data to a broader literature base can be found after the diagrams.

### LEGEND

-  Kosciusko Batholith (I-type Granites)
-  Kosciusko Batholith (S-type Granites)
-  Iberian Massif (I-type Granites)
-  Castelo Branco (S-type Granites)
-  Martins Pereira (I-type Granites)
-  Serra Dourada (S-type Granites)
-  Berridale – Kosciusko Batholith (I-type Granites)
-  Berridale – Kosciusko Batholith (S-type Granites)
-  Cooma Batholith (S-type Granites)





CHAPTER 2: I- VERSUS S-TYPE GRANITES

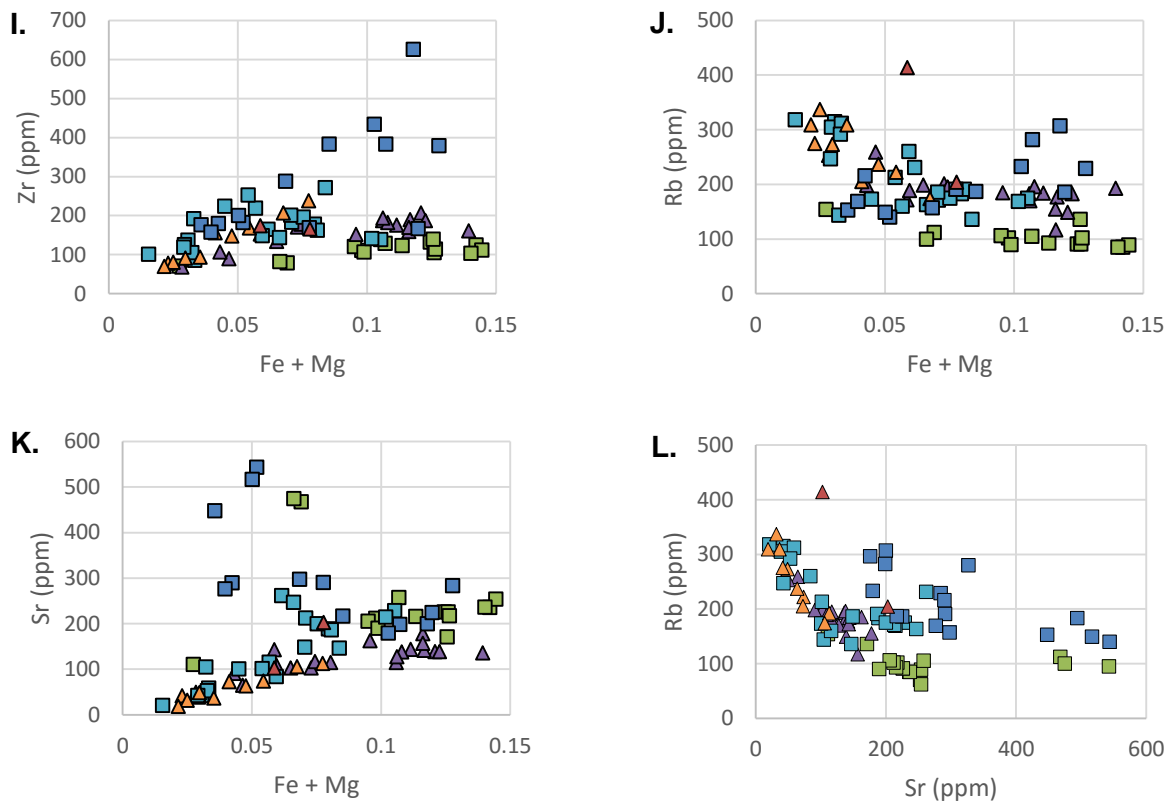


**Figure 1 - Major and Trace Element Compositional Arrays for I- and S-type Granitic Rock Suites**  
 Figures A-H are plots of various major element/element ratios versus maficity (atomic Fe + Mg per 100g of rock). Figures I-K are plots of trace elements against maficity. Figure L is a trace element plot of Rb versus Sr.

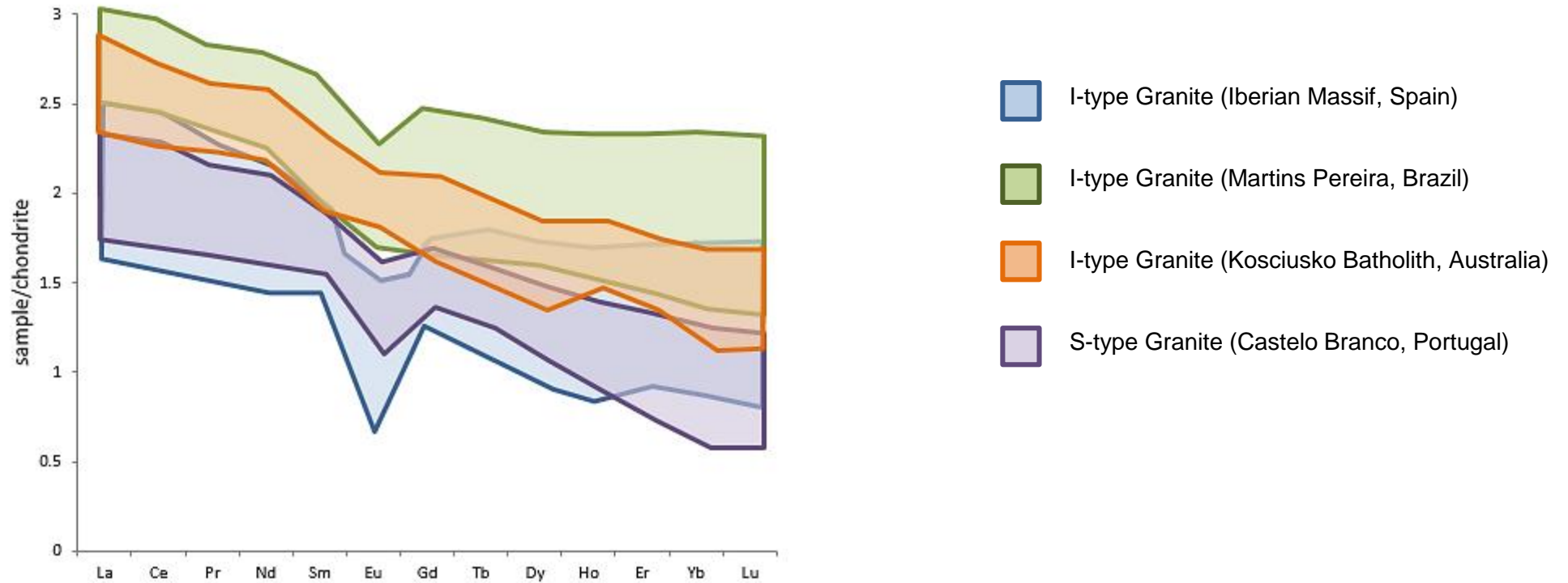


**Figure 2 - Chondrite Normalized REE Plots**

Each colour region represents the overall range in REE values within an individual suite of rocks. Normalization standard is CI Chondrite taken from McDonough and Sun, 1995. The y-axis of the graph denotes the log of the sample values obtained from the literature. As ratios are typically asymmetric, the log of the sample values have been taken in an attempt to restore normality to the data.

CHAPTER 2: I- VERSUS S-TYPE GRANITES

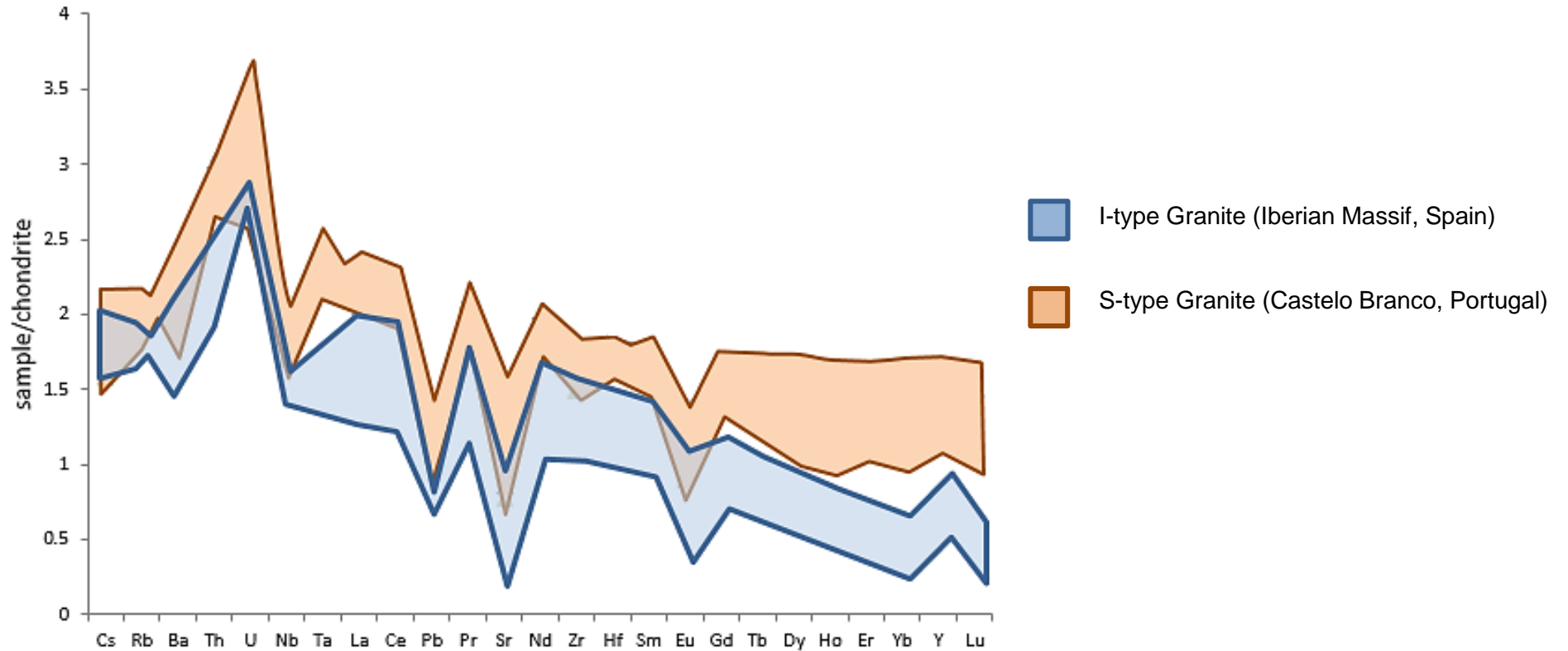


**Figure 3 - Trace Element Spidergram**

Each colour region represents the overall range in Trace Element values within an individual suite of rocks. Normalization standard is CI Chondrite taken from McDonough and Sun, 1995. The y-axis of the graph denotes the log of the sample values obtained from the literature. As ratios are typically asymmetric, the log of the sample values have been taken in an attempt to restore normality to the data.

### 2.1.1 Major Element Chemistry

I-type granites are typically metaluminous ( $A/CNK < 1$ ), and appear to range in composition from mafic granodiorites to leucogranites (Clemens et al., 2011). These rocks are characterised by a mineral assemblage which includes: biotite  $\pm$  hornblende, with accessory sphene and magnetite. Hornblende-bearing I-type granitic rocks can also contain clinopyroxene within their assemblages (Brown, 2013; Clemens et al, 2011; Nédélec et al., 2015). S-type granitic rocks are peraluminous ( $A/CNK > 1$ ), and can range in composition from mafic tonalities to leucogranites (Clemens, 2003). Although described as 'two-mica' bearing granites, S-type granites are far more mineralogically diverse (Clemens and Wall, 1988) and can contain an array of minerals including: muscovite  $\pm$  biotite, garnet, cordierite, aluminosilicates (andalusite/sillimanite), corundum, spinel, tourmaline and quartz (Clarke, 1981).

Geochemical analysis of exposed granitic rocks indicates that I-type granites are generally more sodic than their S-type granite counterparts that are commonly potassium- rich (Brown, 2013). I-type granites lying towards the felsic end of the compositional spectrum contain  $>3.2$  wt. %  $\text{Na}_2\text{O}$ , whilst more mafic I-type granites contain  $>2.2$  wt. %. In general I-type granites typically have 3.5-5.5 wt. %  $\text{K}_2\text{O}$  (Clemens et al., 2011) It has been suggested that the partial melting of hydrous, calc-alkaline to high-K calc-alkaline metamorphic rocks are appropriate to produce high-K I-type granite magmas. Whilst metabasaltic rocks are considered to be unsuitable protoliths as they contain insufficient  $\text{K}_2\text{O}$  (Roberts and Clemens, 1993). Clemens et al., (2011, pg. 175) also propose that basaltic protoliths produce melts that are too sodic to produce even "medium K-series" granitic magmas. Potassic-rich ( $\text{K}_2\text{O} \sim 5$  wt. %) S-type granite rocks have  $\text{Na}_2\text{O}$  values  $<3.2$  wt. %, whilst those with lower  $\text{Na}_2\text{O}$  values of  $<2.2$  wt. % typically have  $\text{K}_2\text{O}$  values of 2 wt. % (Chappell and White, 2001). Figure 1 (F) (pg. 6) demonstrates that at lower maficity values ( $<0.1$ ) there is an overlap in the Na/K values for both the I- and S-type rock suites.

Another important contrast between the two granite types relates to the Aluminum Saturation Index (ASI). Relatively leucocratic I-type granites are weakly peraluminous (ASI value  $> 1.0$ ), becoming increasingly metaluminous (ASI value  $< 1.0$ ) with increasing maficity (Fe + Mg) (Clemens et al., 2011). Whilst their comparatively leucocratic S-type granite counterparts are moderately to strongly peraluminous resulting in an ASI value typically above 1.1 (Clemens et al., 2011; Harris et al., 1997). Analysis of both I- and S-type granites demonstrated an overlap in ASI values between the two granite types. It is here that Clemens et al., (2011) postulate that the similarity in ASI value equates to a closeness in composition between the two granites' parental melts. The similarities in ASI values as proposed by Clemens et al., (2011) are supported by Figure 1(H) (pg. 6) developed in the section above. In this graph the ASI value

## CHAPTER 2: I- VERSUS S-TYPE GRANITES

is seen to range narrowly between 1.0 and 1.3 for the most leucocratic rocks within the chosen I- and S-type granitic suites.

By analysing the bulk geochemistry of granites, Clemens et al., (2011) established there is a positive correlation between increasing maficity (Fe + Mg) and increasing metaluminosity within I-type granites. They attribute this relationship to the entrainment of the peritectic mineral assemblage, specifically clinopyroxene, which results from the incongruent melting of hornblende (Clemens et al., 2011). This is illustrated within Figure 1 (H) (pg. 6) where the I-type granites of the Kosciusko Batholith show a weak, negative trend between maficity and ASI, with a coefficient of determination equal to 0.60. At the lowest recorded maficity value (0.03) for this suite the corresponding ASI value is 1.04, whilst at the highest maficity value (0.14) the corresponding ASI value is lower at 0.94. Conversely the S-type granites of the Kosciusko Batholith are shown to have a slightly weaker, but positive correlation with a coefficient of determination equal to 0.45. The S-type trend is inferred to be a consequence of the entrainment of peritectic garnet, ilmenite ± orthopyroxene within the melt (Stevens et al., 2007).

Clemens et al., (2011) also determined there to be a strong positive correlation between Ti and maficity in both I- and S-type granites. This relationship can be observed in Figure 1 (B) (pg. 6). All suites within this graph show high correlation coefficients ranging from between 0.91 (Martins Pereira, I-type granites) to 1.00 (Serra Dourada, S-type granites). The coefficient of determination for the suites is similarly high ranging from 0.79 (Martins Pereira I-type granites) to 0.94 (Kosciusko Batholith S-type granites). As these values are not ideal (i.e.  $R^2 = 1$ ), the difference between the actual  $R^2$  value and the ideal  $R^2$  value indicates that the change in ASI values (dependent variables) are not solely a consequence of the change in maficity (independent variables). In the case of the Martin Pereira I-type granites approximately 21% of the variation in Ti is unaccounted for by the change in maficity, and can thus be ascribed to factors other than maficity. However, in the case of the Kosciusko S-type granites the variation in Ti content within the rocks can be ascribed largely to the change in maficity, as the  $R^2$  value is significantly closer to unity. At lower maficity values (<0.07) the Ti versus maficity trends for both I- and S-type suites appear to be positioned closely around the regression line, whilst at higher maficity contents (>0.07) there appears to be greater dispersion of the values particularly within the I-type suites (Kosciusko Batholith and Martins Pereira). The strong Ti versus maficity trend observed in the S-type granite suites is a direct result of the entrained peritectic mineral assemblage mimicking the stoichiometry of the biotite only melting reaction (Clemens et al., 2011). The greater dispersion of Ti values in I-type granites at higher (>0.07) maficities can be ascribed to the fact that their magmas are formed from the incongruent melting of both biotite and hornblende (Clemens et al., 2011). The

different trend lines seen in various I-type granite suites (see Kosciusko Batholith and Martins Pereira) result from the differing proportions of biotite to hornblende within their sources (Clemens, 2012). These behaviours are unlikely to arise from restite entrainment or mixing with mantle derived magmas, as these processes would generate highly variable Ti:maficity ratios across compositionally different granitic rocks (Clemens et al., 2011).

Clemens et al., (2011) also noted a weak, negative relationship between K and maficity in both granite types, which can be seen clearly in Figure 1(P) on page 7. This weak trend is ascribed to the fact that K is soluble within the melt and its concentration is dependent on the solubility and proportion of the feldspathic material within the protolithic material (Clemens et al., 2011; Clemens and Stevens, 2012).

Major element isotopes studies have proven to be useful tools to differentiate between I- and S-type granites (O'Neil and Chappell, 1977). A study conducted by the University of Cape Town examined the oxygen and hydrogen isotope geochemistry of the I- and S-type granites of the Cape Granite Suite (CGS) (Harris et al., 1997). Their aim was to see if distinct differences between the two granite subgroups did in fact exist. The I-type granites of the suite were determined to have  $\delta^{18}\text{O}$  values of between 6.6 and 9.9‰ for quartz, whereas the S-types were found to have between 9.5 and 11.4‰. From this it was determined that the  $\delta_{\text{magma}}$  values for I-type granites were lower than those observed in S-type granites. These noticeable differences, with minimal overlap, suggest that the I- and S- type granites of the CGS formed from different, distinct protoliths. It is still unclear from the study the exact source of the I-type granites within the region. However, the authors interpreted the average oxygen isotope value of 7.8‰ to imply a meta-igneous source (Harris et al., 1997). This interpretation corresponds well with Chappell and Whites' (1974) initial surmising of I-type granites being derived from meta-igneous sources.

### 2.1.2 Trace Element Chemistry

Stable isotope studies can also provide valuable insight into the nature of I- and S-type granite protoliths. McCulloch and Chappell conducted a stable isotope study comparing the Nd and Sr isotope characteristics of the I- and S- type granites found within batholiths of the Lachlan Fold Belt. Each granite type has a distinct range of initial  $^{87}\text{Sr}/^{86}\text{Sr}$  values; with I-types having a range of values between 0.70453 and 0.71119. This was far more restricted than the  $\epsilon_{\text{Nd}}$  values which vary significantly between 0.4 to -8.9. The authors hypothesize that the variation in Sr and Nd values for the studied I-type granites indicates multiple protoliths of varying ages. Age calculations on the I-type granites showed that they formed from a mantle-derived crust that was produced ~ 1000 Ma before partial melting began to produce the granites (McCulloch & Chappell, 1982). Both the  $\epsilon_{\text{Nd}}$  and  $^{87}\text{Sr}/^{86}\text{Sr}$  values for S-type granites differ considerably

from the I-types. S-type granites have a range of  $\epsilon_{Nd}$  values of between -6.1 to -9.2, and a range of initial Sr values of 0.7094 to 0.7184. In regards to the S-type granites they attributed the variation to; differential amounts of chemical weathering of the protoliths, along with the overall maficity concentration within the protoliths (McCulloch & Chappell, 1982). Attempts were made to find stable isotope studies that provide major element data in order to establish the relationship between  $^{87}Sr/^{86}Sr$  and maficity in both I- and S-type granitic rocks. The accessible literature did not include both of the aforementioned datasets for individual rock suites, which is why this data was not included in the major and trace element arrays (Figure 1, pg. 6 - 7).

Accessory minerals are also a key feature that differentiate I- and S- type granites. Inherited zircons, along with monazite, apatite and xenotime are typically more prevalent in S-type granites (Broska, 2003; Villaros et al., 2009a); whilst I-types are commonly characterised by allanite, apatite and sphene (Broska, 2003). Inherited zircons demonstrate unequivocally that granites entrain components of their sources (Clemens and Stevens, 2012). According to the literature, both granitic types show a reasonably strong Zr-maficity relationship. However, in the maficity graphs (Figure 1, pg. 6- 7) the relationship appears weakly positive. Even though I-type granites usually contain fewer inherited zircons, they can sometimes display higher Zr concentrations than their S-type equivalents (Clemens et al., 2011). Zircon solubility is a function of both magma chemistry and temperature, and at similar temperatures is higher in I-type compositions than S-type granites (Clemens et al., 2011) This is evident in the above maficity plots (Figure 1, pg. 6 -7), as the highest Zr values in the granitic suites exist in the Martins Pereira I-type granites, at around 400 ppm. It should also be noted that a steeper gradient between Zr and maficity indicates the entrainment of accessory zircon within the granitic magma is more efficient when compared to rock suites with lower gradients (Clemens et al., 2011).

Examination of the 'Chondrite Normalized REE plot (Figure 2, pg. 8) shows that I-type granites are typically more enriched in the LREE than their S-type granite counterparts. Consequently, the S-type granites appear to display an overall flatter profile. In Figure 2 there is also clear evidence for an overlap between the two granites' anomalies, particularly in relation to Eu. Examination of Figure 2 indicates that the Eu anomalies vary significantly, particularly between the various I-type granitic rock suites. The largest Eu anomaly is present within the I-type granitic rocks of the Iberian Massif (Spain). This large Eu anomaly can be attributed to a variety of factors, such as; a higher proportion of Eu being preferentially integrated into residual plagioclase from partial melting of the protolith (Villaros et al., 2009a); the fractional crystallization of plagioclase within the magma; or a source characterised by a strong, negative Eu anomaly (Rudnick, 1992).



By looking at the 'Trace Element Spidergram' (Figure 3, pg. 9) in the section above it is clear to see that both the I- and S- type granite batholiths have similar trace element patterns. The I- and S-type granites show marked depletion in Nb, Pb, Sr and Eu relative to CI Chondrite. Both granites also show depletion in Nb, Hf, Zr, Y and Yb over Ce and Sm when compared to CI chondrite, which is to be expected in the case of both volcanic arc and collision related granites (Pearce et al., 1984). These characteristics may live on through episodes of crystal recycling. There are slight variations between the profiles of I- and S-type granite suites (Pearce et al., 1984), which can be observed in Figure 3. The S-type granites in the spidergram show lower contents of Zr, Hf, Sm and Ce than the I-type granite profile.

## 2.2 Geodynamic Environments

The idea that different geodynamic settings can be linked with the formation of specific granite geochemistry (e.g., Barbarin, 1999; Pearce et al., 1984) is not a new concept. However, it is one of the more controversial methods to discriminate between granitoid types within the literature. The controversy arises with the misapplication of 'tectonic discrimination' diagrams (see Pearce, 1984) to infer the environmental conditions of magmatism and emplacement (Clemens, 2012; Nédélec et al., 2015). Instead, geodynamic setting can be used to infer the formational conditions of the relevant protolithic material (Clemens, 2012; Roberts and Clemens, 1993).

Barbarin, (1999) suggests that when coupled with relevant and accurate petrological, structural and geodynamic data granitoids can be used as reliable geodynamic indicators. When it comes to his Amphibole-bearing Calc-alkaline Granitoids (ACG) classification group, of which I-type granites are a subset, Barbarin defines the general geodynamic environment to be a subduction zone. Here massive, shallow-lying intrusive bodies containing I-type granites stretch parallel to the trench, and are often overlain by andesitic volcanoes (Barbarin, 1999). Unlike the ACG grouping, the Cordierite-bearing Peraluminous Granitoids group (CPG) to which S-type granites belong, are typically associated with crustal thickening in areas of continental collision (Barbarin, 1999). This process is a consequence of the oceanic lithosphere being completely consumed by subduction processes; resulting in a transitional environment and ultimately continental-continental collision (Barbarin, 1999). This implies that ACGs are generally older features than CPGs.

An example of ACGs and CPGs can be found in the European Variscan fold belt, where a late Palaeozoic Cordilleran-type bilateral subduction event is thought to have taken place (Finger and Steyrer, 1990; Franke, 1989). It is here that calc-alkaline plutonism, specifically in the form of I-type granites, tonalities and granodiorites appear similar to those of the American Cordilleras. Structurally, these I-type granitoids form a belt-like formation running from the

western to eastern Alps (~1000km length), which lies parallel to both the Variscan and Alpine fronts. The few S-type granites of the region are located in the northern most areas and are believed to be Carboniferous in age. The earlier (late Devonian) I-type granites are most prevalent in the southern zone (Finger and Steyrer, 1990). The age, geochemical and structural relationship between both granite types in this case fits well within Barbarin's ACG and CPG constructs. However, the same cannot be said of the I- and S-type granites located in eastern Australia, as well as those of the Cape Granite Suite in South Africa.

The Cape Granite Suite can be separated into three main phases of intrusive events. The first phase is characterized by S-type granites, which intruded into the Tygerberg terrane (600-540 Ma) during, as well as after, collisional related tectonics. These S-type granites are the most voluminous granitic rock type in the Cape Granite Suite. This phase was followed by a post-tectonic intrusion of I-type granites at 560 to 520Ma in the Swartland and Boland terranes to the north-east of the Tygerberg terrane. At ~517Ma the alkali feldspar granites intruded into the monzogranites and granite plutons before a later intrusion of A-type granites at ~520Ma (Scheepers, 1995). These events were later followed by S-type volcanic magmatism (~515Ma) in the form of ignimbrite flows and quartz porphyry intrusions that generated the Postberg ignimbrite and Saldanha quartz porphyry respectively (Scheepers and Poujal, 2002). What is important to note from this example is that the environment was a purely collisional one, in which the S-type granites preceded the younger I-type granite intrusions. This directly contradicts the ideas put forward by Barbarin in his 1999 paper.

An earlier paper by Roberts and Clemens (1993) discredits the theory that I-type calc-alkaline magmas must form as a result of; subduction related process; as a product of volcanic sediments undergoing decompression melting in the post-collisional tectonic stages; or as a consequence of magma mixing with a more mafic magma. Instead Roberts and Clemens (1993) put forward their own model, which revolves around the fluid-absent partial melting of metaluminous rocks located within the lower crust. According to Roberts and Clemens, (1993, pg. 827) in order to satisfactorily recreate the high  $K_2O$  contents and the commonly high  $Na_2O/K_2O$  ratio seen in I-type calc-alkaline rocks, the most appropriate source material would be "hydrated, calc-alkaline, and high-K calc-alkaline andesites and basaltic andesites." The proposed partial melting process is triggered by the underplating/intraplating of the lower crustal rocks by a hot, mafic magma. As the conditions for partial melting are fluid-absent, any water that is present in the newly formed, water-undersaturated felsic magma is considered to exclusively be a product of the breakdown of hydrous minerals, such as micas and amphiboles. The authors draw the conclusion that it is the chemical characteristic of the source material that influences the chemical nature of the magma, rather than the processes or geodynamic environment involved in their generation (Roberts and Clemens, 1993).

## Chapter 3: Explaining Granite Geochemistry

As mysterious and controversial as granites are to geologists, the debate does not simply end there. Historically the geological community has been, and continues to be, largely divided about the processes that are responsible for shaping the geochemistry of granitic magmas.

The paper '*What controls chemical variation in granitic magmas?*' by Clemens and Stevens (2012) summarizes the various models have been developed to explain the observed heterogeneity within exposed granites. There are a variety of parameters that can control the chemistry of granite magmas, including: assimilation, magma mixing and mingling, chemical heterogeneity of the source rocks, progressive partial melting of the source to produce compositionally distinct magma batches, crystal fractionation and phenocryst unmixing, restite entrainment, restite unmixing and peritectic assemblage entrainment. This section serves to highlight some key aspects of the most widely used models of granite formation found within recent literature.

### 3.1 Compositional Variation of Granitic Melts

#### 3.1.1 Chemical Heterogeneity in the Source

The geochemical heterogeneity of granites is considered to be primarily controlled by the source and source related processes (Clemens et al., 2011; Clemens et al., 2009b). Compositional variation within the source rocks is a key contributor in producing the major element and isotopic heterogeneities within granitic rocks (e.g., Clemens, 2003; France-Lanord et al., 1988). The amount of chemical heterogeneity within the source material is proposed to correlate directly with the amount of variation observed within the granites (Chappell and White, 2001). For example, the more variable nature in S-type granite character (particularly in terms of  $Sr^{87}/Sr^{86}$  initial values) over I-type granites, is suggested to result from more chemically heterogeneous source rocks than those responsible for the formation of I-type granites (Chappell and White, 2001).

#### 3.1.2 Pulsed Melt Extractions from a Progressively Melted Source

Anatectic melts derived from the incongruent, partial melting reactions of hydrous minerals within a single source material can be produced in batches. Each melt batch forms as a consequence of the increasing temperatures associated with partial melting (Clemens and Stevens, 2012). Melt batch extraction from the source may alter the bulk composition of the source (e.g., Brown, 2004). This change in source composition, along with increased temperatures and changes in volatile component behaviours, alters the composition of successive melt batches (Clemens and Stevens, 2012; Clemens and Wall, 1981; Yakymchuk

et al., 2011). The composition of the melts becomes increasingly mafic and calcic in composition at higher temperature conditions of melting (Clemens and Stevens, 2012).

As some source material is heterogeneous in composition, i.e. chemically layered, the successive magma batches formed through the partial melting of these rocks will be similarly heterogeneous in character (Clemens et al., 2009b). This can largely be attributed to the fact that the compositional variation within the source material varies on a small-scale. Sequential melting of the source means that reactant minerals involved in the initial partial melting reactions may be entirely different phases, or be compositionally distinct to those involved in subsequent partial melting reactions (Clemens and Stevens, 2012). As melt can be produced in batches, it may also be emplaced in successive batches to create a pluton (Sawyer, 1994), such as the Manaslu leucogranitic pluton (Deniel et al., 1987). During ascent, as well as emplacement, these melt batches can remain both geochemically and spatially isolated, with only incomplete levels of mingling occurring between different melt batches (e.g., Deniel et al., 1987; Pressley and Brown, 1999; Searle et al., 2009). The aforementioned may be attributed to the differing thermophysical and transport properties of the successive melt batches. It is this incomplete mixing of melt batches that can result in major element and isotopic heterogeneities, particularly within leucogranitic rocks (Searle et al., 2009 and references therein).

Both the chemical heterogeneity in the source, as well as pulsed melt extractions from a progressively melted source can account for the chemical variability of leucocratic granites. This is supported by evidence from quenched experimental melts (e.g., Montel and Vielzeuf, 1997) and natural melt inclusions within peritectic phases in anatectic granulites (Taylor and Stevens, 2010) that indicate that granitic melts are leucocratic in composition. However, these aforementioned processes are unable to satisfactorily explain the formation of granites whose compositions are more mafic in composition than typical granitic melts. The generation of these more mafic granites requires one or more of the processes discussed in the 'Models of Formation' section below.

## **3.2 Models of Formation**

### **3.2.1 Source Inheritance Models**

#### **Restite Entrainment Model**

The term 'restite' according to Chappell and White (1991, pg. 376) refers specifically to "any solid material in a plutonic or volcanic rock that is residual from partial melting of the source." The term 'restite' is a blanket-term that includes any of the following minerals and rocks depending on which piece of literature one reads: major silicate minerals that have remained

unchanged by partial melting processes or that were in excess; accessory minerals such as zircon, apatite, monazite, allanite and xenotime (amongst others); enclaves of mica-rich rocks proposed to represent the source; as well as the peritectic mineral assemblage that results from the melting of hydrous minerals during partial melting (Clemens et al., 2011).

The restite entrainment model works on the premise that the minerals within exposed granites are primary restite from the source, or are pseudomorphs (secondary restite) of the original restitic material (Chappell et al., 1987). It was observed that the MgO + FeO content of exposed granitic rocks is higher than those obtained in experimental melts for crustal temperatures. It was therefore concluded that in order for this geochemical observation to be true, granite magmas must contain a significant proportion of entrained restitic material (Chappell et al., 1987). The restite model was also used to bypass the idea of mineral nucleation being a requirement to produce porphyritic granite plutons, instead the large crystal nature of these granites would be a trait directly inherited from the source (Chappell et al., 1987).

### **Restite-Unmixing Hypothesis**

Upon having studied the Lachlan Fold Belt of south-eastern Australia in 1977, White and Chappell put forward their 'restite-unmixing' hypothesis to explain chemical variation within granites (White and Chappell, 1977). The model states that at source conditions the restitic material (unreactive silicate minerals, accessory minerals and peritectic minerals) is in equilibrium with a low temperature melt (Chappell et al., 1987). Once a critical melt fraction has been met this restitic material is mobilized along with a melt, and ascends through the crust in accordance with a diapiric model of ascent (Chappell et al., 1987; Stephens, 2001; White and Chappell, 1977). The restitic material remains largely unable to separate from the melt portion during its ascent, due to the viscosity and yield strength of the melt (Chappell et al., 1987). The aforementioned would suggest that some restite will be preserved within crystalline granitic rocks. The restite-unmixing hypothesis proposes that the geochemical composition of granites at the surface is determined by the degree to which the restite portion separates from the melt (Chappell et al., 1987).

The 'restite-unmixing' hypothesis, and the premise upon which it rests, has come under intense scrutiny in recent years. Clemens and Stevens (2012) discuss the impracticalities of the model in terms of three major limitations. The first limitation of 'restite-unmixing' is that for it to apply, large proportions of restite would need to be visible within granites at the surface. Whilst some restitic material (zircon and monazites) are present in exposed granitic rocks, the other two components of restite (unreactive silicate minerals and peritectic minerals) are not. In the case of the Lachlan Fold Belt's S-type granites, it is proposed that the 'restitic' enclaves,

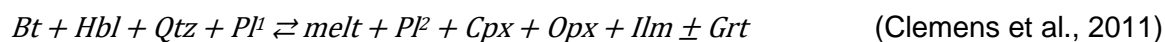
as designated by Chappell and White, are in fact mid-crustal xenolithic material (Clemens, 2003; Vernon 2007). At the conditions of the source, minerals, such as biotite, that are found within granitic enclaves, would be digested during partial melting reactions that are involved in the production of S-type granite magmas. The presence of biotite in the enclaves therefore suggests that the enclaves could not have been produced at the conditions of the source (Clemens, 2003). The second problem with the 'restite-unmixing' model is that it relies heavily on the diapiric ascent model for granite magmas. Diapirism is considered implausible because if the magma (melt + restitic material) from the source ascended as one mobile body (as the mechanism implies), a significant amount of granulite-facies restitic material should be exposed at the surface (Clemens and Mawer, 1992; Clemens and Stevens, 2012). To explain the lack of restite at the surface, Clemens and Mawer (1992) instead suggest a process of granite magma ascent through fracture and conduit networks, where the restitic material would be trapped within the lower levels of the crust (Clemens and Mawer, 1992). The final issue with the 'restite-unmixing' model is that it assumes that the source compositions are directly reflected by the most mafic granites of a suite. For this to be valid there would need to be evidence of large-scale andesitic and pelitic plutons, which from field observations are seen not to exist (Clemens and Stevens, 2012).

In his 2003 paper, Clemens concedes that granites do to a '*certain degree*' mirror their sources, and that it is this mirroring that allows for conclusions to be drawn regarding the distinctly different protoliths and processes involved in formation of both I- and S-type granites. Ultimately, variation in the I- and S- type protoliths allows for the production of significant geochemical variation between the two granite types at the surface.

### **Peritectic Assemblage Entrainment**

The latest to garner recognition in the plethora of granite genesis models is peritectic assemblage entrainment (PAE) (Clemens and Stevens, 2012; Clemens et al., 2011; Stevens et al., 2007). The model proposes that the geochemical heterogeneity of exposed granites, and their corresponding geochemical trends result from the differential entrainment of a distinct mineral assemblage within a hydrous, felsic melt (Clemens et al., 2011; Clemens and Stevens, 2012). This melt + peritectic assemblage is produced via incongruent melting reactions involving the breakdown of hydrous mafic minerals, such as biotite and hornblende, within the source. The peritectic mineral assemblage is dependent on the stoichiometry of the incongruent melting reaction. The stoichiometry of the incongruent melting reaction in turn reflects the composition of source and the pressure-temperature conditions of anatexis (Clemens et al., 2011).

The PAE model was first conceptualised in a study into the S-type granites of the Cape Granite Suite, South Africa (Stevens et al., 2007). The major element geochemical trends (e.g. A/CNK versus maficity; Ti versus maficity) within the granites were determined to be a consequence of the entrainment of peritectic garnet and ilmenite into a leucogranitic melt at the source (Stevens et al., 2007). Further studies (e.g., Clemens and Stevens, 2012), illustrated that the same principles could be applied to various types of granitic rocks, such as I-type granites. These studies concluded that the major and trace element geochemical trends of granites are likely to be the result of the entrainment of a wider array of peritectic minerals than the limited (Grt + Ilm ± Opx) assemblage initially proposed by Stevens et al., (2007) (Clemens, 2012). In the case of I-type granites the protolith is thought to be intermediate in composition (andesite/dacite) (Castro, 2014; Chappell et al., 1998). The hornblende and biotite within the intermediate andesitic/dacitic protolith undergoes an incongruent melting reaction as defined below:



It is the stoichiometry of the above melting reaction that defines the proportion of minerals in the peritectic assemblage, i.e. the molar ratios of Pl : Cpx : Opx : Ilm : Grt. This mineral assemblage is entrained to the ascending melt to form an I-type granitic magma (Clemens and Stevens, 2012). The peritectic minerals are proposed to be highly mobile and easily entrained within the melt due to their small crystal size (Stevens et al., 2007). This small crystal size has been inferred from the fact that the physical processes responsible for the entrainment of accessory minerals, such as zircon and monazite, are similar, if not the same, as those responsible for the entrainment of peritectic minerals (Villaros et al., 2009b). As these accessory minerals are small within metasedimentary rocks, it follows that the entrained peritectic minerals may be similarly sized at the point of entrainment (Villaros et al., 2009b). Studies on natural rock samples from the Mkhondo Valley Metamorphic Suite have indicated the size of entrained garnet crystals to be <1mm in size (Taylor and Stevens, 2010). The size of the entrained crystals were established by examining the size of garnet crystals in “the thinnest, cross cutting leucosome veins” (Taylor and Stevens, 2010, pg. 289).

With entrainment of 35 to 40 mol. % of the peritectic assemblage produced by the melting process producing compositions that are equivalent with the most mafic I-type granite compositions (Clemens and Stevens, 2012). The exact proportion of peritectic minerals to melt is controlled by the physical processes within the source that allow for magma segregation. The most pertinent thing to note about the PAE model though is that it is the stoichiometry and proportion (relative to melt) of the peritectic mineral assemblage entrained

at the source that is the primary control on granite heterogeneity at the surface (Clemens and Stevens, 2012; Clemens et al., 2011).

### ***Geochemical trends***

From a geochemical standpoint, peritectic assemblage entrainment is the only model to date that successfully accounts for the geochemical trends of both compatible and incompatible elements versus maficity that characterise exposed granitic rocks (Clemens and Stevens, 2012). The most significant of these trends is the strong, positive relationship between Ti and maficity and similar Ti:maficite ratios that can be observed in both I- and S-type granitic rocks around the globe (Clemens and Stevens, 2012). In S-type granite magmas this trend is proposed to result from the peritectic mineral assemblage emulating the stoichiometries of the incongruent, partial melting reaction involving biotite within the source (Clemens et al., 2011; Stevens et al., 2007). Conversely, in I-type granites the strong, positive correlation of Ti versus maficity can be ascribed to the entrainment of a distinct peritectic mineral assemblage (Pl + Opx + Cpx + Ilm ± Grt) (Clemens et al., 2011 and references therein). The Ti versus maficity relationship occurs irrespective of the type of source material, and is instead a characteristic produced by the stoichiometries of the peritectic mineral assemblage. This aforementioned fact, along with the extensive overlap in their Ti versus maficity ratios, is why the formation of both I- and S-type granites can be effectively ascribed to the PAE model.

I-type granites display unique geochemical trends, when compared to their S-type counterparts. For example, the melt portion of their magmas is weakly peraluminous, whilst the granites themselves become increasingly metaluminous at moderate to high maficities (Clemens et al., 2011). This trend is proposed to be a direct result of the differential entrainment of a mafic mineral, specifically peritectic clinopyroxene, into a peraluminous melt derived from the source (Clemens et al., 2011). Clinopyroxene is an essential component of the I-type peritectic assemblage, as without it the ASI values seen in I-type granite magmas would be improbable at crustal temperatures (Clemens et al., 2011; Castro et al., 1999). Unlike I-type granite magmas, the ASI value of S-type granites appears to increase within increasing maficity (Clemens et al., 2011). According to Stevens et al., (2007) this trend can be ascribed to the differential entrainment of Grt + Ilm ± Opx into the melt fraction. The positive linear relationship can be observed in the maficity plots in Chapter 2 (Figure 1 (H)), particularly in the S-type granites of the Kosciusko Batholith (Australia) and the Castelo Branco Pluton (Portugal).

Accessory minerals, such as zircon, can be found in both I- and S-type granites. The major difference between the two is that for the same maficity contents of the rocks, I-type granites tend to have higher Zr concentrations (Clemens et al., 2011). The difference in Zr



concentrations between the two granitic rock types relates to the lower modal abundance of inherited zircons in I-type granites, and the highly efficient process of zircon entrainment within I-type granite magmas (Clemens et al., 2011).

Other accessory minerals such as titanite and allanite are proposed to be co-entrained along with the peritectic assemblage in I-type granite magmas. These minerals are liberated from reactant minerals, such as biotite, during incongruent melting. It is noteworthy to mention that peritectic mineral growth most probably occurs in the sites from which these accessory minerals were liberated. The efficient liberation of peritectic minerals from the source is key, as they move both peritectic and accessory phases with them (Villaro et al., 2009a).

In the case of graphed incompatible elements, such as: K, Rb, Sr, Ba and Na, versus maficity their scatter, which is the highest in the most leucocratic rocks, is a function of the inherited variability within the source. This variability within the source is imaged in the plutonic rocks by virtue of the fact that successive magma batches mingle rather than mix (e.g., Pressley and Brown, 1999). The relationship between these incompatible elements and maficity, as can be seen in Figure 1 (C, D, J, K) on pages 6 and 7, is one of decreasing scatter with increasing maficity. This trend occurs due to the fact that these elements are concentrated within the melt, and are thus diluted by peritectic assemblage entrainment (Clemens et al., 2011).

These elements are expressed in the hydrous melt portion of the magma, and provide geologists with clues as to the composition of the reactants in the incongruent melting reaction and the nature of the protolithic material itself (Clemens and Stevens, 2012). Other incompatible elements, such as Li, Be, B and F, express themselves in minerals such as tourmaline and beryl within granitic plutons. The most feasible explanation for their formation is extensive crystal fractionation during emplacement, due to the fact that granitic protoliths have insufficient quantities for their production to be source related (Clemens and Stevens, 2012).

### ***Fate of Entrained Minerals***

According to the PAE model, whilst granite compositions are ultimately a product of their source, the mineral assemblages and compositions observed at the surface are not a simple or direct reflection of the source itself (Clemens et al., 2011; Clemens and Stevens, 2012). Entrained peritectic crystals, although abundant, are small when they are entrained into the melt. During their ascent these crystals are thought to constantly re-equilibrate with the surrounding magmatic conditions (Clemens and Stevens, 2012). This is suggested to occur via a coupled 'dissolution-precipitation' mechanism (Clemens et al., 2011; Clemens and Stevens, 2012; Taylor and Stevens, 2010; Villaro et al., 2009a). Consequently, there is

## CHAPTER 3: EXPLAINING GRANITE GEOCHEMISTRY

relatively little textural and compositional evidence of the higher pressure and temperature peritectic mineral assemblage within exposed granites (Clemens et al., 2011; Clemens and Stevens, 2012). Where evidence of the peritectic minerals exists they show evidence of partial re-equilibration within the surrounding magma (Taylor and Stevens, 2010). Taylor and Stevens' (2010) observations of garnet re-equilibration with the surrounding magma were made in segregated magma volumes trapped in source granulites.

In I-type granitic rocks pyroxene minerals are uncommon features. In cases where they are evident their textural and geochemical nature implies that they have precipitated from the melt. Evidence of high temperature silicates, such as garnets, within I- and S-type granites, indicates that these high temperature silicates were stable within the magma at higher temperatures. As the magma cools upon emplacement, these high temperature phases are seen to be replaced by hydrous minerals. For example, biotite + quartz intergrowths, interpreted to be the products of reaction between melt and orthopyroxene in granitic magmas, are common (Clemens et al., 2011; Clemens and Stevens, 2012; Clemens and Wall., 1988; Maas et al., 1997; White et al., 1999). In S-type granites various degrees of equilibration are observed, namely; cordierite and garnet rimmed by biotite, cordierite and garnet pseudomorphed by biotite, as well as biotite and cordierite being partially replaced by chlorite and/or muscovite (Maas et al., 1997; Villaros et al., 2009a). Whereas, in S-type volcanic rocks there is evidence of clinoamphiboles, such as cummingtonite, partially replacing orthopyroxene (Clemens and Wall, 1988). In I-type granites evidence of partial re-equilibration appears in the form of zoned plagioclases, along with the pseudomorphic replacement of orthopyroxene by biotite and quartz intergrowths (Clemens et al., 2011; Clemens and Stevens, 2012; Maas et al., 1997; White et al., 1999). There is a distinct lack of peritectic feldspars in exposed granitic rocks. The peritectic feldspars are thought to be dissolved into the melt portion and later precipitated as magmatic feldspars with a new, equilibrated composition. Evidence of this includes their "euhedral shape, melt inclusions and oscillatory zoning" (Clemens et al., 2011, pg. 179). In comparison, the ferromagnesian minerals such as garnet will react with the surrounding melt portion to form hydrous minerals, such as hornblende and biotite. These hydrous minerals form as a consequence of the  $a_{H_2O}$  increasing with the pressure decrease associated with magma ascent and corresponding superheating (Clemens et al., 2011; Clemens and Stevens, 2012).

Evidence of a dissolution-precipitation mechanism can be observed in the S-type granites of the Cape Granite Suite (CGS), South Africa. By investigating the evolution of the S-type granites in the region, Villaros et al. (2009) observed that the garnets are homogeneous regardless of their host granite's composition. The geochemical and textural characteristics of the peritectic garnet (high-pressure) entrained at the source are not seen in those exposed

within the CGS (low-pressure). Villaros et al. (2009) reject the idea that these garnets have undergone geochemical changes via a diffusion mechanism, due to the short time scales at which the magmatic events in the region occurred. Calculations conducted by the authors using Carlson (2006) data shows that the self-diffusion process for an entrained garnet grain with a radius of 1cm at the conditions of S-type magma formation within the CGS (i.e. 850° C and 10kb) would take approximately  $3.95 \times 10^8$  yrs. This figure is significantly longer than the proposed dissolution mechanism, which is extremely efficient in comparison at around  $10^2$  to  $10^3$  yrs. The authors have therefore ascribed the garnet homogenisation with the magma to a coupled dissolution-precipitation process.

### 3.2.2 Magma-Mixing

Magma mixing between a basaltic and felsic magma is considered by some to be a viable process (e.g. Zorpi et al., 1989; Chappell, 1996; Vernon, 2007; Karsli et al., 2010) in the generation of calc-alkaline, I-type granites. Hybridization of mantle-derived and crustal derived melt in deep crustal hot zones, or M.A.S.H zones has been inferred to control the isotopic and major element chemistry of granitic rocks (Annen et al., 2006). Underplating of basaltic magmas within the lower crust is suggested to provide sufficient heat and volatile components to induce melting of the pre-existing crustal rocks (Annen et al., 2006). The basaltic magmas are intruded into the lower crust above the magma's liquidus temperature (Annen et al., 2006). As heat is lost from the basaltic magma to the surrounding country rocks, the basaltic magma partially crystallizes (Annen et al., 2006). Conversely, heat transferred to the surrounding crustal rocks raises the temperatures to hypersolidus levels, and these rocks begin to melt (Annen et al., 2006). In the case of simple magma mixing between two endmember magmas thermal equilibrium similarly induces dissolution of crystal components of the felsic magma (Metcalf et al., 1995). The composition and fraction of the residual melts produced by basalt crystallization are controlled by temperatures increases associated with continual basaltic magma injection into the lower crust. Initial melts produced by this process will be rhyolitic in composition, becoming increasingly dacitic and andesitic in composition with increasing temperatures (Annen et al., 2006). It is the continually changing compositional and thermophysical characteristics of these melts that is responsible for the geochemistry of granites. The successive production of varying melt compositions would suggest that crystals formed at initial lower temperatures would be out of compositional equilibrium with the later higher temperature melts, as well as with the more silicic melt compositions derived from melting of lower crustal rocks. These disequilibrium features are preserved in eruptive felsic rocks, such as andesitic lavas, in the form of zoned minerals, variable melt compositions, as well as geochemically distinct populations of individual mineral phases that are not in equilibrium with one another (Kent, 2013). Conversely, petrological examination of granitic

## CHAPTER 3: EXPLAINING GRANITE GEOCHEMISTRY

rocks indicates that they appear not to display mineral compositional or mineral textural evidence of high temperature mineral phases that would be associated with magma mixing/hybridization at lower crustal depths.

The cyclical and episodic nature of magmatism within continental arcs has also been proposed to account for the isotopic and trace element variation between individual plutons/volcanoes, as well as across entire arcs (Paterson and Ducea, 2015). In each cycle there are episodes of increased magmatism within a continental arc known as a 'flare-up', followed by periods of waning magma volumes, known as 'lulls' (Paterson and Ducea, 2015). Any change in the structure, tectonics or chemical composition of the lower crust is thought to trigger periods of increased/decreased magmatism within a continental arc (Paterson and Ducea, 2015). Each magma batch produced by the episodic melting of the lower crust is unique in both its age and in its geochemistry. The geochemical variation between magma batches produced in each cycle may be a result of different magma sources, along with differing depths of the magma batch's formation (Kay et al., 2005). The unique pressure and temperature conditions of each magma batches formation are preserved within the isotopic and "pressure-sensitive trace elements", such as Sr, Y and Nb, within plutonic and volcanic rocks (Kay et al., 2005, pg. 67). Beyond the fluctuations in magma volume, the rate at which magma is added to a continental arc is also an important factor in understanding magmatic systems. In the case of individual plutons determination of the magma addition rate (MAR) has indicated that juvenile magmas are able to recycle older plutonic materials as they ascend through the crust, and are added to the magma chamber (Paterson and Ducea, 2015 and references therein). It is this recycling that is responsible for mixing of melt and crystals that can be observed in both plutonic and volcanic rocks (Paterson and Ducea, 2015 and references therein).

According to a review by Vernon in 2007, there is a distinct lack of restitic components within the S-type granites of the Lachlan Fold Belt, which coincides with similar findings of Clemens (2003). However, unlike Clemens, Vernon offers the suggestion that the some of the enclaves observed within the region are pockets of quenched magma. These pockets result from a peraluminous magma mixing with a more mafic magma at near source levels. The author likens these processes observed in the S-type granites, to similar processes which generate microgranitoid enclaves globally within I-type magmas (Vernon, 2007).

Others ascribe the enclave formation within granites to be a result of the incorporation of accessory magmas into the host magma. These accessory magmas might have little to no influence on the composition of the host magma (Clemens, 2003; Clemens et al., 2011; Clemens et al., 2009a). Magma mixing between crustally-derived melt and more mafic mantle-derived melt is unlikely. This is evident when looking at the correlation between Ti and maficity,

as well as K and maficity in granitic magmas. Ti has a low solubility within the melt, and is found to be concentrated within the peritectic assemblage. Conversely, K has a high solubility within the melt, which accounts for the high-K component seen within the melt portion of the system (Clemens et al., 2011). Both Ti and K exhibit strong positive and negative correlations respectively. Mantle-derived melts have Ti concentrations that vary significantly, but not significantly higher than in many granites. This Ti variation implies that magma mixing processes between mantle and leucogranitic melts would result in distinctly different granite compositions, each with its own unique Ti:maficity ratios. Both experimental and field related data has shown that all granites display similar Ti versus maficity trends, regardless of their composition, making it unlikely that I-type granites could have developed through magma mixing processes (Clemens et al., 2011). Isotopic data collated from I-type granites shows that a mafic magma component is unlikely to have played a significant role in their formation, except potentially in the case of a “hyper-enriched, metasomatised mantle” (Clemens et al., 2011, pg. 176). Magma mixing has been argued as impractical to account for the formation of I-type granites, particularly from a geochemical perspective. As although both the A/CNK and K/Na ratios of I-type granites align with a magma mixing model, the Ti versus maficity ratio is incompatible (Castro, 2014). A magma mixing mechanism would also result in both the major and isotopic geochemical concentrations of the basaltic and felsic end-member magmas changing in a similar manner (Castro, 2014). This is not the case in real-world scenarios where extensive “decoupling between major elements contents and radiogenic isotopes” is prevalent (Castro, 2014, pg. 66).

The aforementioned examples provide a glimpse into the extensive debate surrounding the feasibility of the magma mixing models to account for granite production within the literature. However, it is not the aim of this research to argue against the feasibility of this process. Instead this research can provide valuable insight into the types of kinetic processes that are responsible for the removal or equilibration of high temperature and pressure phases within granites that are proposed to be derived from magma mixing process (e.g., Vernon, 2007).

### **3.2.3 Assimilation**

The assimilation model is one in which the incorporation of crustal material (wall-rock or xenolithic material) is responsible for generating the geochemical and isotopic characteristics of granitic rocks (Clemens and Stevens, 2012). This variation is suggested to result from the fact that assimilated material may be entirely geochemically distinct, as well as significantly older than the magma into which it is assimilating (Annen et al., 2006). In order to melt and assimilate wall rock, a significant amount of heat needs to be conducted from the ascending, mantle-derived mafic magma to the surrounding wall rock. These heat losses from the magma induce crystallization (Nédélec et al., 2015). Experiments on the assimilation of gneissic

material into basaltic liquids conducted by Patiño-Douce (1995) produced magmas that constituted granitic melt and crystals (Opx, Cpx, Pl  $\pm$  Grt) (Nédélec et al., 2015). In general, any mica or amphibole bearing crustal component that is assimilated into a magma at temperature ranges of 850 - 900°C will undergo dehydration reactions to produce Opx + Cpx + Ca-rich Pl + Oxides  $\pm$  Grt, and a hydrous melt (Beard et al., 2005). This mineral assemblage correlates to the 'peritectic' mineral assemblage utilized within this research. Consequently, direct parallels can be drawn between the compositional and textural 'fates' of minerals generated through dehydration reactions associated with peritectic mineral entrainment, and those resulting from assimilation processes.

Similarly to magma mixing/hybridization processes there are arguments against assimilation processes being primary contributors to granite geochemical heterogeneity. The assimilation model is seen by many to be unviable for a variety of reasons. Firstly, although the isotopic data can reproduce trends observed in granitic rocks it is unable to do so satisfactorily for the major elements (Clemens, 2012). Secondly, the energy required to melt the assimilated material would exceed the available energy of the system. If sufficient energy were available, the magma would become so crystal saturated that it would become stagnant (Glazner, 2007). Finally, the distinct lack of restitic enclaves within the vast majority of exposed granites would strongly suggest there is no material being assimilated, as one would expect small remnants of the wall-rock material to be preserved (Clemens and Stevens, 2012). Clemens and Stevens (2012) suggest that wall-rock assimilation is a viable process on a small, localized scale, and cannot be a primary factor contributing to the heterogeneity of an entire granitic pluton.

#### **3.2.4 Fractional Crystallization**

Crystal fractionation is another widely accepted model relating to granite genesis. Fundamentally it involves the partial or complete removal, or isolation, of crystals from a magma. As these minerals are removed or isolated from the rest of the melt portion they are unable to re-equilibrate with the progressively changing pressure and temperature conditions of the surrounding granite magma (Clemens and Stevens, 2012). Fractional crystallization of mafic magmas can produce residual liquids that are largely granitic in their composition. The amount of residual granitic liquid produced via this process is insufficient to account for the widespread, global abundance of granites, and on the whole this process is proposed to account for <10% of granite production worldwide (Best, 1982).

Rejection of crystal fractionation as a viable primary genetic model for granites rests on two key factors. The first being the fact that pulses of magma are responsible for pluton development, rather than the intrusion of one single, pluton sized magma batch (e.g., Glazner et al., 2004; Petford et al., 2000). Between each magma pulse sufficient time may lapse to

allow for each magma layer to partially solidify (Clemens and Stevens, 2012). This implies that if crystal fractionation were to occur it could only take place on a small-scale, and not chamber wide (e.g., Reid et al., 1993). The second criticism of the model is similar to that of the 'restite-unmixing' model. Essentially, the crystal fractionation of biotite or hornblende at depth would be unable to produce the strong, positive Ti vs maficity trends observed within all granitic rocks. However, the crystal fractionation process would produce similarly tight K vs maficity trends that are not observed within granitic suites (Clemens and Stevens, 2012).

### 3.3 Concluding Remarks

Irrespective of the processes by which granite magmas attain their compositions, it appears clear that typical granite magmas exist as mixtures of melt and crystals prior to their intrusion into the sites of pluton assembly. There is little to no evidence of the entrained residuum within exposed granitoid rocks (Clemens et al., 2011; Clemens and Stevens, 2012; Clemens and Wall, 1988; Vernon et al., 2009). According to the literature this is a consequence of a rapid and efficient process of 'dissolution-precipitation', which re-equilibrates minerals with the surrounding magmatic conditions during both ascent and emplacement (e.g., Villaros et al., 2009a). This study has chosen to investigate the fate of a peritectic mineral assemblage (Pl + Opx + Cpx + Ilm ± Grt) that, according to the Clemens et al., (2011), might be involved in the formation of a mafic I-type granodiorite. The peritectic assemblage entrainment (PAE) model has been used over other potential petrogenetic processes as it defines the entrained residuum with clarity. Thus, the experimental design that follows matches the concept of peritectic assemblage entrainment in detail. In addition, when all the aforementioned evidence relating to granitic magma petrogenesis is considered, the PAE model appears to be the most suitable petrogenetic process to produce I-type granites and their unique geochemical characteristics.

## Chapter 4: Experimental Design

This chapter outlines in detail the analytical techniques and experimental procedures used throughout this research. 'Analytical Techniques' gives the reader a comprehensive breakdown of the equipment and standards employed during analysis of both the starting materials and final run products. The 'Phase Equilibrium Modelling' subsection of this chapter allows the reader insight into the foundation and thought-process involved in undertaking this research. 'Experimental Methodology' contains a step-by-step breakdown of various experimental techniques ranging from the production of a synthetic starting material to the creation of gold capsules. This section also discusses the technical ins-and-outs of the experimental apparatus used in this research. The reader will note that, where relevant, justification of the methods and equipment used within this research has been provided.

To develop the narrative of I-type granite genesis we need to look at its three major landscapes. The first landscape is one of tangibility. In this landscape, real-world observations of exposed I-type granites allow for deductive reasoning. Whilst this approach is highly valuable, its reliance on 'top-down' logic is particularly problematic where I-type granites are concerned. Certain granitic plutons lack physical evidence of source related material, which means the use of top-down logic to draw conclusions about the genetic history of these rocks is subject to strong limitations. The second landscape is one in which experimental techniques are utilized to provide windows into various stages of formation from the source to emplacement. These techniques allow for the use of inductive reasoning. The issue with employing experimental techniques is that they limit the ability to study pertinent magmatic processes, such as fractional melting and magma segregation. These limitations result because the experiments are closed systems, which can only be altered by controlled changes in the temperature and pressure conditions to which they are subjected. The third landscape is a thermodynamic approach, which involves phase equilibrium modelling of various compositions over a range of pertinent pressure-temperature conditions. This approach is borrowed from metamorphic studies of partially melted rocks. To date this technique has not been used widely within igneous studies, although it has the potential to significantly advance understanding of igneous processes within felsic magmas. This study has chosen to focus on the latter two landscapes.



## 4.1 Analytical Techniques

A variety of analytical techniques have been employed during this research. These various analytical methods are outlined in the subsections that follow.

### ***X-ray Fluorescence***

PANalytical X-Ray Fluorescence analysis was conducted on the major element chemistry of the synthetic starting gel. This analysis was conducted both before and after the addition of synthesized fayalite, kaolinite and  $\text{TiO}_2$  to the gel. The XRF contains a 3kWatt Rh X-ray tube fitting and both NIST® and SARM® standards were used during the element analysis.

### ***X-ray Diffraction***

The composition of the fayalite utilized in the experiments was determined using a Bruker D8 X-ray Powder Diffractometer (XRD) with a Cu sealed tube. The XRD results for fayalite were then compared to XRD patterns within the literature. From these comparisons it was determined that the synthesized fayalite was suitable to use in the experiments.

### ***Sample Preparation***

The starting bulk composition, as well as the experimental run product samples were prepared according to the following steps. The relevant material to be analysed was placed on a rough thin-section slide and covered with liquid epoxy. In the case of the experimental run products the gold capsule was broken open using scissors and the run product was removed using tweezers. The thin section slide was then left to dry and harden overnight. The thin-section slide was then placed into a thin-section weight. The epoxy was then ground down under water using a Jean Wirtz TG200 grinder with a  $15\mu\text{m}$  grinding pad until the experimental material within the epoxy was exposed and flat. The thin-section slide was then polished using a Struers Rotopol-35 on  $9\mu\text{m}$ ,  $3\mu\text{m}$  and  $1\mu\text{m}$  polishing pads with the relevant polishing fluid.

### ***Scanning Electron Microscopy***

Thin-section slides containing the relevant peritectic assemblage/experimental run products were analysed using the Zeiss® EVO MA 15 Scanning Electron Microscope (SEM) fitted with an Oxford Instrument® Energy Dispersive X-Ray Spectrometer attachment. Standard settings outlined in the SEM manual provided to users were utilized during each analysis. These settings include; carbon coating of samples to  $15\mu\text{m}$ , a working distance of 8.5mm, a Faraday Cup reading of between -19nA and -20nA, beam current of 100 $\mu\text{m}$  and an accelerating voltage of 20kV. The SEM runs using INCA software; and the Energy-dispersive X-ray spectrometry option was utilized to analyse the major element chemistry of the samples. The results of the analyses are detailed in the tables (Table 7, pg. 48). The natural standards used for each

mineral can be found within the Appendix under Zeiss® EVO MA 15 Scanning Electron Microscope Mineral Standards.

High resolution backscattered electron images of the starting bulk composition were also taken using the SEM, which required the standard settings of the machine to be adjusted such that the working distance was reduced to between 6.0 and 7.5mm.

Analysis of melt within the run products required the sample to be cooled down to  $-180^{\circ}\text{C}$  on a Gatan cryogenic stage using liquid nitrogen. Liquid nitrogen was added intermittently in order to ensure the stage temperature was regulated. Unlike standard SEM analysis a Faraday cup cannot be utilized during melt analysis, which means that the beam current cannot be checked. To curb this issue and to ensure beam stability, volatile free phases, such as quartz and plagioclase, were analysed intermittently to ensure the accuracy of the melt results. Using a cryogenic stage also reduced count losses of alkalis, in particular sodium and potassium, that can arise through quantitative electron microprobe analysis (e.g., Moyen and Stevens, 2006; Nielsen and Sigurdsson, 1981).

### ***Phase Equilibrium Modelling***

Equilibrium assemblages were modelled using THERIAK-DOMINO Software (de Capitani and Petrakakis, 2010). Pseudosections 1 and 2 were calculated using THERIAK-DOMINO software developed by de Capitani and Petrakakis in 2010. The database used was compiled by Douglas Tinkham, and is based upon the original database developed by Holland and Powell in 1998. The following solution models from the database were utilized; PLC1 (Holland and Powell, 2003), GT07W2 (White et al., 2007), BI05 (White et al., 2005), ILM05 (White et al., 2000), OPX (White et al., 2002), CAMP11 (Diener and Powell, 2012), CPX11 (Diener and Powell, 2012), LIQtC2 (White et al., 2007). These models allow for a range of phases including; plagioclase, garnet, biotite, ilmenite, orthopyroxene, clinopyroxene, quartz, rutile, sphene and melt to be plotted. The reader should note that the plagioclase model of Holland and Powell (2003) encompasses the three feldspar endmembers;  $\text{KAlSi}_3\text{O}_8$  -  $\text{NaAlSi}_3\text{O}_8$  -  $\text{CaAlSi}_3\text{O}_8$ . The phase equilibrium models were edited and labelled in Adobe Illustrator® CS4. The results of the modelling can be found in the section that follows below.

## ***4.2 Phase Equilibrium Modelling – A Rationale of Experimental Techniques***

Pseudosection models are invaluable tools that aid in the understanding of how phase assemblages and compositions alter over a range of pressure and temperature conditions within a defined composition. They allow for a variety of important data such as; equilibrium assemblages, mineral modes, isopleths of phase compositional parameters, and the location of the solidus, to be calculated and graphically represented. The combination of this collective

## CHAPTER 4: EXPERIMENTAL DESIGN

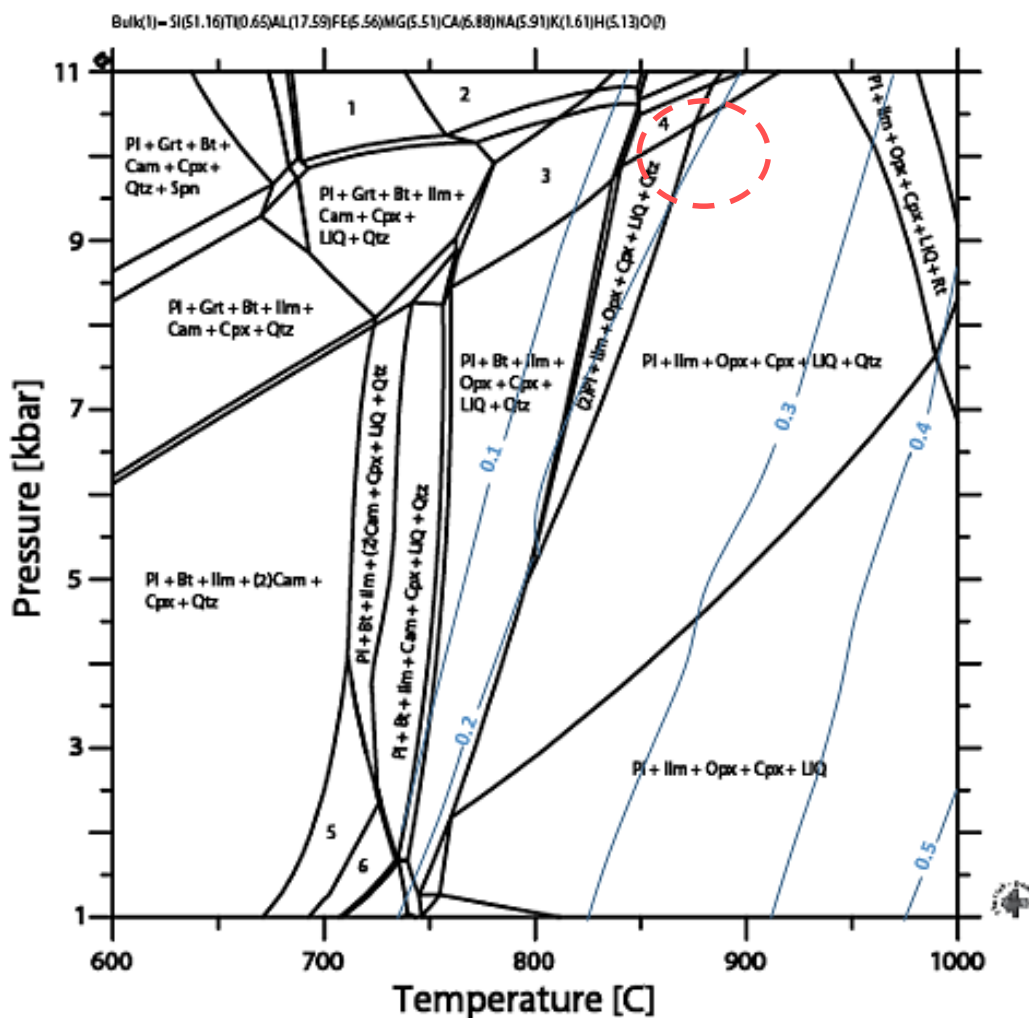
data provides the foundation on which to establish appropriate pressure and temperature conditions for experimentation. Reviews on the agreement between previous experimental studies on granulite facies rocks (e.g. Tropper et al., 2005) and Theriak-Domino modelling outputs have shown the two methods to be in good agreement with one another (e.g., Tropper et al., 2015). Although discrepancies, such as the biotite stability and melt proportion, are commonly evident between the different methods (Tropper et al., 2015).


Despite the multitude of benefits pseudosections can provide, they are not without their limitations. Discrepancies can, and do, exist between what mineral assemblages and compositions a phase equilibrium model predicts versus what is observed in the field or through experimentation. There are several issues surrounding phase equilibrium modelling. One of the most prominent is the gap in current knowledge surrounding certain thermodynamic properties of minerals and melts (White et al., 2011). This means that the input data, such as the thermodynamic datasets and mineral and melt activity models within the system, particularly in relation to the activity-compositional relationships, are not well defined (White et al., 2011). The quality of the user defined data can also be responsible for generating inexplicable or inaccurate modelling outputs. In some cases the solution models within the software may be unsuitable for the specific bulk composition to be modelled (e.g. ultramafic rocks) or they may contain general inaccuracies (de Capitani and Petrakakis, 2010; White et al., 2011). For example, the latest amphibole and clinopyroxene models (Diener and Powell, 2012) have been utilized to develop the phase equilibrium models (Figure 4, pg. 34; Figure 5, pg. 35) that follow below. In spite of the significant improvements made over the previous versions, the model still contains some prominent issues. The issue most relevant to this research is the fact that the models have been calibrated specifically for greenschist, blueschist, amphibolite and eclogite facies metamorphic conditions (Diener and Powell, 2012) whilst this research focuses on granulite facies conditions. At granulite facies conditions element substitutions involving K and Ti have not been accounted for by the models (Diener and Powell, 2012). This is a significant issue as it indicates that the pseudosection models are a substantial simplification over natural systems. Thermodynamic modelling software packages, such as Theriak Domino, are also unable to provide information on the rates of reactions and reaction pathways. Instead this information can be ascertained through analysis of experimental run products. It is clear, from all of the aforementioned, that modelling software does not account for all the variables at play within a real-world system, but instead provides the users with relevant approximations (de Capitani and Petrakakis, 2010).

Pseudosection 1 (Figure 4, pg.34) illustrates the influence of pressure and temperature variations on an andesitic source composition (composition taken from Clemens et al., 2011, pg. 180). This andesitic composition is intended to represent a hypothetical I-type granite

source originating within the lower continental crust (Clemens et al., 2011; Barbarin, 1999; Scheepers, 1995; Roberts and Clemens, 1993; Hine et al., 1978). The intention in developing Pseudosection 1 (Figure 4, overleaf) was to quell any doubt regarding the feasibility of clinopyroxene being a source related component. From the phase equilibrium model (Figure 4, overleaf) it can be seen that for the source pressure and temperature conditions (approx. 9kbar and 850°C) clinopyroxene is a stable phase. The stability of clinopyroxene within the source is important, as according to the peritectic assemblage entrainment model, its entrainment is essential in generating the distinct geochemical characteristics of I-type granites. The formation of this mineral assemblage is a consequence of the fluid-absent, incongruent melting of biotite and hornblende within the source material. Other significant peritectic minerals, namely plagioclase and ilmenite, are also evident at the proposed pressure-temperature conditions of the source. Based upon the hypothetical source composition below garnet does not form part of the peritectic assemblage at the relevant pressure and temperature conditions of the source. According to the literature, the inclusion of garnet within the peritectic assemblage is largely controlled by the composition of the source material, specifically its Mg#, as well as the pressure conditions of incongruent melting within the source (Villaros et al., 2009a and references therein). Although supported by the literature, Pseudosection 1 provides the reader with tangible insight into the rationale behind including these phases within the 'peritectic' mineral assemblage utilized within this research.

## CHAPTER 4: EXPERIMENTAL DESIGN

**LEGEND**

 I-type granite source PT region (approximate)

 Melt Isopleths (vol. %)

- 1 PI + Grt + Bt + Cpx + LIQ + Qtz + Rt
- 2 PI + Grt + Bt + Cam + Cpx + LIQ + Qtz + Rt
- 3 PI + Grt + Bt + Ilm + Opx + Cpx + LIQ + Qtz
- 4 (2)PI + Grt + Ilm + Opx + Cpx + LIQ + Qtz
- 5 PI + Bt + Ilm + (2)Cam + Cpx + H<sub>2</sub>O + Qtz
- 6 PI + Bt + Ilm + Cam + Cpx + H<sub>2</sub>O + Qtz

Figure 4 - Pseudosection 1

Phase equilibrium model of an andesite (taken from Clemens et al., 2011, pg. 180) intended to represent the source composition of I-type granites (as proposed in Clemens et al., 2011; Barbarin, 1999; Scheepers, 1995; Roberts and Clemens, 1993; Hine et al., 1978). The mineral-melt assemblage (PI + Ilm + Opx + Cpx + LIQ + Qtz) at the proposed pressure-temperature conditions of the source (dashed circle) are predicted to result from the fluid-absent, incongruent melting of both biotite and hornblende within the source material (e.g., Clemens et al., 2011).

This research is predominantly focused on the 'fate' of entrained peritectic minerals in high-level granites at various stages of isobaric cooling. As a result, granulite facies conditions (1 - 11kbar; 600 - 1000°C) were deemed apt to develop a phase equilibrium model that reflects the entire granitic system from the proposed pressure and temperature conditions of the source to those corresponding to its final emplacement. Pseudosection 2 illustrates the various mineral assemblages obtained when the starting bulk composition is 'exposed' to lower-granulite facies conditions.

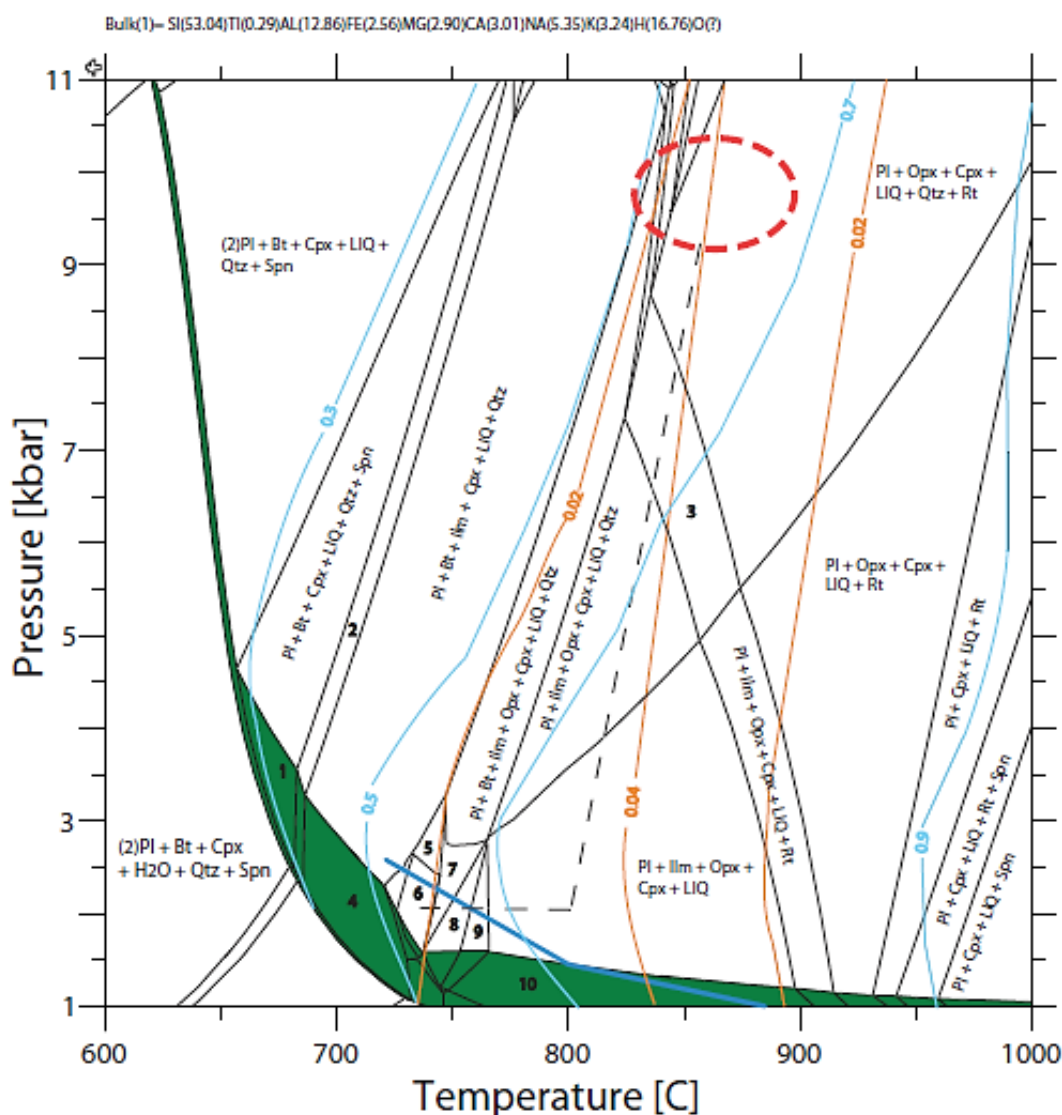








Figure 5 - Pseudosection 2

Phase equilibrium model displaying the range of mineral assemblages produced when an average I-type granite composition is exposed to granulite facies conditions. This average I-type granite composition is the one utilized within this study as the starting bulk composition.

**LEGEND**

-  Cold-Seal Pressure Vessel Pressure-Temperature Upper Limits
  -  Melt Isopleths (vol. %)
  -  Orthopyroxene Isopleths (vol. %)
  -  Hypothetical Ascent and Cooling Paths
  -  H<sub>2</sub>O – Melt Saturation Band
  -  I-type granite source PT region (approximate)
- 1 PI + Bt + Cpx + LIQ + H<sub>2</sub>O + Qtz + Spn
  - 2 PI + Bt + Cpx + LIQ + Qtz + Spn
  - 3 PI + Ilm + Opx + Cpx + LIQ + Qtz + Rt
  - 4 PI + Bt + Ilm + Cpx + LIQ + H<sub>2</sub>O + Qtz
  - 5 PI + Bt + Ilm + Cam + Cpx + LIQ + Qtz
  - 6 PI + Bt + Ilm + (2)Cam + Cpx + LIQ + Qtz
  - 7 PI + Bt + Ilm + Opx + Cam + Cpx + LIQ + Qtz
  - 8 PI + Bt + Ilm + Opx + Cam + Cpx + LIQ
  - 9 PI + Ilm + Opx + Cam + Cpx + LIQ
  - 10 PI + Ilm + Opx + Cpx + LIQ + H<sub>2</sub>O

***Issues with Clinopyroxene Modelling***

Pseudosection 2 (Figure 5, pg. 35) predicts clinopyroxene to be a stable phase across the subsolidus pressure-temperature range. The unlikely coexistence of PI, Qtz, Cpx and H<sub>2</sub>O in this region, would indicate issues with the modelling technique across these pressures and temperatures. This overestimation of clinopyroxene stability may be ascribed to issues with the amphibole model; i.e. that substitutions involving K and Ti have not been accounted for by the model at granulite facies conditions (Diener and Powell, 2012). In natural granitic rocks it is likely that the Ca component within the entrained clinopyroxene would have facilitated the growth of apatite, which would be impossible to produce from the starting bulk composition used to create the phase equilibrium model above.

At hypersolidus conditions further issues appear to be apparent with the clinopyroxene model, specifically in its ability to constrain the clinopyroxene volume percentages at lower temperatures (<760°C). Examination of the modelling output indicates that the volume percentages of clinopyroxene are seen to fluctuate dramatically (in some cases across a tenth of a degree) at these low temperatures and across the entire pressure range (1 – 11kbar). This is the only mineral out of the modelled mineral assemblage that appears to fluctuate in its predicted volume to this extent. The aforementioned has made constraining the volume

percent isopleths of clinopyroxene high on impossible, both manually and through software outputs. This accounts for the noticeable absence of clinopyroxene volume percent isopleths within Figure 5 (pg. 35).

### ***Hypersolidus Conditions***

It should be noted that across the wide range of pressures (1-11kbar) and temperatures (600-1000°C) of the phase equilibrium model there is no evidence of a liquidus. This corresponds to the literature that proposes I-type granitic magmas of intermediate to mafic compositions consist of both melt and crystals (restitic/peritectic) at even the highest temperatures (1000°C) of crustal anatexis (Clemens et al., 2011; Clemens and Stevens, 2012; Stevens et al., 2007; Villaros et al., 2009; White and Chappell, 1977). At the proposed conditions of partial melting of the source the mineral-melt assemblage of this I-type granite composition is the same as in Pseudosection 1 (pg. 34) for the suggested andesitic source material (barring rutile and ilmenite). This implies that andesite compositions, such as the one in Pseudosection 1 (pg. 34) are suitable source materials to generate I-type granites of intermediate to mafic composition.

### ***Hypothetical Ascent Path***

The ascent path represents the ascent path of the I-type granitic magma from the hypothetical source to higher levels within the continental crust. The dashed line begins at source conditions (~ 9kbar; 850°C), in which melt segregation from the source and the entrainment of peritectic minerals takes place. It is generally suggested that magma ascent is an adiabatic process, i.e. one in which thermal energy is not gained or lost during decompression (Rutherford, 2008). However, heat transfers can result from losses to the surrounding wall rock during ascent, as well as through the formation of vesicles (gas expansion). Although the magma is also able to undergo heating as a consequence of latent heat being released during crystallization (Rutherford, 2008). Unlike the cooling path the ascent path has a steep gradient. The fact that the path is sloped indicates that with the pressure decrease associated with magma ascent there is a corresponding temperature decrease (e.g., Stevens et al., 2007). This drop in temperature is minimal (approx. 50°C) as the rate of ascent is thought to be rapid (Stevens et al., 2007). This rapid ascent rate means that the granitic magma has minimal time to interact with the surrounding wall rock during ascent, and is geochemically isolated from its surroundings (Clemens, 2003).

### ***Hypothetical Isobaric Cooling Path***

This path forms the basis for this research. A portion of this range was investigated within this research, specifically over a temperature range of 720 - 770°C and at a pressure condition of ~2kbar. The mineral assemblages vary considerably along this cooling path, making this a



compelling area to research. This path describes the mineralogical changes that occur during granite emplacement within higher levels of the crust (~10km depth). The most significant mineralogical changes observed along the path (as indicated by Pseudosection 2, pg. 35) is the formation of biotite and clinoamphibole at lower temperatures. Biotite is the predominant ferromagnesian mineral at these lower temperature conditions.

### ***Experimental Constraints***

Experimental constraints on this research relate largely to the limitations of the machinery used. For example, experiments had to be conducted below the pressure-temperature limits of the cold-seal pressure vessels (blue line on Pseudosection 2, pg.35) in order to prevent damage to the machinery. This, combined with the fact that the experiments needed to be conducted at pressure and temperature conditions above the zone of H<sub>2</sub>O-melt saturation (green-shaded area), has meant that only a small temperature and pressure range could be investigated in this research.

## **4.3 Experimental Methodology**

### ***Synthetic Starting Material***

The main purpose of this study is to shed light on the 'fate' of entrained peritectic minerals within a granitic magma at upper crustal pressure and temperature conditions. To achieve this by experimentation a synthetic starting material was used. This starting material, along with a hypothetical peritectic mineral assemblage, was synthesized to be representative of the melt portion within a natural granitic system. The anhydrous composition of the melt was obtained from Sen and Dunn (1994). Granitic melts generated from the fluid-absent, partial melting of biotite and hornblende in both quartzofeldspathic and intermediate source rocks have H<sub>2</sub>O contents ranging from 3.0 to 4.7 wt. % at 10kbar (Clemens and Vielzeuf, 1987). Consequently, the initial melt composition was recalculated to include 4.49 wt. % water.

A synthetic oxide mixture was prepared according to the method drafted in Hamilton and Henderson, 1968. However, for the purposes of this research various alterations to the method were necessary. Unlike in Hamilton and Henderson's method kaolinite and synthesised fayalite were added to the oxide mixture upon its completion. The fayalite encompassed the total FeO required to produce the melt fraction. The rationale behind adding fayalite was to avoid issues with iron oxidation that can occur when other reagents, such as Fe<sup>3+</sup> powder or Fe metal sponge, are added to an oxide mixture. The addition of kaolinite meant human errors associated with manually adding liquid H<sub>2</sub>O into the experimental capsules using a syringe could be avoided entirely. The kaolinite provided the total H<sub>2</sub>O and Al<sub>2</sub>O<sub>3</sub> components within the starting material. As it is hygroscopic in nature, care was taken to ensure that the kaolinite

was stored within a drying cupboard at 110°C prior to its inclusion in the starting material. The proportions of fayalite and kaolinite added to the starting material were determined through stoichiometric calculations.

The fayalite used within the experiments was synthesised by combining SiO<sub>2</sub>, Fe metal and Fe<sub>2</sub>O<sub>3</sub> in the correct molar proportions. This mixture was then pressed into pellets (~0.5cm diameter) using a hydraulic press. Oxyacetylene welding was conducted on the base of a glass tube. The pellets were then placed into the tube. The tube was flushed with argon gas, and then the tube was melted closed under vacuum. A vacuum test was then conducted on the tube to determine if there were any leakages. This was done by submerging the tube in water within a Schlenk flask under vacuum. Once it was established that the tube was airtight; it was placed in a furnace at ~900°C for 3 days. The resulting fayalite powder was then removed from the tube and analysed using X-Ray Diffraction. The powder was then ground down to a fine powder (<50µm) using an agate pestle and mortar.

Both the fayalite and kaolinite were added in the correct molar proportions to the oxide mixture upon its completion. The mixture comprised of a number of oxides, specifically SiO<sub>2</sub>, TiO<sub>2</sub>, Al<sub>2</sub>O<sub>3</sub>, MgO, CaO, Na<sub>2</sub>O and K<sub>2</sub>O. The exact composition of the oxide mixture is outlined in Table 1 below.

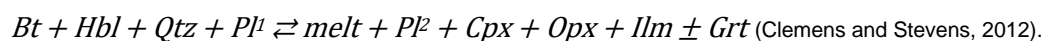
**Table 1 - Synthetic Silicate Melt Composition**

SiO <sub>2</sub>	TiO <sub>2</sub>	Al <sub>2</sub> O <sub>3</sub>	Fe <sub>2</sub> O <sub>3</sub>	FeO	MnO	MgO	CaO	Na <sub>2</sub> O	K <sub>2</sub> O	H <sub>2</sub> O	Sum
72.35	0.11	12.89	0.00	0.97	0.00	0.09	1.00	3.57	4.55	4.49	100.00

The final result produces a white powder. The powder was wet-batch milled for 25 minutes under acetone in a Fritsch Planetary Mill to ensure a fineness of <50µm. Once this process was complete the powder was left to dry at room temperature, before later storage at 110°C in a drying cupboard.

### ***Peritectic Mineral Assemblage***

The melting reaction involved in the production of I-type granitic magmas is as follows:



From this melting reaction it can be determined that the peritectic assemblage comprises of; plagioclase, clinopyroxene, orthopyroxene, ilmenite and garnet.

The aforementioned minerals were collected from Limpopo granulite samples provided by Gautier Nicoli. Each of the rock samples were crushed into grains ranging in size from 2-4mm using a geological hammer. The plagioclase grains were then individually separated using

## CHAPTER 4: EXPERIMENTAL DESIGN

tweezers into the relevant seed crystals under a WILD M400 Photomicroscope (x1.25). The plagioclase grains were then placed in a resealable bag. This process was then repeated for each of the required minerals. These grains formed the peritectic mineral seeds used within each of the experiments.

Individual seeds of each peritectic mineral were mounted to a thin-section slide and analysed according to the method outlined in 'Analytical Techniques' subheading above to determine their compositions (Table 7, pg.48). As granulite facies minerals are fairly homogeneous in nature, the composition of the seeds were assumed to be representative of the sample.

Upon determination of peritectic mineral compositions, calculations were conducted to determine the stoichiometric proportions of the minerals according to the melting reaction suggested by Clemens and Stevens, 2012. The overall proportion of magma to be comprised of peritectic minerals was chosen to be 30 wt. %, which is in line with maximum figures proposed by Petford et al., (2000) for the realistic crystal load of granite magmas. Also this amount of entrained crystals appears to be required to account for common granodioritic compositions (Stevens and Clemens, in press). The calculated proportions of peritectic minerals were then weighed on a suitably sensitive balance scale and combined. The bulk composition of the peritectic mineral assemblage is outlined in Table 2 (below).

**Table 2 - Peritectic Mineral Assemblage Bulk Composition**

SiO <sub>2</sub>	TiO <sub>2</sub>	Al <sub>2</sub> O <sub>3</sub>	FeO	MnO	MgO	CaO	Na <sub>2</sub> O	K <sub>2</sub> O	Sum
52.33	1.36	15.44	10.46	0.00	7.88	9.36	3.16	0.00	100

The peritectic mineral assemblage was then ground down under acetone using an agate pestle and mortar until it formed a fine powder. This peritectic assemblage was then added to the synthetic melt powder, and stored for the duration of the study at 110°C in a drying cupboard. The melt powder and peritectic mineral mixture is hereinafter referred to as the 'Starting Bulk Composition'. The composition of the finished starting material is outlined in Table 3 (below). Textural analysis of the Starting Bulk Composition using a Zeiss® EVO MA 15 Scanning Electron Microscope (method outlined in Analytical Techniques) showed that the average size of the synthetic melt powder to be <50µm (length), whilst the peritectic mineral assemblage was <400µm (length).

**Table 3 - Starting Bulk Composition**

SiO <sub>2</sub>	TiO <sub>2</sub>	Al <sub>2</sub> O <sub>3</sub>	FeO	MnO	MgO	CaO	Na <sub>2</sub> O	K <sub>2</sub> O	H <sub>2</sub> O	Sum
66.34	0.48	13.65	3.82	0.00	2.43	3.51	3.45	3.18	3.14	100

### ***Capsules***

The capsules utilised within the experiments were created by fashioning gold sheets into cylindrical tubes. The gold sheets were approximately 2mm in thickness. Gold was chosen as the capsule medium as it is almost inert, easy to mould into cylinders and it has a low H<sub>2</sub> diffusivity (Ratajeski and Sisson, 1999). However, one of the most important reasons gold was used is that in regards to silicate samples gold absorbs minimal Fe (Ratajeski and Sisson, 1999). The base of the cylindrical tube was crimped using pliers to a depth of 2mm. An arc welder with a graphite electrode (set at 70A) was then used to seal the end. This method created a 'toothpaste-tube' style well in which the materials relevant to experimentation could sit. The sealed end was then examined under a WILD M400 Photomicroscope (x1.25) to confirm that no holes were present within the seal.

The starting bulk composition was then added to the 'toothpaste-tube' like capsule. A gap approximately 3 mm deep was left to allow for sufficient space for the top of the capsule to be welded. The top of the cylindrical tube was welded closed in the same manner as the base. The diameter and length of each of the capsules was approximately 10mm by 5mm. The entire procedure was then repeated for each experiment.

### ***Experimental Apparatus***

A cold seal pressure vessel was used to expose the gold capsule (containing the synthetic gel and peritectic minerals) to approximate granulite facies conditions (700 - 800°C and ~2kbar) during experimentation. A Marshall Furnace (Series 1100) was utilized as it has a maximum temperature of 1200°C. These temperatures are generated by a series of heavy gauge nickel-chrome wires coiled around a ceramic tube. This tube sits in a mullite muffle that acts as an insulator and helps regulate and maintain a uniform temperature across the furnace. The machine allows for a maximum voltage output of 110V. The system utilizes a Haskel air driven double acting pump, which generates the water pressure within the vessel. The air pressure within the system is monitored by a Bundenberg Standard Test gauge (lb/in<sup>2</sup>). The confining water pressure within the cold seal pressure vessel is monitored using a HEISE Pressure gauge, with a range of between 0-50 000 PSI. A digital Temperature Controller measured the temperature at this point during experiments using a K -type thermocouple.

Before experiments could be conducted a 35cm long K-type thermocouple wire was marked in 1cm increments and placed cm-by-cm inside the furnace during a test run. This test run was run at a constant temperature of 300°C, and was not conducted under pressure. By measuring the temperature at each cm interval the hottest part or 'hot spot' of the furnace was found to be at a depth of 18cm. The portion of the Inconel vessel containing the gold capsule sat at this depth (18cm) during each experiment to ensure consistency.

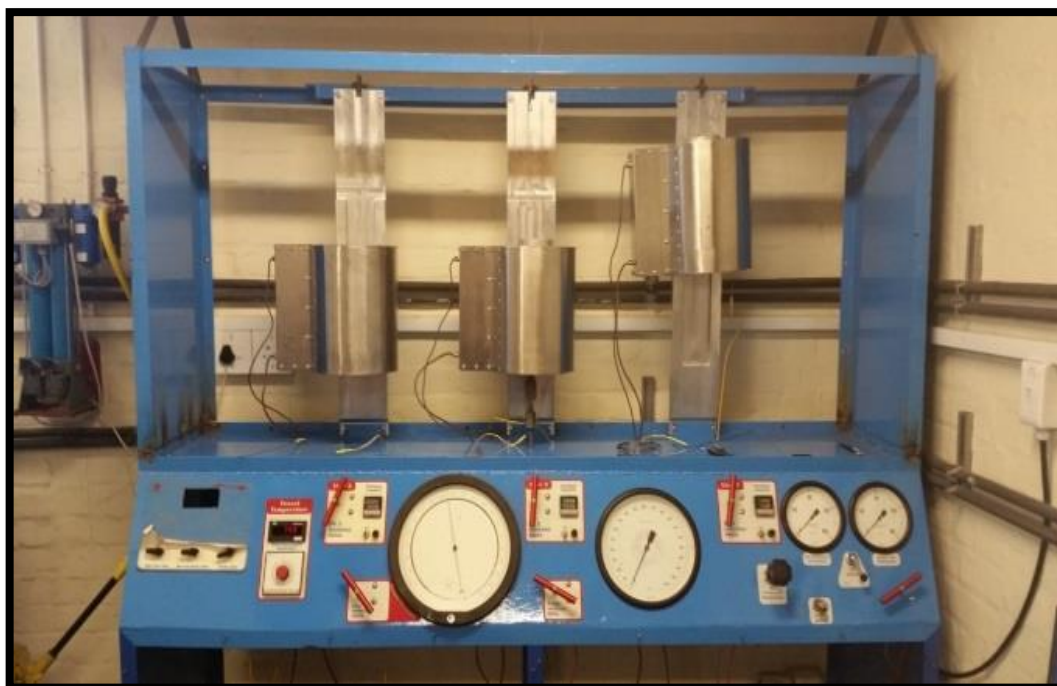


Figure 6 - Photograph of the Experimental Machinery

### ***Experimental Procedure***

A calibration experiment was conducted to determine the temperature gradient between the external and internal portion of the Inconel vessel. During the calibration experiment no gold capsule was placed within the vessel. In order to measure the internal temperature of the Inconel vessel a 40cm K-type thermocouple was wired through the entire apparatus. Care was taken to ensure that the tip of this K-type thermocouple was located at the same point as a gold capsule would have been during a routine experimental setup (~18cm depth).

The calibration experiment required a setup whereby a K-type thermocouple needed to be placed through and silver soldered to a steel cone. The steel cone acted as a seal to prevent water leakages and ensured the pressure within the Inconel vessel remained constant during the calibration experiment. Once soldered, the steel cone and thermocouple were then placed through a steel T-piece attachment. The T-piece attachment was then screwed into the base of the experimental platform (underneath a hole in the platform), allowing the thermocouple to be exposed above the experimental platform. The cold seal pressure components, including the Inconel vessel, were then placed over the thermocouple and tightened with a wrench (Figure 7, overleaf).

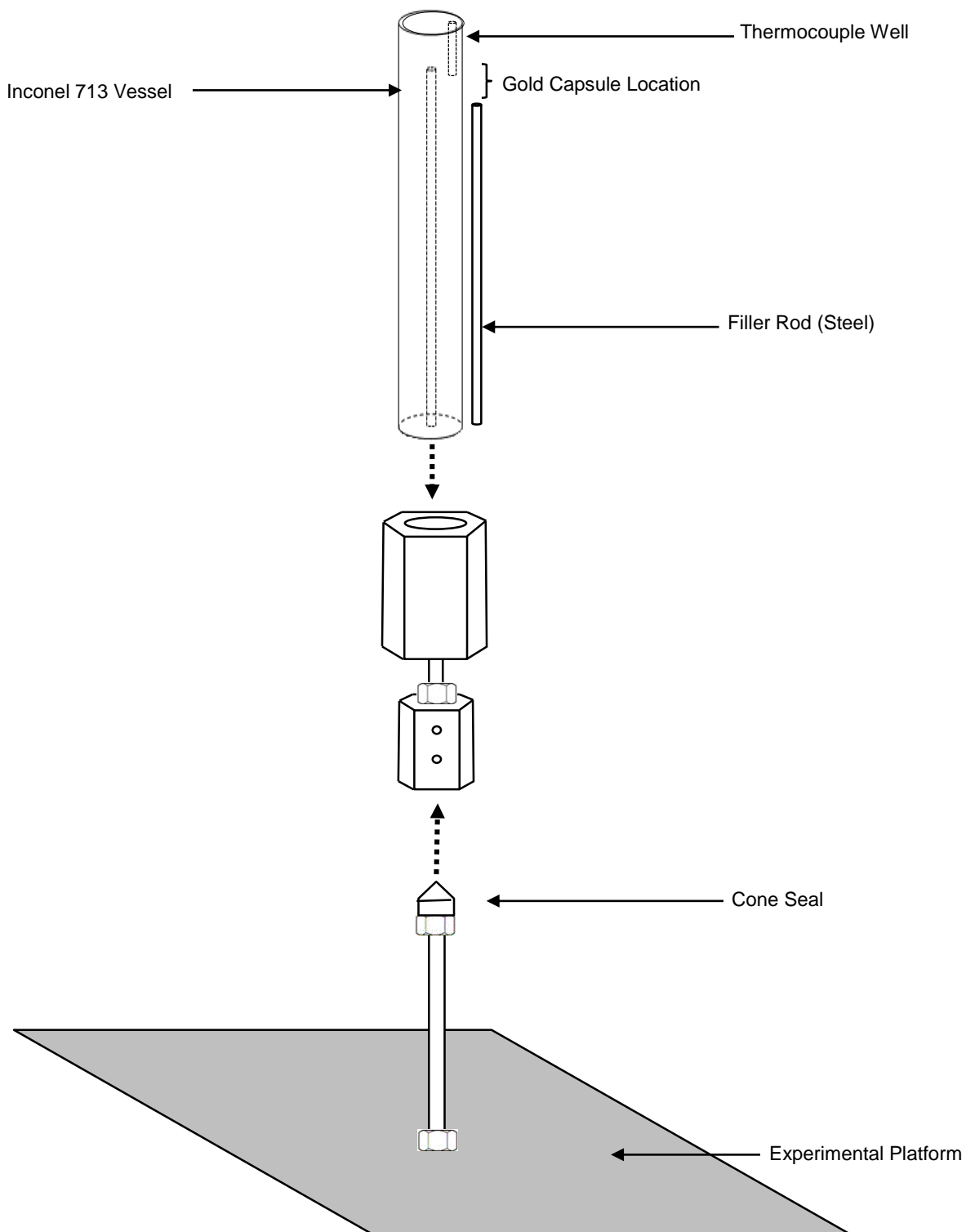


Figure 7 - Schematic of the Standard Cold-Seal Pressure Vessel Set-up

## CHAPTER 4: EXPERIMENTAL DESIGN

An initial calibration experiment was conducted where the Inconel vessel was placed over the thermocouple without a steel filler rod inside it. A 35cm K-type thermocouple was placed into the external thermocouple well, located at the top of the Inconel vessel. The furnace was then placed over the vessel, coming to rest just above the 'cone seal', which forms the cold seal portion of the apparatus. The pressure and temperature conditions of this initial calibration experiment were 1 kbar and 700-780°C (tested in 20°C intervals). The results of this initial calibration experiment are shown below.

**Table 4 - Calibration Experiment Results (Test 1)**

<b>Furnace Control T (°C)</b>	<b>Internal T (°C)</b>	<b>P (kbar)</b>	<b>External T (°C)</b>	<b>Difference (°C)</b>
725	681	1.00	701	20
735	704	1.00	721	17
756	724	1.00	741	17
775	744	1.00	761	17
793	765	1.00	781	16

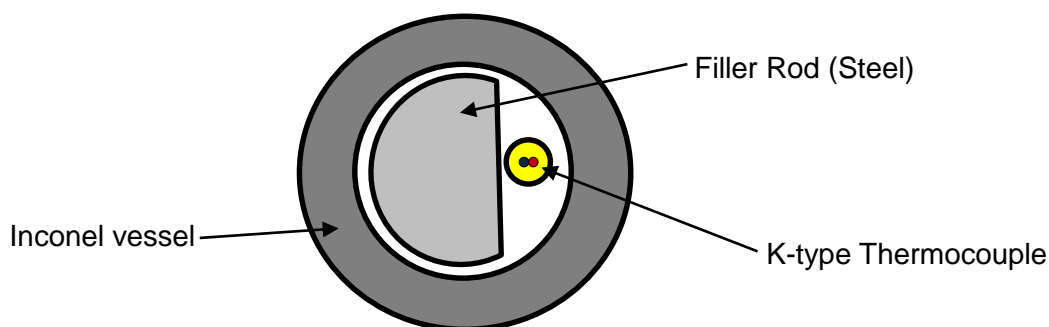
It is evident from the table above that there is a significant discrepancy between the external and internal thermocouple readings (average = 17.4°C). It was initially thought that the absence of a filler rod allowed for the redistribution of heat between the cooler base and the hotter upper portion of the Inconel vessel. It was thought that the constant convection of water around the inside of the vessel was causing this problem, and that a filler rod would reduce the heat loss associated with this convection. As a result a second calibration experiment was conducted to confirm and validate the accuracy of the initial calibration experiment's results.

In this second calibration test a filler rod was used inside the Inconel vessel. The cylindrical steel filler rod needed to be filed down to create a flat side that would allow for the 40 cm K-type thermocouple to fit alongside it within the Inconel vessel (Figure 8, overleaf) The rod was filed down using a steel file. The base of the rod was also filed down (Figure 9, pg.46) to prevent the thermocouple from being crushed when the Inconel vessel was attached to the rest of the experimental setup. Instead this shape would mean that the thermocouple would bend minimally, but still be able to be pushed up the side of the filler rod. This step was considered to be appropriate, as the combined space taken up by the thermocouple and the filed steel rod is equivalent to the space taken up by an unfiled steel filler rod during a standard experiment. The results of this second calibration experiment are shown overleaf.

**Table 5 - Calibration Experiment Results (Test 2)**

Furnace Control T (°C)	Internal T (°C)	P (kbar)	External T (°C)	Difference (°C)
725	680	1.00	700	20
734	703	1.00	721	18
748	724	1.00	741	17
770	744	1.00	743	17
790	764	1.00	780	16

From the results of the second calibration experiment it was determined that the temperature difference between the external and internal temperature of the Inconel vessel of a cold seal pressure differs on average by  $\sim 17^{\circ}\text{C}$ . It was also determined that the filler rod had no effect on the redistribution of heat within the vessel by convection processes. Temperature adjustments were made in future experiments to accommodate the temperature discrepancies of the internal and external parts of Inconel vessel. The reader should also note that relevant higher temperature experiments were unable to be conducted due to the pressure-temperature limitations of the cold seal-pressure vessel.

**Figure 8 - Cross-section of Inconel vessel (Calibration Experiment – Test 2)**



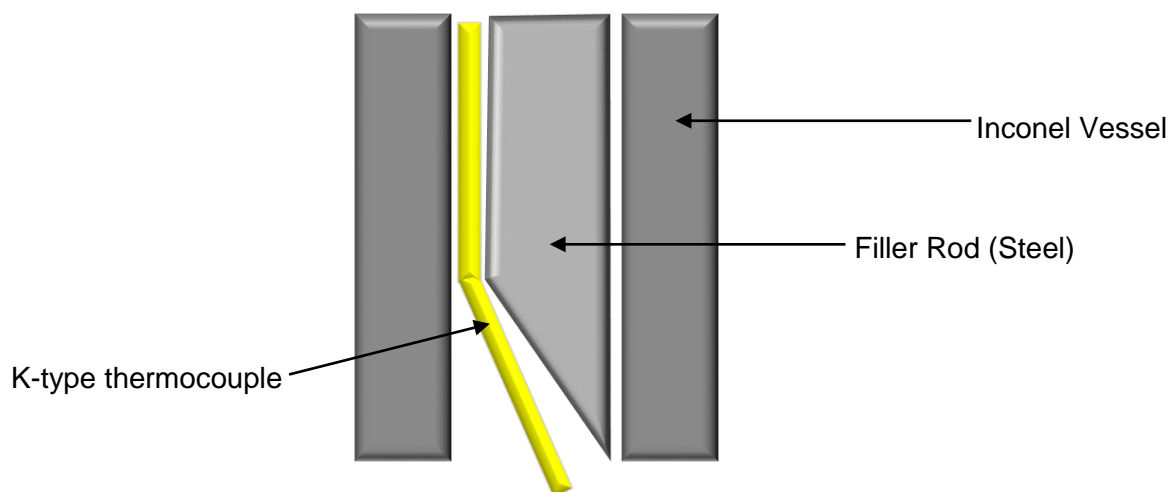


**Figure 9 - Side profile of Inconel vessel base (Calibration Experiment – Test 2)**

Standard experiments were conducted in a similar manner to the calibration experiments. In the standard experiments the gold capsules containing the starting bulk composition were used. These gold capsules were held in place by an unfired steel filler rod within the Inconel vessel. No internal thermocouple was used during the standard experimental set-up, instead the temperature was monitored by an external 35cm K-type thermocouple that sat in the thermocouple well at the top of the Inconel vessel. Temperature and pressure readings were recorded daily during the 10 day period of experimentation. These temperature readings were then later adjusted by 17°C due to temperature discrepancies within the set-up. Upon completion each experiment was quenched. During quenching solidus temperatures were reached in under a minute. The furnace was lifted from around the Inconel vessel. The Inconel vessel was then further cooled using compressed air and water to bring the vessel down to 60°C, allowing for the gold capsule to be removed from the Inconel vessel. The gold capsule was weighed before and after experimentation to ensure that there were no leaks in the capsule during the experimental run. The gold capsules were cut open using scissors and the contents were carefully removed using tweezers and placed into labelled plastic vials for later analysis.

## Chapter 5: Results

The results section is subdivided into three main subsections. The subsection below (5.1) presents the experimental mineral and melt compositions in comprehensive tables. The section thereafter (Textures in the Experimental Run Products, pg. 61) shows BSE images taken using the Zeiss® SEM show the mineral textures produced by experimentation. Finally, the 'Mineral and Textural Descriptions' (pg. 67) section provides the reader with a detailed discussion of the compositional and textural features of the experimental run products.

**Table 6 - Experimental PT Conditions and Mineral Assemblages**

Experiment	P (kbar)	Dev.	T (°C)	Dev.	Experimental Mineral Assemblages
1	1.90	0.0	733	1.0	Pl + Ilm + Cpx + Bt + LIQ + Qtz
2	1.90	0.0	763	2.0	Pl + Ilm + Grt + Bt + Opx + Cpx + LIQ + Qtz
3	1.90	0.0	723	2.0	Pl + Bt + Grt + Opx + Cam + Cpx + LIQ + H <sub>2</sub> O + Qtz
4	1.40	0.0	743	1.0	Pl + Ilm + Cpx + Grt + Cam + Bt + LIQ + H <sub>2</sub> O + Qtz
5	1.40	0.0	730	1.0	Pl + Grt + Ilm + Cpx + Cam + Bt + LIQ + H <sub>2</sub> O + Qtz

\*Metastable phases are indicated in red.

## 5.1 Mineral and Melt Compositions

**Table 7 - Peritectic Assemblage Mineral Compositions**

	<b>Grt</b>	<b>Pl</b>	<b>Opx</b>	<b>Cpx</b>	<b>Ilm</b>
<i>SiO<sub>2</sub></i>	37.95	59.05	51.86	52.66	0.00
<i>TiO<sub>2</sub></i>	0.00	0.00	0.00	0.00	50.10
<i>Al<sub>2</sub>O<sub>3</sub></i>	21.91	25.54	3.97	2.55	0.00
<i>Cr<sub>2</sub>O<sub>3</sub></i>	0.00	0.00	0.00	0.88	0.00
<i>Fe<sub>2</sub>O<sub>3</sub></i>	0.92	0.00	1.06	0.00	4.66
<i>FeO</i>	30.13	0.00	20.06	7.84	44.24
<i>MnO</i>	0.54	0.00	0.00	0.00	0.99
<i>MgO</i>	6.21	0.00	22.20	18.14	0.37
<i>CaO</i>	2.64	7.21	0.00	17.64	0.00
<i>Na<sub>2</sub>O</i>	0.00	7.41	0.00	0.00	0.00
<i>K<sub>2</sub>O</i>	0.00	0.29	0.00	0.00	0.00
<i>Total</i>	100.29	99.50	99.16	99.70	100.34
<i>Si</i>	2.97	2.65	1.94	1.94	0.00
<i>Ti</i>	0.00	0.00	0.00	0.00	0.95
<i>Al</i>	2.02	1.35	0.17	0.11	0.00
<i>Cr</i>	0.00	0.00	0.00	0.03	0.00
<i>Fe<sup>3+</sup></i>	0.05	0.00	0.03	0.00	0.09
<i>Fe<sup>2+</sup></i>	1.97	0.00	0.63	0.24	0.94
<i>Mn</i>	0.04	0.00	0.00	0.00	0.02
<i>Mg</i>	0.72	0.00	1.24	0.99	0.01
<i>Ca</i>	0.22	0.35	0.00	0.69	0.00
<i>Na</i>	0.00	0.64	0.00	0.00	0.00
<i>K</i>	0.00	0.02	0.00	0.00	0.00
<i>Sum</i>	8.00	5.01	4.00	4.00	2.00
<i>Mg#</i>	26.28	0.00	65.26	80.49	0.96
<i>X<sub>An</sub><sup>a</sup></i>	-	34.39	-	-	-
<i>X<sub>Ab</sub><sup>b</sup></i>	-	63.96	-	-	-
<i>X<sub>Or</sub><sup>c</sup></i>	-	1.65	-	-	-

$X_{Wo}^d$	-	-	0.00	-	-
$X_{En}^e$	-	-	66.36	-	-
$X_{Fs}^f$	-	-	33.64	-	-
$X_{Aeg}^g$	-	-	-	0.00	-
$X_{Jd}^h$	-	-	-	0.00	-
$X_{Di}^i$	-	-	-	100.00	-
$X_{Alm}^j$	67.36	-	-	-	-
$X_{Prp}^k$	24.09	-	-	-	-
$X_{Grs}^l$	7.36	-	-	-	-
$X_{Sps}^m$	1.19	-	-	-	-

<sup>a</sup> $X_{An} = (Ca/(Ca + Na + K)) * 100$     <sup>b</sup> $X_{Ab} = (Na/(Ca + Na + K)) * 100$     <sup>c</sup> $X_{Or} = (K/(Ca + Na + K)) * 100$   
<sup>d</sup> $X_{Wo} = (Ca/Ca + Mg + FeT) * 100$     <sup>e</sup> $X_{En} = (Mg/Ca + Mg + FeT) * 100$     <sup>f</sup> $X_{Fs} = (FeT/Ca + Mg + FeT) * 100$   
<sup>g</sup> $X_{Aeg} = (Fe^{3+} * (Fe^{3+} + (Na-Fe^{3+}) + Ca)) * 100$     <sup>h</sup> $X_{Jd} = ((Na-Fe^{3+})/(Fe^{3+} + (Na-Fe^{3+}) + Ca)) * 100$     <sup>i</sup> $X_{Di} = (Ca/(Fe^{3+} + (Na-Fe^{3+}) + Ca)) * 100$   
<sup>j</sup> $X_{Alm} = (FeT/(Ca + Mg + Mn + Fe)) * 100$     <sup>k</sup> $X_{Prp} = (Mg/(Ca + Mg + Mn + FeT)) * 100$     <sup>l</sup> $X_{Grs} = (Ca/(Ca + Mg + Mn + FeT)) * 100$     <sup>m</sup> $X_{Sps} = (Mn/(Ca + Mg + Mn + FeT)) * 100$   
Fe<sup>3+</sup> calculated using Droop (1987)  
Mg# = 100 \* (Mg/(Mg + Fe<sup>2+</sup> + Fe<sup>3+</sup>))

## CHAPTER 5: RESULTS

**Table 8 - Experiment 1 Average Mineral Compositions**

<u>Pressure</u>	1.90kbar									
<u>Temperature</u>	733°C									
<u>Duration</u>	10 days									
	Melt		Pl		Cpx				Ilm	
					Core		Rim			
	n= 15	$\sigma$	n= 7	$\sigma$	n=6	$\sigma$	n=7	$\sigma$	n=7	$\sigma$
<i>SiO<sub>2</sub></i>	69.45	1.2	58.91	0.4	52.36	0.2	51.99	0.9	0.07	0.0
<i>TiO<sub>2</sub></i>	0.00	0.0	0.00	0.0	0.05	0.0	0.35	0.1	50.08	0.5
<i>Al<sub>2</sub>O<sub>3</sub></i>	12.27	0.3	25.53	0.2	2.55	0.1	1.84	0.2	0.00	0.0
<i>Cr<sub>2</sub>O<sub>3</sub></i>	0.00	0.0	0.00	0.0	1.10	0.0	0.54	0.3	0.00	0.0
<i>Fe<sub>2</sub>O<sub>3</sub></i>	0.00	0.0	0.00	0.0	0.00	0.0	1.45	0.0	7.39	0.0
<i>FeO</i>	0.60	0.1	0.05	0.0	5.64	0.2	9.26	0.5	39.30	0.0
<i>MnO</i>	0.00	0.0	0.00	0.0	0.00	0.0	0.69	0.1	2.57	0.1
<i>MgO</i>	0.00	0.0	0.00	0.0	15.59	0.2	11.59	0.3	1.81	0.1
<i>CaO</i>	0.54	0.0	7.53	0.4	22.41	0.3	21.87	0.4	0.00	0.0
<i>Na<sub>2</sub>O</i>	2.57	0.3	6.98	0.4	0.06	0.0	0.73	0.1	0.00	0.0
<i>K<sub>2</sub>O</i>	4.53	0.2	0.48	0.2	0.00	0.0	0.15	0.0	0.00	0.0
<i>Total</i>	89.96	1.1	99.48	0.4	99.76	0.6	100.46	0.7	101.22	0.5
<i>Si</i>	-	-	2.65	-	1.94	-	1.95	-	0.00	-
<i>Ti</i>	-	-	0.00	-	0.00	-	0.01	-	0.93	-
<i>Al</i>	-	-	1.35	-	0.11	-	0.08	-	0.00	-
<i>Cr</i>	-	-	0.00	-	0.03	-	0.02	-	0.00	-
<i>Fe<sup>3+</sup></i>	-	-	0.00	-	0.00	-	0.04	-	0.14	-
<i>Fe<sup>2+</sup></i>	-	-	0.00	-	0.17	-	0.29	-	0.81	-
<i>Mn</i>	-	-	0.00	-	0.00	-	0.02	-	0.07	-
<i>Mg</i>	-	-	0.00	-	0.86	-	0.65	-	0.05	-
<i>Ca</i>	-	-	0.36	-	0.89	-	0.88	-	0.00	-
<i>Na</i>	-	-	0.61	-	0.00	-	0.05	-	0.00	-
<i>K</i>	-	-	0.03	-	0.00	-	0.01	-	0.00	-
<i>Sum</i>	-	-	5.00	-	4.00	-	4.00	-	2.00	-
<i>Mg#</i>	-	-	0.00	-	83.13	-	66.18	-	5.00	-

$X_{An}^a$	-	-	36.32	-	-	-	-	-	-	-
$X_{Ab}^b$	-	-	60.92	-	-	-	-	-	-	-
$X_{Or}^c$	-	-	2.76	-	-	-	-	-	-	-
$X_{Wo}^a$	-	-	-	-	-	-	-	-	-	-
$X_{En}^b$	-	-	-	-	-	-	-	-	-	-
$X_{Fs}^c$	-	-	-	-	-	-	-	-	-	-
$X_{Aeg}^d$	-	-	-	-	0.00	-	0.00	-	-	-
$X_{Jd}^e$	-	-	-	-	0.48	-	5.70	-	-	-
$X_{Di}^f$	-	-	-	-	99.52	-	94.30	-	-	-
$X_{Alm}^j$	-	-	-	-	-	-	-	-	-	-
$X_{Prp}^k$	-	-	-	-	-	-	-	-	-	-
$X_{Grs}^l$	-	-	-	-	-	-	-	-	-	-
$X_{Sps}^m$	-	-	-	-	-	-	-	-	-	-

$$^aX_{An} = (Ca/(Ca + Na + K)) * 100$$

$$^bX_{Ab} = (Na/(Ca + Na + K)) * 100$$

$$^cX_{Or} = (K/(Ca + Na + K)) * 100$$

$$^dX_{Wo} = (Ca/Ca + Mg + FeT) * 100$$

$$^eX_{En} = (Mg/Ca + Mg + FeT) * 100$$

$$^fX_{Fs} = (FeT/Ca + Mg + FeT) * 100$$

$$^gX_{Aeg} = (Fe^{3+} * (Fe^{3+} + (Na-Fe^{3+}) + Ca)) * 100$$

$$^hX_{Jd} = (Na-Fe^{3+}) / (Fe^{3+} + (Na-Fe^{3+}) + Ca) * 100$$

$$^iX_{Di} = (Ca / (Fe^{3+} + (Na-Fe^{3+}) + Ca)) * 100$$

$$^jX_{Alm} = (FeT / (Ca + Mg + Mn + FeT)) * 100$$

$$^kX_{Prp} = (Mg / (Ca + Mg + Mn + FeT)) * 100$$

$$^lX_{Grs} = (Ca / (Ca + Mg + Mn + FeT)) * 100$$

$$^mX_{Sps} = (Mn / (Ca + Mg + Mn + FeT)) * 100$$

Fe<sup>3+</sup> calculated using Droop (1987)

$$Mg\# = 100 * (Mg / (Mg + Fe^{2+} + Fe^{3+}))$$

## CHAPTER 5: RESULTS

**Table 9 - Experiment 2 Average Mineral Compositions**

<u>Pressure</u>	1.90 kbar											
<u>Temperature</u>	763°C											
<u>Duration</u>	10 days											
	<b>Melt</b>		<b>Grt</b>		<b>Pl</b>		<b>Opx</b>		<b>Cpx</b>		<b>Ilm</b>	
	n=21	Σ	n=5	σ	n=4	σ	n=3	σ	n=6	σ	n=5	σ
<i>SiO<sub>2</sub></i>	71.24	0.9	38.86	0.2	56.58	3.9	54.30	0.2	52.23	0.2	0.07	0.0
<i>TiO<sub>2</sub></i>	0.00	0.0	0.00	0.0	0.04	0.1	0.00	0.0	0.26	0.0	50.08	1.2
<i>Al<sub>2</sub>O<sub>3</sub></i>	11.26	0.2	21.96	0.2	27.39	2.3	1.79	0.0	2.48	0.1	0.00	0.0
<i>Cr<sub>2</sub>O<sub>3</sub></i>	0.00	0.0	0.22	0.1	0.07	0.1	0.39	0.0	1.78	0.1	0.00	0.0
<i>Fe<sub>2</sub>O<sub>3</sub></i>	0.00	0.0	0.70	0.0	0.00	0.0	1.51	0.0	0.00	0.0	8.89	0.0
<i>FeO</i>	0.60	0.1	26.85	0.2	0.31	0.2	12.39	0.4	6.71	0.5	37.95	1.1
<i>MnO</i>	0.00	0.0	0.00	0.0	0.00	0.0	0.54	0.1	0.00	0.0	2.57	0.1
<i>MgO</i>	0.00	0.0	8.30	0.0	0.07	0.1	28.09	0.4	16.96	0.7	1.81	0.2
<i>CaO</i>	0.69	0.1	3.52	0.1	10.08	2.2	0.88	0.0	19.45	1.0	0.00	0.0
<i>Na<sub>2</sub>O</i>	2.03	0.1	0.00	0.0	4.59	1.4	0.00	0.0	0.26	0.1	0.00	0.0
<i>K<sub>2</sub>O</i>	3.96	0.1	0.00	0.0	0.75	0.5	0.00	0.0	0.00	0.0	0.00	0.0
<i>Total</i>	89.78	1.2	100.41	0.4	99.87	0.4	99.89	0.4	100.13	0.3	101.37	0.2
<i>Si</i>	-	-	2.99	-	2.73	-	1.95	-	1.92	-	0.00	-
<i>Ti</i>	-	-	0.00	-	0.00	-	0.00	-	0.01	-	0.91	-
<i>Al</i>	-	-	1.99	-	1.56	-	0.07	-	0.11	-	0.00	-
<i>Cr</i>	-	-	0.01	-	0.00	-	0.01	-	0.05	-	0.00	-
<i>Fe<sup>3+</sup></i>	-	-	0.04	-	0.00	-	0.04	-	0.00	-	0.18	-
<i>Fe<sup>2+</sup></i>	-	-	1.73	-	0.01	-	0.37	-	0.21	-	0.84	-
<i>Mn</i>	-	-	0.00	-	0.00	-	0.02	-	0.00	-	0.06	-
<i>Mg</i>	-	-	0.95	-	0.01	-	1.50	-	0.93	-	0.02	-
<i>Ca</i>	-	-	0.29	-	0.52	-	0.03	-	0.77	-	0.00	-
<i>Na</i>	-	-	0.00	-	0.09	-	0.00	-	0.02	-	0.00	-
<i>K</i>	-	-	0.00	-	0.07	-	0.00	-	0.00	-	0.00	-
<i>Sum</i>	-	-	8.00	-	5.00	-	4.00	-	4.00	-	2.00	-
<i>Mg#</i>	-	-	34.99	-	0.00	-	78.45	-	81.84	-	1.92	-
<i>X<sub>An</sub><sup>a</sup></i>	-	-	-	-	52.58	-	-	-	-	-	-	-

$X_{Ab}^b$	-	-	-	-	43.08	-	-	-	-	-	-	-
$X_{Or}^c$	-	-	-	-	4.63	-	-	-	-	-	-	-
$X_{Wo}^d$	-	-	-	-	-	-	1.77	-	-	-	-	-
$X_{En}^e$	-	-	-	-	-	-	78.74	-	-	-	-	-
$X_{Fs}^f$	-	-	-	-	-	-	19.48	-	-	-	-	-
$X_{Aeg}^g$	-	-	-	-	-	-	-	-	1.49	-	-	-
$X_{Jd}^h$	-	-	-	-	-	-	-	-	0.87	-	-	-
$X_{Di}^i$	-	-	-	-	-	-	-	-	97.64	-	-	-
$X_{Alm}^j$	-	-	58.74	-	-	-	-	-	-	-	-	-
$X_{Prp}^k$	-	-	31.62	-	-	-	-	-	-	-	-	-
$X_{Grs}^l$	-	-	9.64	-	-	-	-	-	-	-	-	-
$X_{Sps}^m$	-	-	0.00	-	-	-	-	-	-	-	-	-

$${}^aX_{An} = (\text{Ca}/(\text{Ca} + \text{Na} + \text{K})) * 100$$

$${}^bX_{Ab} = (\text{Na}/(\text{Ca} + \text{Na} + \text{K})) * 100$$

$${}^cX_{Or} = (\text{K}/(\text{Ca} + \text{Na} + \text{K})) * 100$$

$${}^dX_{Wo} = (\text{Ca}/(\text{Ca} + \text{Mg} + \text{FeT})) * 100$$

$${}^eX_{En} = (\text{Mg}/(\text{Ca} + \text{Mg} + \text{FeT})) * 100$$

$${}^fX_{Fs} = (\text{FeT}/(\text{Ca} + \text{Mg} + \text{FeT})) * 100$$

$${}^gX_{Aeg} = (\text{Fe}^{3+} * (\text{Fe}^{3+} + (\text{Na}-\text{Fe}^{3+}) + \text{Ca})) * 100$$

$${}^hX_{Jd} = (\text{Na}-\text{Fe}^{3+})/(\text{Fe}^{3+} + (\text{Na}-\text{Fe}^{3+}) + \text{Ca}) * 100$$

$${}^iX_{Di} = (\text{Ca}/(\text{Fe}^{3+} + (\text{Na}-\text{Fe}^{3+}) + \text{Ca})) * 100$$

$${}^jX_{Alm} = (\text{FeT}/(\text{Ca} + \text{Mg} + \text{Mn} + \text{FeT})) * 100$$

$${}^kX_{Prp} = (\text{Mg}/(\text{Ca} + \text{Mg} + \text{Mn} + \text{FeT})) * 100$$

$${}^lX_{Grs} = (\text{Ca}/(\text{Ca} + \text{Mg} + \text{Mn} + \text{FeT})) * 100$$

$${}^mX_{Sps} = (\text{Mn}/(\text{Ca} + \text{Mg} + \text{Mn} + \text{FeT})) * 100$$

Fe<sup>3+</sup> calculated using Droop (1987)

$$\text{Mg\#} = 100 * (\text{Mg}/(\text{Mg} + \text{Fe}^{2+} + \text{Fe}^{3+}))$$

Metastable mineral data is red.



## CHAPTER 5: RESULTS

**Table 10 - Experiment 3 Average Mineral Compositions**

<u>Pressure</u>	1.90 kbar									
<u>Temperature</u>	723°C									
<u>Duration</u>	10 days									
	<b>Melt</b>		<b>Pl</b>		<b>Cpx</b>		<b>Opx</b>		<b>Grt</b>	
	n=10	$\sigma$	n= 6	$\sigma$	n= 6	$\sigma$	n= 4	$\sigma$	n= 6	$\sigma$
<i>SiO<sub>2</sub></i>	71.61	1.1	59.84	0.2	52.74	0.5	52.06	0.2	38.95	0.2
<i>TiO<sub>2</sub></i>	0.00	0.0	0.00	0.0	0.36	0.0	0.00	0.0	0.00	0.0
<i>Al<sub>2</sub>O<sub>3</sub></i>	12.23	0.8	25.38	0.2	2.45	0.3	4.15	0.1	22.00	0.2
<i>Cr<sub>2</sub>O<sub>3</sub></i>	0.00	0.0	0.00	0.0	0.64	0.3	0.00	0.0	0.00	0.0
<i>Fe<sub>2</sub>O<sub>3</sub></i>	0.00	0.0	0.00	0.0	2.31	0.0	0.19	0.0	1.29	0.0
<i>FeO</i>	0.52	0.1	0.00	0.0	3.95	0.3	21.11	0.1	25.46	0.1
<i>MnO</i>	0.00	0.0	0.00	0.0	0.00	0.0	0.00	0.0	0.48	0.1
<i>MgO</i>	0.00	0.0	0.00	0.0	14.70	0.3	22.86	0.1	8.42	0.1
<i>CaO</i>	0.85	0.3	7.43	0.0	22.36	0.3	0.30	0.0	4.40	0.1
<i>Na<sub>2</sub>O</i>	2.51	0.4	7.28	0.1	0.99	0.5	0.00	0.0	0.00	0.0
<i>K<sub>2</sub>O</i>	3.75	0.3	0.46	0.0	0.00	0.0	0.00	0.0	0.00	0.0
<i>Total</i>	91.46	0.6	100.39	0.2	100.49	0.5	100.68	0.3	100.99	0.4
<i>Si</i>	-	-	2.66	-	1.93	-	1.91	-	2.97	-
<i>Ti</i>	-	-	0.00	-	0.01	-	0.00	-	0.00	-
<i>Al</i>	-	-	1.33	-	0.11	-	0.18	-	1.98	-
<i>Cr</i>	-	-	0.00	-	0.01	-	0.00	-	0.00	-
<i>Fe<sup>3+</sup></i>	-	-	0.00	-	0.06	-	0.01	-	0.07	-
<i>Fe<sup>2+</sup></i>	-	-	0.00	-	0.12	-	0.65	-	1.63	-
<i>Mn</i>	-	-	0.00	-	0.00	-	0.00	-	0.03	-
<i>Mg</i>	-	-	0.00	-	0.80	-	1.25	-	0.96	-
<i>Ca</i>	-	-	0.35	-	0.88	-	0.01	-	0.36	-
<i>Na</i>	-	-	0.63	-	0.07	-	0.00	-	0.00	-
<i>K</i>	-	-	0.03	-	0.00	-	0.00	-	0.00	-
<i>Sum</i>	-	-	5.00	-	4.00	-	4.00	-	8.00	-
<i>Mg#</i>	-	-	0.00	-	81.32	-	65.68	-	36.09	-
<i>X<sub>An</sub><sup>a</sup></i>	-	-	35.13	-	-	-	-	-	-	-

$X_{Ab}^b$	-	-	62.28	-	-	-	-	-	-	-
$X_{Or}^c$	-	-	2.59	-	-	-	-	-	-	-
$X_{Wo}^d$	-	-	-	-	-	-	0.62	-	-	-
$X_{En}^e$	-	-	-	-	-	-	65.47	-	-	-
$X_{Fs}^f$	-	-	-	-	-	-	33.92	-	-	-
$X_{Aeg}^g$	-	-	-	-	0.01	-	-	-	-	-
$X_{Jd}^h$	-	-	-	-	7.40	-	-	-	-	-
$X_{Di}^i$	-	-	-	-	92.58	-	-	-	-	-
$X_{Alm}^j$	-	-	-	-	-	-	-	-	55.75	-
$X_{Prp}^k$	-	-	-	-	-	-	-	-	31.43	-
$X_{Grs}^l$	-	-	-	-	-	-	-	-	11.80	-
$X_{Sps}^m$	-	-	-	-	-	-	-	-	1.02	-

$^aX_{An} = (Ca/(Ca + Na + K)) * 100$      $^bX_{Ab} = (Na/(Ca + Na + K)) * 100$      $^cX_{Or} = (K/(Ca + Na + K)) * 100$   
 $^dX_{Wo} = (Ca/Ca + Mg + FeT) * 100$      $^eX_{En} = (Mg/Ca + Mg + FeT) * 100$      $^fX_{Fs} = (FeT/Ca + Mg + FeT) * 100$   
 $^gX_{Aeg} = (Fe^{3+} * (Fe^{3+} + (Na-Fe^{3+}) + Ca)) * 100$      $^hX_{Jd} = (Na-Fe^{3+}) / (Fe^{3+} + (Na-Fe^{3+}) + Ca) * 100$      $^iX_{Di} = (Ca / (Fe^{3+} + (Na-Fe^{3+}) + Ca)) * 100$   
 $^jX_{Alm} = (FeT / (Ca + Mg + Mn + FeT)) * 100$      $^kX_{Prp} = (Mg / (Ca + Mg + Mn + FeT)) * 100$      $^lX_{Grs} = (Ca / (Ca + Mg + Mn + FeT)) * 100$      $^mX_{Sps} = (Mn / (Ca + Mg + Mn + FeT)) * 100$   
 $Fe^{3+}$  calculated using Droop (1987)  
 $Mg\# = 100 * (Mg / (Mg + Fe^{2+} + Fe^{3+}))$   
 Metastable mineral data is red.

## CHAPTER 5: RESULTS

**Table 11 - Experiment 4 Average Mineral Compositions**

<u>Pressure</u>	1.40 kbar											
<u>Temperature</u>	743°C											
<u>Duration</u>	10 days											
	Melt		Grt		Ilm		Pl		Cpx (1)		Cpx (2)	
	n= 14	$\Sigma$	n= 12	$\sigma$	n= 3	$\sigma$	n= 7	$\sigma$	n= 8	$\sigma$	n= 7	$\sigma$
<i>SiO<sub>2</sub></i>	71.15	0.8	38.14	0.3	6.40	0.7	59.98	0.8	52.77	0.6	52.37	0.4
<i>TiO<sub>2</sub></i>	0.00	0.0	0.00	0.0	23.23	0.7	0.00	0.0	0.32	0.0	0.33	0.0
<i>Al<sub>2</sub>O<sub>3</sub></i>	11.33	0.2	21.71	0.2	1.46	0.1	25.34	0.1	2.34	0.2	2.90	0.3
<i>Cr<sub>2</sub>O<sub>3</sub></i>	0.00	0.0	0.00	0.0	0.00	0.0	0.00	0.0	0.92	0.1	1.13	0.1
<i>Fe<sub>2</sub>O<sub>3</sub></i>	0.00	0.0	0.68	0.0	44.78	0.0	0.00	0.0	0.71	0.0	0.00	0.0
<i>FeO</i>	0.51	0.1	30.36	0.3	25.79	0.4	0.00	0.0	9.05	1.7	5.51	0.3
<i>MnO</i>	0.00	0.0	0.43	0.1	0.00	0.0	0.00	0.0	0.47	0.0	0.00	0.0
<i>MgO</i>	0.00	0.0	6.48	0.1	1.10	0.1	0.00	0.0	20.77	2.2	15.68	0.4
<i>CaO</i>	0.69	0.1	2.55	0.1	0.00	0.0	7.34	0.2	13.14	3.7	22.07	0.8
<i>Na<sub>2</sub>O</i>	1.81	0.3	0.00	0.0	0.00	0.0	7.23	0.2	0.00	0.0	0.00	0.0
<i>K<sub>2</sub>O</i>	4.14	0.1	0.00	0.0	0.26	0.0	0.32	0.0	0.00	0.0	0.00	0.0
<i>Total</i>	89.63	0.9	100.34	0.7	103.03	0.5	100.21	0.6	100.49	0.5	99.98	0.7
<i>Si</i>	-	-	2.98	-	0.15	-	2.67	-	1.92	-	1.93	-
<i>Ti</i>	-	-	0.00	-	0.42	-	0.00	-	0.01	-	0.01	-
<i>Al</i>	-	-	2.00	-	0.04	-	1.33	-	0.10	-	0.13	-
<i>Cr</i>	-	-	0.00	-	0.00	-	0.00	-	0.02	-	0.02	-
<i>Fe<sup>3+</sup></i>	-	-	0.04	-	0.81	-	0.00	-	0.02	-	0.00	-
<i>Fe<sup>2+</sup></i>	-	-	1.98	-	0.52	-	0.00	-	0.28	-	0.17	-
<i>Mn</i>	-	-	0.03	-	0.00	-	0.00	-	0.01	-	0.00	-
<i>Mg</i>	-	-	0.75	-	0.04	-	0.00	-	1.13	-	0.86	-
<i>Ca</i>	-	-	0.21	-	0.00	-	0.35	-	0.51	-	0.87	-
<i>Na</i>	-	-	0.00	-	0.00	-	0.62	-	0.00	-	0.00	-
<i>K</i>	-	-	0.00	-	0.01	-	0.02	-	0.00	-	0.00	-
<i>Sum</i>	-	-	8.00	-	2.00	-	4.99	-	4.00	-	3.99	-
<i>Mg#</i>	-	-	27.15	-	2.89	-	0.00	-	79.25	-	83.54	-

$X_{An}^a$	-	-	-	-	-	-	35.28	-	-	-	-	-
$X_{Ab}^b$	-	-	-	-	-	-	62.89	-	-	-	-	-
$X_{Or}^c$	-	-	-	-	-	-	1.83	-	-	-	-	-
$X_{Wo}^d$	-	-	-	-	-	-	-	-	-	-	-	-
$X_{En}^e$	-	-	-	-	-	-	-	-	-	-	-	-
$X_{Fs}^f$	-	-	-	-	-	-	-	-	-	-	-	-
$X_{Aeg}^g$	-	-	-	-	-	-	-	-	0.00	-	0.00	-
$X_{Jd}^h$	-	-	-	-	-	-	-	-	0.00	-	0.00	-
$X_{Di}^i$	-	-	-	-	-	-	-	-	100.00	-	100.00	-
$X_{Alm}^j$	-	-	66.56	-	-	-	-	-	-	-	-	-
$X_{Prp}^k$	-	-	25.32	-	-	-	-	-	-	-	-	-
$X_{Grs}^l$	-	-	7.16	-	-	-	-	-	-	-	-	-
$X_{Sps}^m$	-	-	0.95	-	-	-	-	-	-	-	-	-

$^a X_{An} = (Ca / (Ca + Na + K)) * 100$      $^b X_{Ab} = (Na / (Ca + Na + K)) * 100$      $^c X_{Or} = (K / (Ca + Na + K)) * 100$   
 $^d X_{Wo} = (Ca / (Ca + Mg + FeT)) * 100$      $^e X_{En} = (Mg / (Ca + Mg + FeT)) * 100$      $^f X_{Fs} = (FeT / (Ca + Mg + FeT)) * 100$   
 $^g X_{Aeg} = (Fe^{3+} * (Fe^{3+} + (Na - Fe^{3+}) + Ca)) * 100$      $^h X_{Jd} = (Na - Fe^{3+}) / (Fe^{3+} + (Na - Fe^{3+}) + Ca) * 100$      $^i X_{Di} = (Ca / (Fe^{3+} + (Na - Fe^{3+}) + Ca)) * 100$   
 $^j X_{Alm} = (FeT / (Ca + Mg + Mn + FeT)) * 100$      $^k X_{Prp} = (Mg / (Ca + Mg + Mn + FeT)) * 100$      $^l X_{Grs} = (Ca / (Ca + Mg + Mn + FeT)) * 100$      $^m X_{Sps} = (Mn / (Ca + Mg + Mn + FeT)) * 100$   
 $Fe^{3+}$  calculated using Droop (1987)  
 $Mg\# = 100 * (Mg / (Mg + Fe^{2+} + Fe^{3+}))$   
 Metastable mineral data is red.

## CHAPTER 5: RESULTS

**Table 12 - Experiment 5 Average Mineral Compositions**

<u>Pressure</u>	1.40 kbar									
<u>Temperature</u>	730°C									
<u>Duration</u>	10 days									
	<b>Melt</b>		<b>Grt</b>		<b>Ilm</b>		<b>Pl</b>		<b>Cpx</b>	
	n= 19	$\sigma$	n= 11	$\sigma$	n= 6	$\sigma$	n= 5	$\sigma$	n= 6	$\sigma$
<i>SiO<sub>2</sub></i>	70.04	0.7	38.43	0.3	0.60	0.0	59.16	0.2	52.50	0.3
<i>TiO<sub>2</sub></i>	0.00	0.0	0.00	0.0	48.82	0.6	0.00	0.0	0.32	0.0
<i>Al<sub>2</sub>O<sub>3</sub></i>	11.07	0.3	21.63	0.2	0.00	0.0	25.89	0.2	2.46	0.1
<i>Cr<sub>2</sub>O<sub>3</sub></i>	0.00	0.0	0.00	0.0	0.00	0.0	0.00	0.0	0.67	0.1
<i>Fe<sub>2</sub>O<sub>3</sub></i>	0.00	0.0	1.39	0.0	8.95	0.0	0.00	0.0	0.00	0.0
<i>FeO</i>	0.61	0.1	26.83	0.2	38.86	0.7	0.00	0.0	6.99	1.0
<i>MnO</i>	0.00	0.0	0.40	0.1	1.88	0.1	0.00	0.0	0.53	0.0
<i>MgO</i>	0.00	0.0	7.43	0.2	2.17	0.1	0.00	0.0	17.14	1.1
<i>CaO</i>	0.58	0.1	4.26	0.1	0.00	0.0	7.26	0.1	19.50	2.2
<i>Na<sub>2</sub>O</i>	2.55	0.4	0.00	0.0	0.00	0.0	7.10	0.1	0.00	0.0
<i>K<sub>2</sub>O</i>	4.73	0.2	0.00	0.0	0.00	0.0	0.39	0.0	0.00	0.0
<i>Total</i>	89.58	1.3	100.38	0.7	101.27	0.4	99.81	0.3	100.12	0.4
<i>Si</i>	-	-	2.97	-	0.01	-	2.64	-	1.93	-
<i>Ti</i>	-	-	0.00	-	0.90	-	0.00	-	0.01	-
<i>Al</i>	-	-	1.97	-	0.00	-	1.36	-	0.11	-
<i>Cr</i>	-	-	0.00	-	0.00	-	0.00	-	0.01	-
<i>Fe<sup>3+</sup></i>	-	-	0.08	-	0.17	-	0.00	-	0.00	-
<i>Fe<sup>2+</sup></i>	-	-	1.74	-	0.80	-	0.00	-	0.21	-
<i>Mn</i>	-	-	0.03	-	0.04	-	0.00	-	0.02	-
<i>Mg</i>	-	-	0.86	-	0.08	-	0.00	-	0.94	-
<i>Ca</i>	-	-	0.35	-	0.00	-	0.35	-	0.77	-
<i>Na</i>	-	-	0.00	-	0.00	-	0.62	-	0.00	-
<i>K</i>	-	-	0.00	-	0.00	-	0.02	-	0.00	-
<i>Sum</i>	-	-	8.00	-	2.00	-	4.99	-	4.00	-
<i>Mg#</i>	-	-	32.05	-	7.61	-	0.00	-	81.38	-

$X_{An}^a$	-	-	-	-	-	-	35.29	-	-	-
$X_{Ab}^b$	-	-	-	-	-	-	62.45	-	-	-
$X_{Or}^c$	-	-	-	-	-	-	2.26	-	-	-
$X_{Wo}^d$	-	-	-	-	-	-	-	-	-	-
$X_{En}^e$	-	-	-	-	-	-	-	-	-	-
$X_{Fs}^f$	-	-	-	-	-	-	-	-	-	-
$X_{Aeg}^g$	-	-	-	-	-	-	-	-	0.00	-
$X_{Jd}^h$	-	-	-	-	-	-	-	-	0.00	-
$X_{Di}^i$	-	-	-	-	-	-	-	-	100.00	-
$X_{Alm}^j$	-	-	59.51	-	-	-	-	-	-	-
$X_{Prp}^k$	-	-	28.07	-	-	-	-	-	-	-
$X_{Grs}^l$	-	-	11.57	-	-	-	-	-	-	-
$X_{Sps}^m$	-	-	0.86	-	-	-	-	-	-	-

$^a X_{An} = (Ca / (Ca + Na + K)) * 100$      $^b X_{Ab} = (Na / (Ca + Na + K)) * 100$      $^c X_{Or} = (K / (Ca + Na + K)) * 100$   
 $^d X_{Wo} = (Ca / (Ca + Mg + FeT)) * 100$      $^e X_{En} = (Mg / (Ca + Mg + FeT)) * 100$      $^f X_{Fs} = (FeT / (Ca + Mg + FeT)) * 100$   
 $^g X_{Aeg} = (Fe^{3+} * (Fe^{3+} + (Na - Fe^{3+}) + Ca)) * 100$      $^h X_{Jd} = (Na - Fe^{3+}) / (Fe^{3+} + (Na - Fe^{3+}) + Ca) * 100$      $^i X_{Di} = (Ca / (Fe^{3+} + (Na - Fe^{3+}) + Ca)) * 100$   
 $^j X_{Alm} = (FeT / (Ca + Mg + Mn + FeT)) * 100$      $^k X_{Prp} = (Mg / (Ca + Mg + Mn + FeT)) * 100$      $^l X_{Grs} = (Ca / (Ca + Mg + Mn + FeT)) * 100$      $^m X_{Sps} = (Mn / (Ca + Mg + Mn + FeT)) * 100$   
 $Fe^{3+}$  calculated using Droop (1987)  
 $Mg\# = 100 * (Mg / (Mg + Fe^{2+} + Fe^{3+}))$   
 Metastable mineral data is red.

## CHAPTER 5: RESULTS

**Table 13 - Experimental Melt Average Compositions**

Experiment	Starting Melt	1		2		3		4		5		
Pressure (kbar)	-	1.90		1.90		1.90		1.40		1.40		
Temperature (°C)	-	733		763		723		743		730		
		$\sigma$	n=15	$\sigma$	n=21	$\sigma$	n=10	$\sigma$	n=14	$\sigma$	n=19	$\sigma$
<i>SiO<sub>2</sub></i>	75.74	-	77.20	1.2	79.35	0.9	78.30	1.0	79.38	0.8	78.19	0.7
<i>TiO<sub>2</sub></i>	0.12	-	0.00	0.0	0.00	0.0	0.00	0.0	0.00	0.0	0.00	0.0
<i>Al<sub>2</sub>O<sub>3</sub></i>	13.49	-	13.64	0.3	12.54	0.2	13.37	0.8	12.64	0.2	12.36	0.3
<i>Cr<sub>2</sub>O<sub>3</sub></i>	0.00	-	0.00	0.0	0.00	0.0	0.00	0.0	0.00	0.0	0.00	0.0
<i>Fe<sub>2</sub>O<sub>3</sub></i>	0.00	-	0.00	0.0	0.00	0.0	0.00	0.0	0.00	0.0	0.00	0.0
<i>FeO</i>	1.02	-	0.67	0.1	0.67	0.1	0.57	0.1	0.57	0.1	0.68	0.1
<i>MnO</i>	0.00	-	0.00	0.0	0.00	0.0	0.00	0.0	0.00	0.0	0.00	0.0
<i>MgO</i>	0.09	-	0.00	0.0	0.00	0.0	0.00	0.0	0.00	0.0	0.00	0.0
<i>CaO</i>	1.05	-	0.60	0.0	0.77	0.1	0.93	0.3	0.77	0.1	0.65	0.1
<i>Na<sub>2</sub>O</i>	3.74	-	2.86	0.3	2.26	0.1	2.74	0.4	2.02	0.3	2.85	0.4
<i>K<sub>2</sub>O</i>	4.76	-	5.04	0.2	4.41	0.1	4.10	0.3	4.62	0.1	5.28	0.2
<i>Total</i>	100	-	100	1.0	100	1.2	100	0.6	100	0.9	100	1.3
<i>Mg#<sup>a</sup></i>	0.00	-	0.00	-	0.00	-	0.00	-	0.00	-	0.00	-
<i>Na<sub>2</sub>O/CaO</i>	3.56	-	4.76	-	2.94	-	2.95	-	2.62	-	4.40	-
<i>K<sub>2</sub>O/Na<sub>2</sub>O</i>	1.27	-	1.76	-	1.95	-	1.49	-	2.29	-	1.85	-
<i>Ferro<sup>b</sup></i>	1.23	-	0.60	-	0.60	-	0.52	-	0.51	-	0.61	-
<i>A/NK<sup>c</sup></i>	1.59	-	1.73	-	1.87	-	1.95	-	1.90	-	1.52	-
<i>A/CNK<sup>d</sup></i>	1.41	-	1.61	-	1.69	-	1.72	-	1.71	-	1.41	-

<sup>a</sup>Mg# = 100 \* (MgO/(MgO + FeO))

<sup>b</sup>Ferro= TiO<sub>2</sub> + FeO + MgO + MnO

<sup>c</sup>A/NK = Al<sub>2</sub>O<sub>3</sub>/(Na<sub>2</sub>O + K<sub>2</sub>O)

<sup>d</sup>A/CNK = Al<sub>2</sub>O<sub>3</sub>/(CaO + Na<sub>2</sub>O + K<sub>2</sub>O)

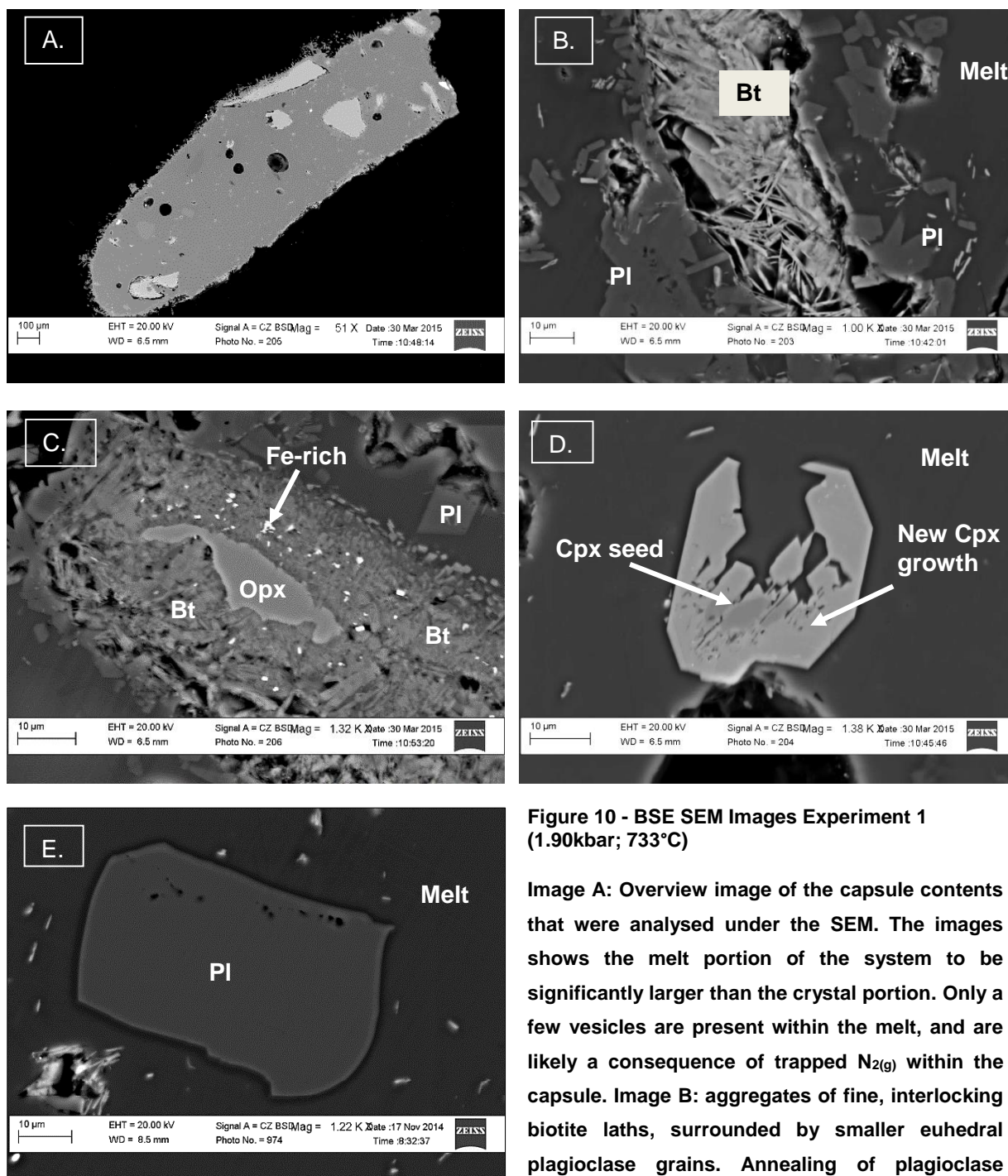
## 5.2 Textures in the Experimental Run Products

The following few pages illustrate the mineral textures that can be observed within the experimental run products. The minerals range in size (length) from ~2 - 400 $\mu\text{m}$  in all the experiments. The most noteworthy textures are the reaction rims of biotite that surround metastable garnet and metastable orthopyroxene, and the reaction rims of clin amphibole around clinopyroxene. These reaction rims vary in size (~2 - 10 $\mu\text{m}$ ) between differing experimental pressure and temperature conditions. Plagioclase displays evidence of melt and fluid inclusions, suggesting that the initial 'peritectic' plagioclase has dissolved and a new plagioclase phase has precipitated from the melts during the experimental runs. Clinopyroxene is the only mineral to demonstrate clear evidence of normal compositional zonation, which appears to indicate a coupled dissolution-precipitation mechanism is at work. All the experimental melts appear to contain vesicles. The vesicles are evidence of air trapped within the experimental capsule that contains components, such as  $\text{N}_{2(g)}$ , that are insoluble within the melt phase. In some cases these vesicles are shown to contain quenched hydrous crystals, which suggests that an  $\text{H}_2\text{O}$ -rich fluid existed within the system as a separate phase.



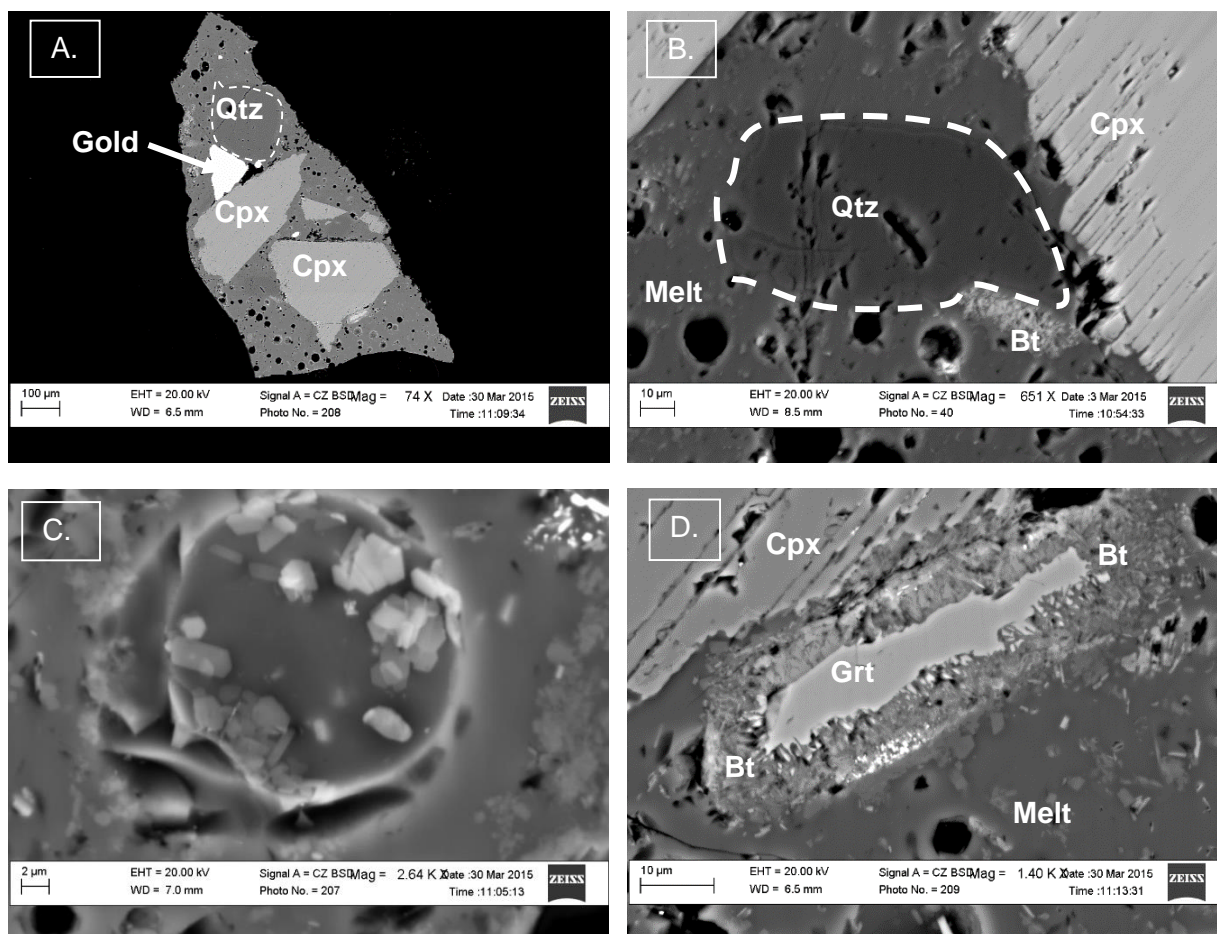
## CHAPTER 5: RESULTS

## Experiment 1 - 1.90kbar; 733°C



**Figure 10 - BSE SEM Images Experiment 1 (1.90kbar; 733°C)**

**Image A:** Overview image of the capsule contents that were analysed under the SEM. The images shows the melt portion of the system to be significantly larger than the crystal portion. Only a few vesicles are present within the melt, and are likely a consequence of trapped N<sub>2</sub>(g) within the capsule. **Image B:** aggregates of fine, interlocking biotite laths, surrounded by smaller euhedral plagioclase grains. Annealing of plagioclase grains appears to have occurred to produce larger, subhedral plagioclase crystals. **Image C:** anhedronal orthopyroxene crystal has reacted with the surrounding melt portion to produce a reaction rim of small, amorphous, biotite crystals. The lighter areas within the biotite reaction rim represent areas of Fe enrichment. **Image D:** zoned clinopyroxene, with the darker portion representing the initial 'peritectic' seed composition and the lighter portion representing new clinopyroxene growth. The rim of new clinopyroxene growth has a considerably lower Mg# than the core. This image also clearly shows the homogeneous nature of the surrounding melt portion. **Image E:** large (~50µm length), euhedral plagioclase grain containing melt/gas inclusions (<1µm).

**Experiment 2 - 1.90kbar; 763°C****Figure 11 - BSE SEM Images Experiment 2 (1.90kbar; 763°C)**

**Image A:** Overview image of the experimental run product, showing the reader the size and spatial relationships of the larger crystals, particularly clinopyroxene and quartz. **Image B:** clinopyroxene showing strong one directional cleavage. Rounded, magmatic quartz crystal also evident. The small area of biotite within the image likely indicates the complete replacement of either peritectic garnet/orthopyroxene. **Image C:** vesicles containing quenched, plagioclase crystals. Quench crystals were too small to analyse accurately under the SEM. **Image D:** reaction of metastable garnet with the surrounding melt to produce a reaction rim of a hydrous phase, specifically biotite. This experiment appears to contain a significantly larger crystal component compared to Experiment 1. The gold visible in Image A is a fragment of the capsule and is not a constituent of the experimental run product. The melt in this experiment is homogeneous, containing interspersed, sub- to anhedral plagioclase grains (<10µm).

## CHAPTER 5: RESULTS

## Experiment 3 - 1.90kbar; 723°C

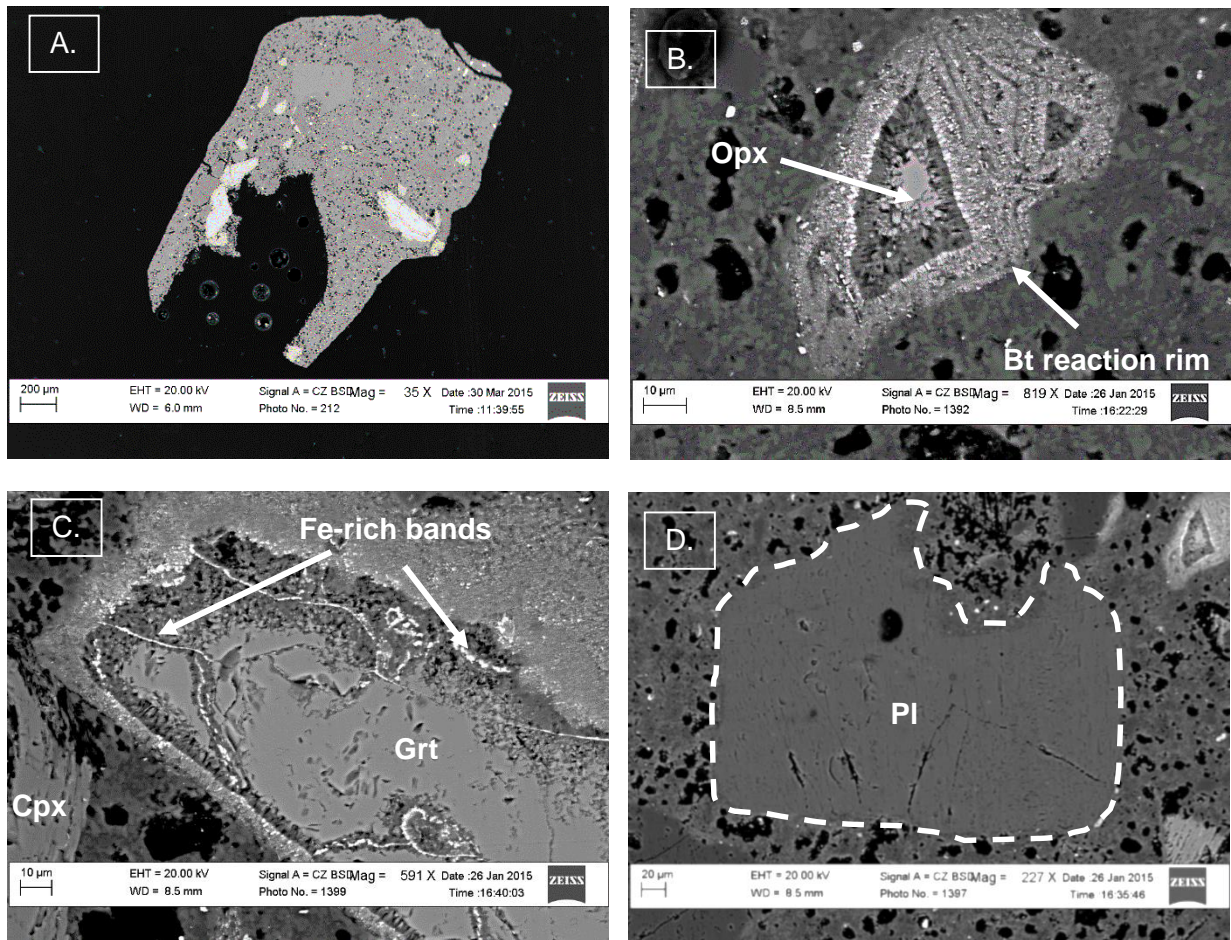


Figure 12 - BSE SEM Images Experiment 3 (1.90kbar; 723°C)

Image A: Overview image of the entire run product. From this image it clear to see that compared to the previous two experiments there is a significantly higher proportion of vesicles. This, along with the high quantity of plagioclase crystals within the melt, can be attributed to the temperature of the experiment lying on the H<sub>2</sub>O-melt saturation boundary (as predicted by phase equilibrium modelling). Images B and C: garnet and orthopyroxene have reacted with the surrounding melt portion to form biotite. Image D shows a subhedral plagioclase grain exhibiting exsolution textures.

## Experiment 4 - 1.40kbar; 743°C

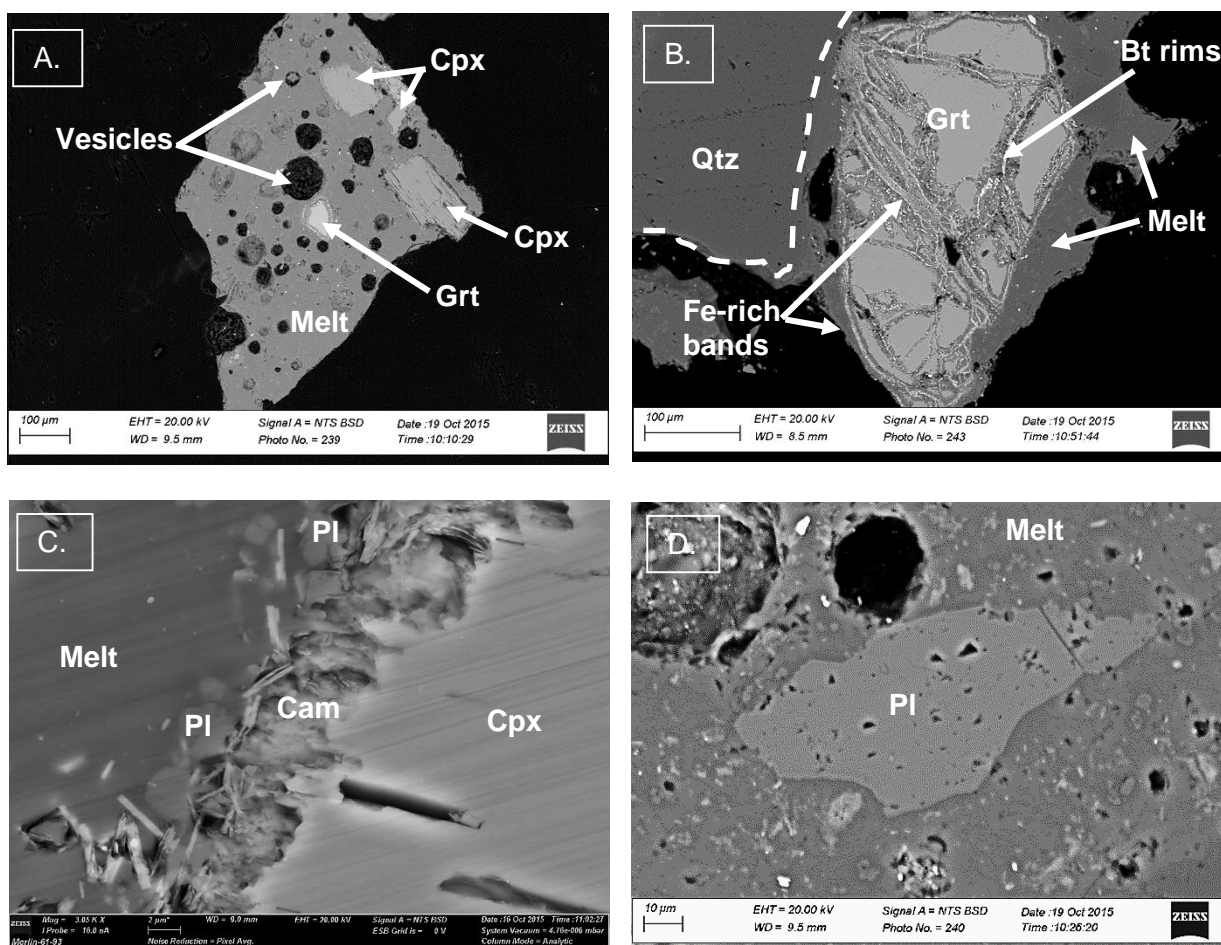


Figure 13 - BSE SEM Images Experiment 4 (1.40kbar; 743°C)

Image A: Overview of experimental run product. Large number of vesicles containing quenched crystals visible due to experimental conditions lying within the H<sub>2</sub>O-melt saturation band. Image B: extensive fracturing of garnet seed resulting in thick (~10µm wide) biotite rims containing Fe-rich bands along fracture planes. Image C: a zoomed in view of the reaction of clinopyroxene to clin amphibole along the mineral-melt reaction interface. Image D: large (~80µm), anhedronal plagioclase crystal containing triangular shaped etch pits. The plagioclase crystal is surrounded by a crystal rich melt that predominantly contains anhedronal plagioclase crystals (<1µm). Vesicles containing hydrous quench crystals, as well as vesicles/voids containing N<sub>2(g)</sub> are present.

## CHAPTER 5: RESULTS

## Experiment 5 - 1.40kbar; 730°C

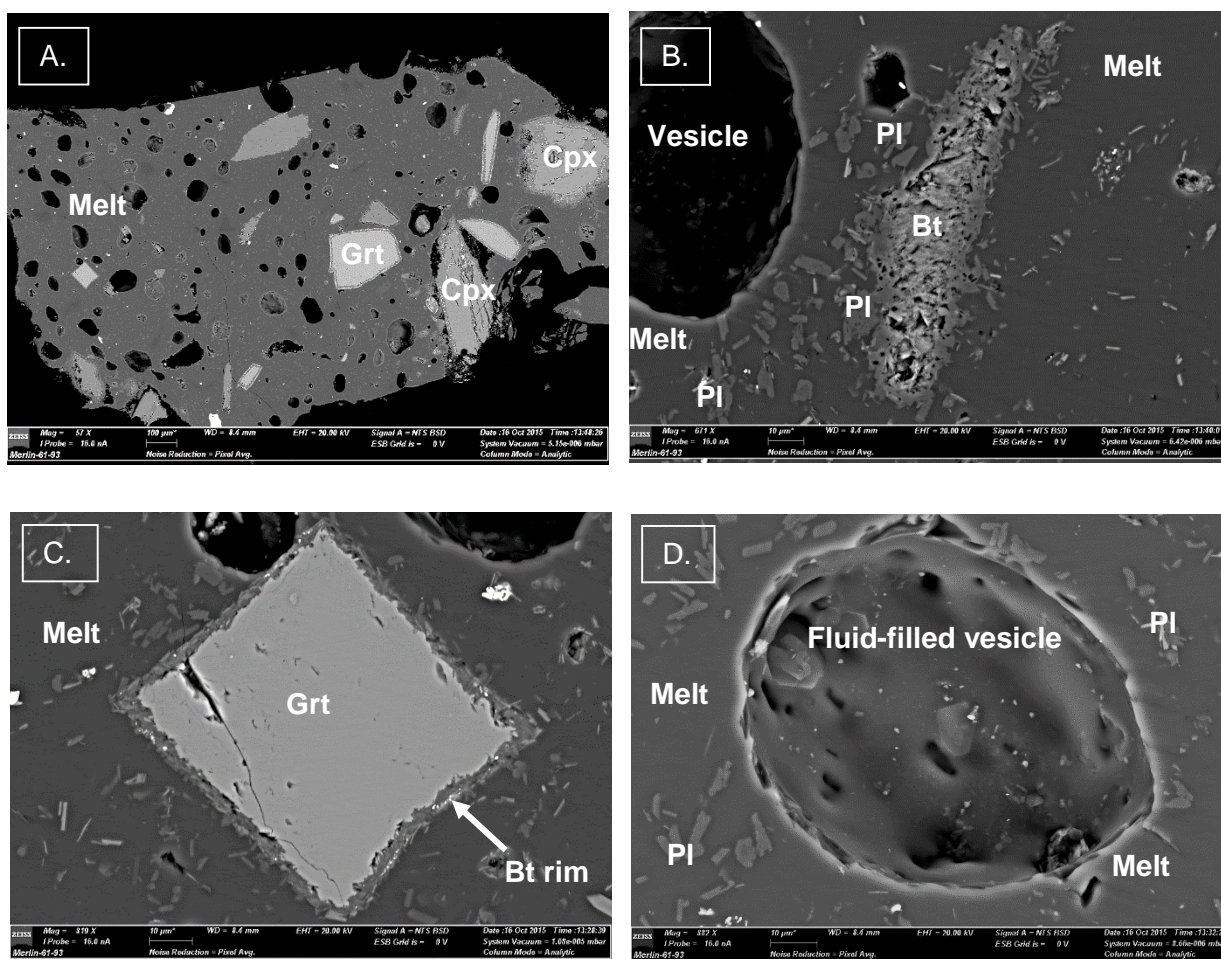


Figure 14 - BSE SEM Images Experiment 5 (1.40kbar; 730°C)

**A:** Overview of experimental run product. Vesicles are more prevalent, but smaller in size than higher T experiments at corresponding pressures (1.40kbar). **Image B:** pseudomorphic replacement of orthopyroxene by irregularly shaped, interlocking biotite crystals. Melt is homogeneous in composition and interspersed with small plagioclase crystals (<5µm length). **Image C:** garnet crystal orientated in such a way as to display one of the characteristic face shapes of a rhombic dodecahedron. The garnet has partially reacted with the melt to produce a thin, uniform biotite reaction rim. **Image D:** a close up view of a fluid-filled vesicle containing minimal quenched crystals.

### 5.3 Mineral and Textural Descriptions

The following section provides the reader with a detailed description of the experimental mineral compositions and textures. The five experiments have been first divided according to the pressure conditions at which they were run. Thereafter, each mineral description has been further subdivided according to the temperature conditions of its relevant experiment.

#### Higher Pressure Experiments (1.90kbar)

##### *Plagioclase*

**763°C:** The plagioclase crystals can be found along the edge of the run product. Their grain shape is indistinguishable, creating the appearance of a homogeneous, thin line running along the majority of the capsule. It also is present as minute, anhedral fragments that are scattered within the melt. These mineral fragments are generally  $<5\mu\text{m}$ . A few grains exist that are around  $10\mu\text{m}$  in length, and upon closer examination these crystals appear to show exsolution textures. Geochemical analysis indicates the composition of the plagioclase within the experiment to be  $\text{An}_{52.4}\text{Ab}_{43.0}\text{Or}_{4.6}$ , which differs dramatically from the initial plagioclase composition used in the starting powder. The initial plagioclase composition used in the starting powder have a definite albitic composition, with a mole percentage of  $\text{Ab}_{64}$ . This large discrepancy in composition may be a result of rapid dissolution-precipitation mechanisms that are responsible for the equilibration of plagioclase to the surrounding experimental pressure and temperature conditions. The experimental plagioclase can be described as having an intermediate composition lying between labradorite ( $\text{An}_{60}$ ) and andesine ( $\text{An}_{40}$ ) in the plagioclase series.

**733°C:** Plagioclase crystals are of particular interest in this experiment as they appear as two distinct textural varieties. The first type appears as small, euhedral crystals ( $<5\mu\text{m}$ ) that form a 'dense' ring around the entire run product (i.e. inner surface of gold capsule). These particular crystals overlap and interlock with each other, appearing very tightly packed. Equally small ilmenite fragments are present in amongst these plagioclase grains. The second textural variety of plagioclase crystals are significantly larger ( $\sim 30\mu\text{m}$ ) than those appearing on the inner surface of the gold capsule. These larger crystals tend to be isolated with regards to other minerals, and are instead completely surrounded by melt. They are also partially corroded, containing dark, circular spots of gas or melt inclusions. Both textural varieties are compositionally similar within minimal variation in apfu value, with the maximum deviation being  $\pm 0.08$  apfu for Na. All of the plagioclase within the experiment appears to have an albitic composition, with a general mole percent formula of  $\text{Ab}_{60.9}\text{An}_{36.3}\text{Or}_{2.8}$ .

**723°C:** The plagioclase within Experiment 3 (1.90kabr and 723°C) is albitic in composition, specifically  $Ab_{62.3}An_{35.1}Or_{2.6}$  (mol. %). When comparing the general plagioclase formula to the original plagioclase composition in the starting powder there is minimal variation in composition (maximum deviation 0.02 apfu). There is a large, anhedral plagioclase grain of approximately 200µm within the experimental run product (Figure 12 (D), pg. 64). This larger grain is isolated from the other minerals, and is instead surrounded by melt. The experimental melt is interspersed with very small plagioclase grains that are anhedral and less than 10µm in size.

### ***Garnet***

**763°C:** Although not predicted at the pressure-temperature conditions of Experiment 2 (1.90kbar and 763°C), garnet is present within the run product. There is only one garnet crystal visible within the run product. The grain is a subhedral lath, and it is considerably smaller than the majority of other minerals (30µm in length). The garnet grain is surrounded by melt with a relatively high concentration of plagioclase fragments. The garnet is in close proximity to a clinopyroxene crystal. The garnet is surrounded by a uniform reaction front (~5µm). This reaction front is comprised largely of indistinct biotite crystals.

The composition of the garnet is important as it may provide clues as to why garnet persists at the low pressure conditions of experimentation. By looking at its mole percent formula it is clear to see that the garnet ( $Alm_{58.7}Prp_{31.6}Grs_{9.6}Sps_{0.0}$ ) is compositionally similar to the original garnet composition in the starting powder ( $Alm_{67.4}Prp_{24.1}Grs_{7.4}Sps_{1.1}$ ). However, the Mg# of this experimental garnet is 34.99, which is higher than the 26.28 of the initial garnet composition in the starting powder.

**733°C:** Not evident within the run product.

**723°C:** Although not predicted for the pressure-temperature conditions of Experiment 3 (1.90 kbar and 723°C) garnet persists at these conditions. The garnet is in disequilibrium with the pressure, temperature and compositional conditions of the experiment, which is evident from the reaction rim surrounding all the garnet grains. The garnet within this experiment has a mol. % formula of  $Alm_{55.8}Prp_{31.4}Grs_{11.8}Sps_{1.0}$ . This garnet varies only slightly from the original garnet composition in the starting powder, which has a mol. % formula of  $Alm_{67.3}Prp_{24.1}Grs_{7.4}Sps_{1.2}$ . Examination of the mol. % formula shows there is a significant mol. % difference between the initial garnet composition and the experimental garnet in respects to almandine ( $\pm 11.5\%$ ).

The garnet grains within the run product appear tabular shaped, and are largely surrounded by the melt portion of the run product and a large number of vesicles. The largest garnet is

around 220µm in length (Figure 12 (C), pg. 64). It has a large reaction rim that extends mainly across one of its surfaces. This reaction rim has a biotite-like composition, and contains smaller reaction rims that run parallel to the grain boundary that appear to have a high Mn content. The smaller reaction rims vary significantly in length (<10 - 40µm). The exact composition of these small reaction rims is unknown as they are too narrow to get an accurate analysis, particularly when surrounded by the indistinct biotite-like material.

### ***Orthopyroxene***

**763°C:** Orthopyroxene is present in vast quantities, and along with its clinopyroxene counterpart forms the coarsest-grained minerals within the run product. The orthopyroxene crystals are around 250µm long. They appear as large, tabular crystals. Spatially the grains appear isolated from other minerals, and are surrounded solely by vesicle-rich melt.

The mole percent formula for the orthopyroxene in Experiment 2 is  $Wo_{1.8}En_{78.7}Fs_{19.5}$ . Although wollastonite is not a pyroxene mineral, due to its formula ( $CaSiO_3$ ) it has been used to illustrate a theoretical calcium endmember. The initial orthopyroxene compositions have a Mg# of 65.3, whilst the experimental orthopyroxene has a significantly higher Mg# at 78.5.

**733°C:** Not evident within the run product.

**723°C:** The orthopyroxene within Experiment 3 has a mol. % formula of  $Wo_{0.6}En_{65.5}Fs_{33.9}$ . The formula is mid-way between the enstatite-ferrosilite mineral series, and thus the mineral can be classified as hypersthene. The orthopyroxene in the run product differs from the initial peritectic orthopyroxene very minimally, with a Mg# number of 65.7 compared to the original orthopyroxene's 65.3. The orthopyroxene can be observed to be reacting, with the reaction being preserved in the run product as can be seen in the SEM images (Figure 12 (B), pg. 64). The reaction taking place between the orthopyroxene and melt is producing a rim of biotite-like material.

The orthopyroxenes are found across the run product, and are significantly smaller in size than the other minerals present within the experiment (approximately 10 µm diameter). Their size is due to the fact that they have almost fully reacted with the surrounding melt to produce a biotite-like material. The biotite rims are very intricate and fine-grained. Their composition as determined by SEM analysis was inaccurate as the surface of the reaction rim is not smooth, as well as the fact that the grains are too small to get an accurate and precise reading.

### ***Clinopyroxene***

**763°C:** The clinopyroxene crystals present within the experiment are sub- to euhedral in shape. The crystals appear to be surrounded entirely by melt and intergrain boundaries are



## CHAPTER 5: RESULTS

visible between some of the clinopyroxene and ilmenite crystals. The grains are variable in size ranging from 40µm to 200µm. The clinopyroxene crystals appear to be clustered, with the larger crystals being centrally located within the capsule. The smaller variety of clinopyroxene appear as anhedral fragments close to the edge of the capsule, and like their larger counterparts show no preferred orientation. No zonation within any of the crystals is evident either visually or through quantitative analysis.

Its mole percent formula indicates  $\text{Aeg}_{1.5}\text{Jd}_{0.9}\text{Di}_{97.6}$ . There are only slight differences between the original peritectic clinopyroxene, with the experimental clinopyroxene having a higher Mg# of 81.8 compared to the original clinopyroxenes' 80.5. The greatest deviation in apfu relates to the  $\text{Fe}^{2+}$  content which varies by 0.16 apfu. The Ca apfu value is 0.1 higher in the peritectic clinopyroxene than in the experimental equivalent.

**733°C:** Clinopyroxene exists as a stable phase within Experiment 1 (1.90kbar and 733°C). The crystals appear randomly distributed, and are well dispersed across the entire run product. The crystals vary dramatically in size, ranging from ~20 to 100µm. Despite their size all of the experimental clinopyroxenes show evidence of reaction rims of clinoamphibole. Some of the larger grains (~ 100µm) exhibit one directional cleavage. The smaller grains exhibit the most extensive amount of new mineral growth. This new growth was determined through SEM analysis to be similar in composition to the original clinopyroxene compositions. However, some variation between the two is clearly evident. Visually the original clinopyroxene composition (core) appears to be dark grey, whilst the new growth (rim) appears significantly lighter in colour, which infers a higher Fe content. The most notable compositional variation between the two is the Mg content of the rim (0.65 apfu) when compared to the core (0.86 apfu). Another interesting discrepancy between the two compositions relates to the Fe content. The Cpx rim, unlike the core, contains  $\text{Fe}^{3+}$  and, on average, shows an increase of 0.12 apfu for  $\text{Fe}^{2+}$ . ( $\text{Fe}^{3+}$  content has been estimated using Droop (1987)). The mineral formula calculated for the clinopyroxene cores indicates that it is a diopside, with the mole percent formula of  $\text{Aeg}_{0.0}\text{Jd}_{0.5}\text{Di}_{99.5}$  and a Mg# of 83.1. Whilst the mineral nature of the clinopyroxene rim changes slightly with a decreased Mg# of 66.18, and a composition of  $\text{Jd}_{5.7}\text{Di}_{94.3}$ .

**723°C:** The clinopyroxene within the experimental run product has a composition of  $\text{Jd}_{7.4}\text{Di}_{92.6}$ . The grains appear to be lath-shaped, and show strong one directional cleavage. The clinopyroxene appears to be reacting to form fine, needles of clinoamphibole along its crystal edge. The clinopyroxenes vary in size from around 50 to 60µm. They appear to be generally surrounded by melt, but also share mineral boundaries with rounded quartz crystals and garnet reaction rims (biotite-like material).

### ***Ilmenite***

**763°C:** The ilmenite crystals range in size from 10 – 100µm, and are typically subhedral in character. They are randomly dispersed in clusters, and are surrounded by melt. Occasionally the crystals share mineral boundaries with clinopyroxene grains. Only a few ilmenite crystals are visible within the run product.

The ilmenite in the run product has a general formula of  $(\text{Fe}^{2+}_{0.8} \text{Fe}^{3+}_{0.2} \text{Mn}_{0.1})\text{Ti}_{0.9}\text{O}_3$ , which when compared to the original ilmenite composition has a greater number of  $\text{Fe}^{3+}$  atoms per formula unit (+0.1 apfu). The minor inclusion of Mn into the mineral structure places the mineral composition towards the ilmenite end of the ilmenite ( $\text{FeTiO}_3$ ) – pyrophanite ( $\text{MnTiO}_3$ ) series. Despite all these aforementioned differences the Ti component of the minerals remains unchanged. The Mg# for the experimental ilmenite is higher at 1.92, when compared to the 0.96 Mg# of the initial ilmenite composition.

**733°C:** Within the run product the ilmenite crystals appear to be anhedral. Their size varies from 10 -35µm, and they appear evenly distributed along the outskirts of the run product. Visual examination of the ilmenite crystals would indicate little or no change textural change from the original composition within the starting material. However, quantitative analysis illustrates quite significant increases within the  $\text{Fe}^{3+}$ , Mn and Mg contents of the final run product when compared to the starting composition. The  $\text{Fe}^{3+}$  content increased from 0.09 to 2.1 apfu, whilst the Mn and Mg contents increase by 0.08 and 0.09 apfu respectively. The overall general mineral formula is  $(\text{Fe}^{2+}_{0.9}\text{Fe}^{3+}_{0.1} \text{Mn}_{0.1} \text{Mg}_{0.1})\text{Ti}_{0.9}\text{O}_3$ . The Mg# increases at this lower temperature of this experiment, moving from the 1.92 seen at 763°C to 5.00.

**723°C:** Not evident within the run product.

### ***Quartz***

**763°C:** Quartz is present in large quantities within the run product. It occurs in two areas in particular (Figure 11 (A and B), pg. 62). The boundary of the smaller (40 µm) crystal is indistinct and Fe rich areas exist in and around the crystal. The larger quartz crystal of 100µm is surrounded by melt. The presence of quartz in the run product implies that the starting bulk composition is oversaturated with respects to silica allowing for quartz (a mineral not part of the initial mineral assemblage) to be readily produced.

**733°C:** Quartz is visible in one area of the run product, in which it appears as a large (40µm) rounded crystal within the melt portion of the run product. It is easily distinguishable from the melt due to the variation in its colour (darker) when compared to the melt portion.

**723°C:** The quartz crystals are large (~30 - 100µm) and are well distributed across the entire run product. Mineral grain boundaries exist between the quartz crystals and a variety of minerals, such as orthopyroxene, clinopyroxene and garnet.

### ***Biotite***

Biotite appears to be present across all three of the higher pressure experimental run products. It appears as two textural varieties, firstly as a component within the reaction rims of metastable orthopyroxene and garnet, and secondly as a pseudomorph of these minerals. However, the biotite crystals in both cases were too small/narrow to analyse without contamination of the adjacent crystals and/or quenched melt. Consequently, compositional data of biotite has been excluded as a phase within the 'Mineral and Melt Compositions' section, as well as from the textural description that follows. Although the excitation volume of the electron beam was too large to analyse the biotite compositions accurately, it still allowed for the identification of the mineral phase within the run products.

**763°C:** The biotite within Experiment 2 occurs as a result of a metastable garnet phase reacting with the surrounding melt portion. It forms a reaction rim in which the individual crystals are so small in size that they are indistinguishable from one another. Certain areas within the reaction rim appear to be more Fe<sup>2+</sup> rich with the variation being as extreme as 1.0 apfu. However, due to their small crystal size, analysis of the mineral's composition was inaccurate due to contamination of the results by surrounding crystals and quenched melt.

**733°C:** The biotite within the experiment appears as fine, needle like crystals and is nucleated within one area of the capsule. The needle-like crystals are contained within a large lath shaped cavity and an adjacent, smaller, oval cavity. The cavities are surrounded by small, euhedral plagioclase crystals. The uneven surface created by the needle structures within the cavity has meant that quantitative analysis of the biotite was inaccurate.

**723°C:** In Experiment 3 biotite occurs as a reaction rim surrounding both reacting garnet and orthopyroxene minerals. In both cases the crystal size is less than 2µm, making analysis both difficult and largely inaccurate due to surrounding minerals and quenched melt contaminating the results. Spatially, the biotite is surrounded by melt and occurs near to both quartz and clinopyroxene crystals. In some areas of the run product biotite is present as small plates, showing preferred orientation, which have likely developed from the complete breakdown of orthopyroxene through mineral-melt reactions. The size of the reaction rim around the garnet and orthopyroxene grains may be indicative of which mineral reacts quicker with the surrounding melt portion. If this is the case, orthopyroxene reacts much faster than garnet at the pressure-temperature conditions of experimentation.

### ***Clinoamphibole***

In a similar manner to the biotite analysis the clinoamphibole needles were too small/narrow to accurately constrain their composition using SEM techniques. This accounts for the lack of compositional data in both the 'Mineral Composition' tables and the textural descriptions below.

**763°C:** Not evident within the run product.

**733°C:** Not evident within the run product.

**723°C:** Clinoamphibole appears along the edge of the clinopyroxene prisms within this experiment. Clinopyroxene appears to have reacted with the melt portion to produce thin (~1µm width), needle-like crystals of clinoamphibole. These crystals appear to show preferred orientation, particularly closer to the clinopyroxene crystal boundary. The alignment of these crystals appears to mimic the cleavage planes of the reacting clinopyroxene crystals.

### ***Melt***

**763°C:** The melt appears relatively homogeneous, with large quantities of vapour bubbles existing within it. Due to the large number of vesicles within this higher temperature run product the vapour bubbles are likely comprised two different gases. The first are nitrogen bubbles, which results from air being trapped within the gold capsule during preparation. This trapped nitrogen is an unavoidable consequence of the experimental procedure. The second variety is trapped aqueous fluid. This experimental melt contained the highest SiO<sub>2</sub> contents (79.35 wt. %) within the higher pressure experiments (1.90kbar). The melt also had a relatively low Na<sub>2</sub>O/CaO ratio (2.94) compared to the original starting melt's 3.56. Vesicles are randomly distributed across the run product, with some containing euhedral, quench crystals.

**733°C:** The melt appears homogeneous, which has been verified through quantitative analysis (maximum  $\sigma = 1.05$ ). The melt also contains a small number of dark, voids which most probably indicates the presence of insoluble N<sub>2(g)</sub> within the melt. The experimental melt compositions do not vary significantly over the temperature bracket of 40°C. However, there are marginal differences. The 733°C experiment contains the highest wt. % K<sub>2</sub>O (5.04), highest wt. % Na<sub>2</sub>O (2.86) and highest wt. % Al<sub>2</sub>O<sub>3</sub> (13.64). This may be largely due to the low proportion of plagioclase and biotite minerals in the run product. This mid-temperature experiment also has the lowest wt. % CaO, which can be ascribed to the fact that there is large proportion of clinopyroxene mineral in relation to the other minerals.

**723°C:** The temperature of experimentation lies within the H<sub>2</sub>O-melt saturation band, which accounts for the matrix being made up of plagioclase crystals and interstitial melt within the

run product. The angular nature of the smaller, interstitial melt pools results from the development of plagioclase crystal faces. The large amount of biotite within the experiment may also be a limiting factor accounting for the lower FeO content within the melt portion (0.57 wt. % compared to the 0.67 wt. % in higher temperature experiments) and the lower K<sub>2</sub>O wt. % of 4.10. This low temperature experiment contains the highest CaO value at 0.93 wt. %.

### **Lower Pressure Experiments (1.40kbar)**

#### ***Plagioclase***

**743°C:** Plagioclase crystals within the experiments appear in three major textural varieties. The first variety are present as fine, anhedral crystals that are both abundant and evenly distributed throughout the melt. These crystals vary in both their size and shape, but are generally <5µm in length. These fragments were too small to accurately analyse without contamination of the results by surrounding crystals and quenched melt. The second variety appears to be recrystallized plagioclases. The length of these crystals ranges between 45-55µm. They are homogeneous, subhedral to anhedral crystals that appear to have trapped melt/fluid components during their crystallization. The final plagioclase textural type appear to be large (163µm x 164µm) crystals, which have formed from the fracturing of a larger 'peritectic' plagioclase crystal. These minerals show no compositional or textural evidence that would indicate they had reacted with the surrounding melt during experimentation. In general the plagioclase crystals in this experiment all showed similar compositions to the initial plagioclase compositions in the starting powder. The overall mole percent formula of the experimental plagioclases is An<sub>35.3</sub>Ab<sub>62.9</sub>Or<sub>1.8</sub>, compared to the initial plagioclases' composition of An<sub>34.4</sub>Ab<sub>63.9</sub>Or<sub>1.7</sub>.

**730°C:** The plagioclase crystals were randomly dispersed throughout the experimental run product. The crystals are small, with the largest crystal being <15µm in length that appears as a subhedral lath. The majority of the crystals appear as fragments that are less than <5µm in diameter. All the crystals had appear to be sub- to anhedral in shape. The general mole percent formula of the plagioclase in this mid-temperature experiment is An<sub>35.3</sub>Ab<sub>62.5</sub>Or<sub>2.2</sub>. The newly formed plagioclase is sodic in composition, and is therefore similar in composition to the initial plagioclase composition. The experimental plagioclase also has a negligibly lower overall albitic component (Ab<sub>62.5</sub>) than the 'peritectic' plagioclase composition (Ab<sub>63.9</sub>).

#### ***Garnet***

**743°C:** Unlike in higher pressure experiments the garnet crystals within this experiment appear to be nucleated within one portion of the run product (Figure 13 (B), pg. 65). The configuration and overall size of the garnet crystals suggests that they all formed from one

original garnet crystal that has been fractured. The garnet fragments vary in size and shape (sub- to anhedral). The fragments are linked by a biotite rim that runs between and around the fragments. The entire garnet – biotite ‘network’ is 403 $\mu$ m x 222 $\mu$ m in size. The garnets within this experiment appear to have a significantly higher almandine component of  $X_{\text{Alm}} = 0.66$ , when compared to those seen in the higher temperature experiments ( $X_{\text{Alm}}$  of 0.55 – 0.58). However, its composition appears similar to the initial garnet composition in the starting powder ( $X_{\text{Alm}} = 0.67$ ).

**730°C:** The garnets within this experiment appear as both subhedral and euhedral crystal shapes (some as perfect squares, (Figure 10Figure 14 (C), pg. 66). There are only a few garnet crystals present and they are randomly dispersed throughout the run product and are surrounded by melt. Despite their shape the garnets all appear to have a thin (approximately 2 - 3 $\mu$ m), even rim of non-ideal biotite along their crystal faces. Quantitative examination of the garnets show them to have a mole percent formula of  $\text{Alm}_{59.5}\text{Prp}_{28.0}\text{Grs}_{11.6}\text{SpS}_{0.9}$ . This composition has a higher pyrope, grossular and spessartine component than the original garnet composition in the starting powder ( $\text{Alm}_{67.4}\text{Prp}_{24.1}\text{Grs}_{7.3}\text{SpS}_{1.2}$ ).

### *Orthopyroxene*

**743°C:** None evident within the run product.

**730°C:** None evident within the run product.

### *Clinopyroxene*

**743°C:** The clinopyroxene within this experiment exists in two compositional varieties. The most noticeable differences between the two types is within the apfu values for Ca, Mg and  $\text{Fe}^{2+}$ . The clinopyroxenes with the lower  $\text{Fe}^{2+}$  and Mg apfu values are associated with the precipitation of fine, needles of clinoamphibole along their rim. The clinoamphibole rims are non-uniform, with some crystals only showing evidence of clinoamphibole formation along one crystal edge. The formation of clinoamphibole is also associated with the development of euhedral plagioclase crystals that are ~2 $\mu$ m wide. Despite the differences both clinopyroxene minerals are classified as diopsides. Texturally both sets of minerals are large (106 $\mu$ m x 74 $\mu$ m), crystal laths that display one directional cleavage along their surfaces.

**730°C:** The clinopyroxene, like the higher temperature experiment (743°C) at corresponding pressures, also has a rim of fine, intermingling clinoamphibole crystals that is approximately 5 $\mu$ m in width. The rim is not uniform in size. The clinopyroxene is anhedral, and appears homogeneous in composition both visually and through quantitative analysis. Its overall mole percent formula indicates that it is diopside, which is exactly the same variety as the initial clinopyroxene composition in the starting powder.

### ***Ilmenite***

**743°C:** Ilmenite is visible as small (<1µm), globular crystals. A small amount of Si is present in the analyses, which can be attributed to the contamination of the results by surrounding crystals/quenched melt. Both the texture and composition of the experimental ilmenites differs from the initial ilmenite composition in the starting powder. Compositionally the experimental ilmenite is seen to have a higher Mg# of 2.86, whilst the initial ilmenite compositions have an Mg# of 0.96. Texturally the experimental ilmenite is significantly smaller than those first introduced into the starting composition.

**730°C:** The ilmenite appears as anhedral crystals, with very few crystals visible within the run product. The crystals are approximately 5 – 10µm in diameter, and are mainly isolated within the melt. The mineral formula is almost ideal, differing from the original ilmenite composition by ±0.1 apfu Fe<sup>2+</sup>, Fe<sup>3+</sup> and Ti.

### ***Quartz***

**743°C:** The majority of the quartz appears to be nucleated into one large pool that exists in close proximity to the garnet-biotite network mentioned above, as well as melt and anhedral vesicles. The crystal is large (453µm x 194µm) and subhedral in nature. There are a few rounded quartz crystals that are smaller ~15µm x 15µm in size which are predominantly surrounded by melt.

**730°C:** Rounded crystals of quartz are present. Unlike in experiments at higher pressure (1.90kbar) the majority of the crystals appear elongated rather than circular in shape. The different morphologies observed within and between experiments is dependent on whether the crystal face being examined is the prismatic or pyramidal face of an alpha quartz prism. The quartz crystals are isolated from most of the more mafic mineral crystals, instead all are surrounded by plagioclase masses. The crystals range in diameter from 50 - 150µm.

### ***Biotite***

As mentioned in the biotite section within the higher pressure (1.90kbar) experiments the analysis of biotite within the experiments appears to be marred by its small crystal size. The fact that the analysis appeared to be inaccurate is likely due to issues with the electron beam within the SEM being too large to analyse the small crystals, rather than the analysis indicating the presence of biotite crystals with non-stoichiometric compositions.

**743°C:** Biotite forms reaction rims around the garnet minerals within the experiments. The biotite rim surrounding garnet is large, with a width of ~ 15.4µm at its widest point. Compositionally, the biotite rim around garnet appears to be Al-rich and Mg-poor. The

characteristic Fe-rich bands along the fracture planes of garnet crystals are also evident within this experiment.

**730°C:** Garnet has a reaction rim of biotite. The biotite in this experiment appears homogeneous, with the exception of fine Fe-rich bands that run parallel to the crystal boundary. In this experiment there are also isolated masses of biotite plates that show preferred orientation. These masses look subhedral in shape, with some masses appearing to be more tabular in shape than others. These are most likely pseudomorphic replacements of orthopyroxene by biotite within the experiment.

### ***Clinoamphibole***

Clinoamphibole was identified within both of the lower pressure experiments, but its analysis was inaccurate as the results contained components of surrounding minerals and quenched melt.

**743°C:** Clinoamphibole within this experiment appears similar to the clinoamphibole observed in Experiment 3 at higher pressure (1.90kbar). Fine, needle like crystals of clinoamphibole minerals appear to be the product of reactions between the clinopyroxene and melt (Figure 13 (C), pg. 65). This clinoamphibole reaction rim is surrounded by small (~2µm), euhedral plagioclase crystals. The presence of plagioclase is indicative of water being drawn out of the surrounding melt by mineral-melt reactions, which promotes crystallization.

**730°C:** The clinoamphibole surrounding the clinopyroxene appears as needle shaped crystals that show no preferred orientation, and instead form a mesh like structure. These crystals are <5µm in length and width. Unlike the biotite reaction rims around garnet the clinoamphibole reaction rim surrounding clinopyroxene is less well-defined.

### ***Melt***

**743°C:** The melt portion is homogeneous in both appearance and composition. As in the higher pressure experiments the melt is leucocratic in nature. The most significant difference between the melts of the higher and lower pressure experiments is the higher K<sub>2</sub>O/Na<sub>2</sub>O ratio of 2.29 compared to the 1.76 ratio seen in a similar temperature experiment (733°C) at 1.90kbar. The melt is vesicle-rich, containing vesicles as large as ~80µm in diameter. The vesicles are likely fluid (H<sub>2</sub>O) saturated, as some contain hydrous, quenched crystals.

**730°C:** The melt is both similar in composition and appearance to the 743°C experiment discussed above. However, slight variations in composition are evident. Overall the experimental melt has the lowest A/NK and A/CNK ratios out of all the experimental melts within this research at 1.52 and 1.41 respectively.



## Chapter 6: Discussion and Interpretation

### 6.1 Non-Equilibrium Studies

Examination of natural rock systems on a macroscopic scale can appear to show equilibrium features. However, analysis of these rocks on a microscopic level is likely to display evidence of grain-scale disequilibrium, such as coronas and reaction rims (Gill, 2015). The experimental findings of this research exhibit both equilibrium and disequilibrium features. The experimental run products provide a window into the degree of equilibration at various magmatic pressure and temperature conditions within an average I-type granite composition.

From the findings of this experimental research it is clear to see that the experimental minerals within the run products are both texturally and compositionally distinct from the initial 'peritectic' minerals added to the starting bulk composition. These mineralogical changes are evidence of the system moving in the direction of equilibrium, by attempting to reduce its Gibbs free energy (Giddings, 1991; Zhu and Anderson, 2002). The types of mineral reaction processes that are seen to be at work within the magma are largely dependent on the stability of the phases within the magma, as well as whether the individual 'peritectic' mineral phases are in equilibrium with the surrounding magma composition. Similarly, the pressure and temperature conditions of the surrounding magma is seen to control the types of reaction processes, and ultimately the manner in which equilibrium is approached within individual mineral phases.

Although the system appears to be moving in the direction of equilibrium, and can largely be considered 'equilibrium data' (Luth, 1976), there is evidence of localized disequilibrium features within the experimental run products. The presence of kinetically persistent experimental garnet well below the pressure and temperature conditions in which it is predicted to be stable by phase equilibrium modelling is a prominent disequilibrium feature within the experimental results. Although the garnet composition is seen to change, potentially through dissolution-precipitation mechanisms, and later reactions with the melt phase, it is clear from the low pressure and temperature conditions of experimentation that these garnets are preserved at near subsolidus conditions. The overriding implication of these findings is the potential preservation of these disequilibrium features within the crystalline granitic rocks (Carmichael et al., 1974). In the case of undifferentiated I-type granites, high pressure minerals, such as garnets, are uncommon features (Clemens et al., 2011). However, where garnets are present in granites they commonly appear to have reaction rims of biotite (e.g., Villaros et al., 2009a), as can also be seen in the experimental run products.

## CHAPTER 6: DISCUSSION AND INTERPRETATION

This research is a study into the 'fate' of a mineral assemblage that may reasonably represent an entrained 'peritectic' mineral assemblage within an I-type granitic magma. The research assumed instantaneous emplacement of the magma at different, relatively low magmatic temperatures (~720-770°C) and pressures (~2kbar). These pressure temperature conditions were then steadily maintained over the 10 day experimental run-time. These 'peritectic' phases generally appear to be out of equilibrium with the composition, pressure and temperature of the experimental magma. The subsections that follow examine the processes by which these non-equilibrium 'peritectic' mineral phases are observed to either approach or attain equilibrium within the experimental run products. Further discussions relating the predicted stabilities of minerals and equilibrium nature of the 'peritectic' minerals as determined by the phase equilibrium modelling are also outlined in the sections that follow.

## 6.2 Mineral Kinetic Processes

### 6.2.1 Dissolution-Precipitation Mechanism

#### *Plagioclase*

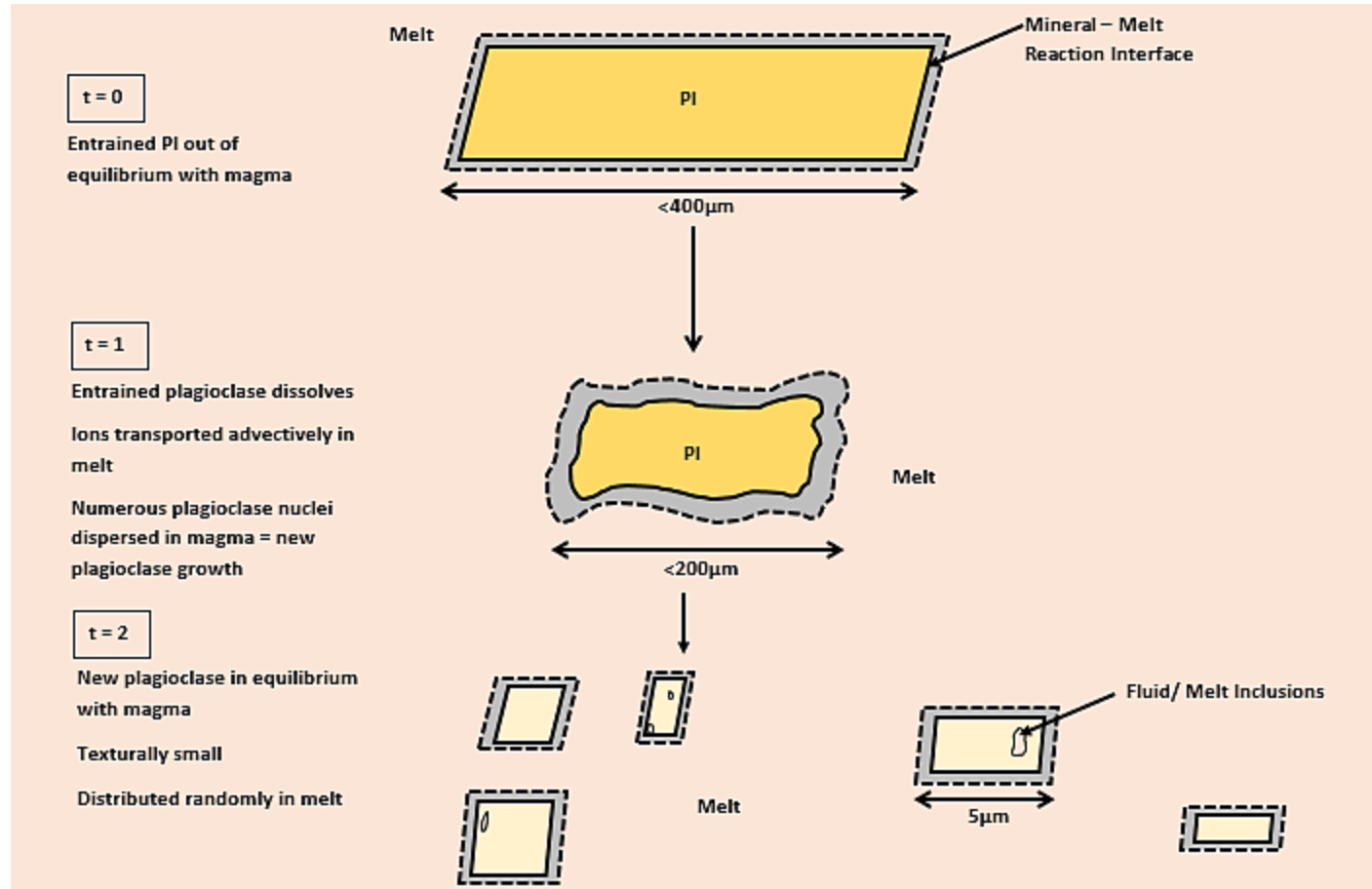
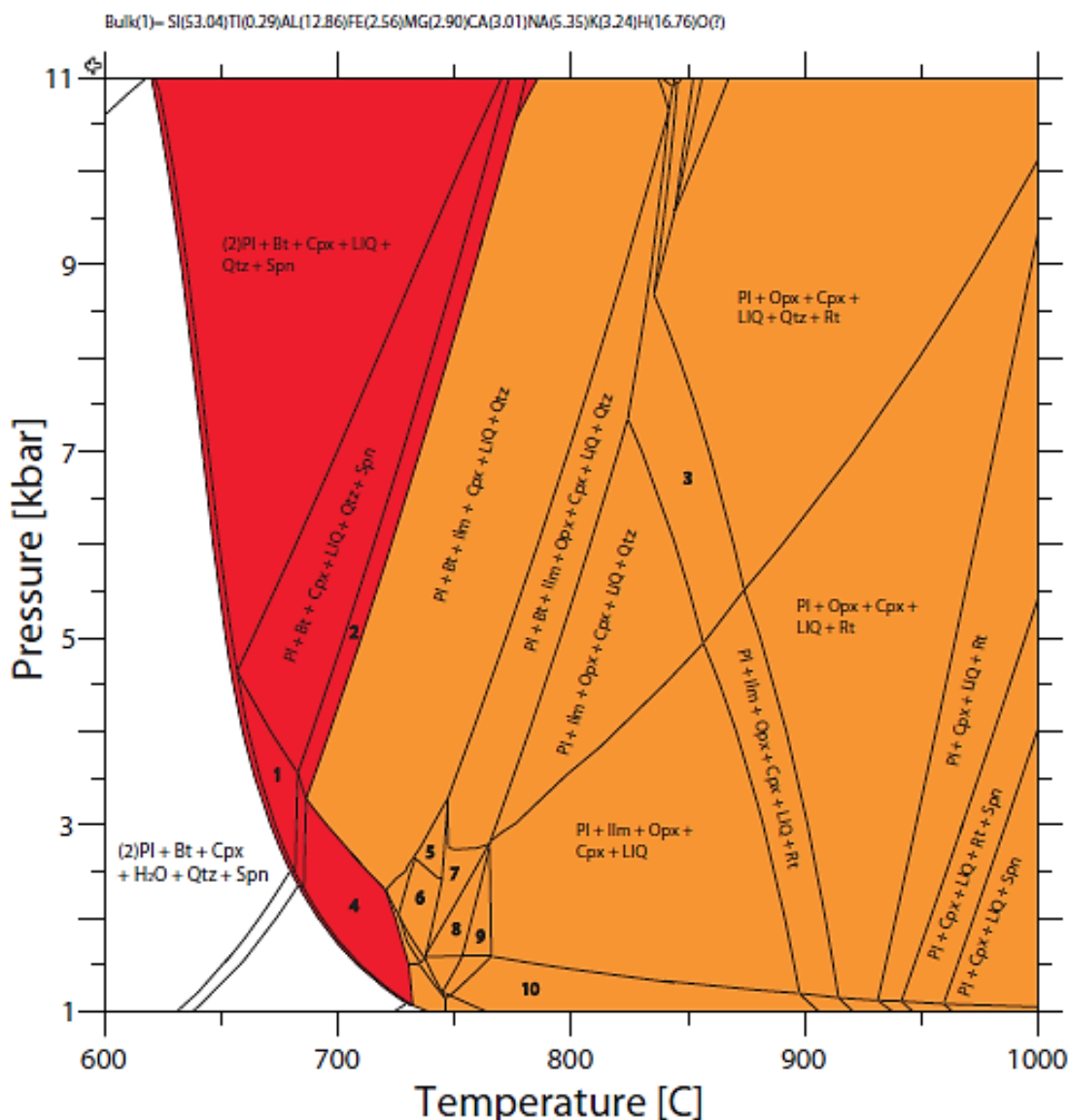


Figure 15 - Schematic of Dissolution - Precipitation Mechanism in Plagioclase



**Figure 16 - Plagioclase Hypersolidus Stability Fields for an Average I-type Granitic Magma Composition.** The orange shaded regions indicate where plagioclase is predicted to be stable by the phase equilibrium modelling, but is compositionally different to the initial 'peritectic' plagioclase seed placed within the experimental starting bulk composition. These PT regions correspond to where a coupled dissolution-precipitation mechanism is proposed to be the dominant reaction process responsible for the re-equilibration of plagioclase to the PT conditions of the surrounding magma in both natural and experimental systems. The red shaded areas show where the predicted and 'peritectic' plagioclase compositions used in the starting material are compositionally similar ( $\pm 2.0$  mol. % albite). Within these regions the plagioclase will not react, as it is in compositional equilibrium with the surrounding magma.

As predicted by phase equilibrium modelling, experimental plagioclase is evident and stable in all of the experimental run products. The experimental plagioclase crystals show evidence of textural and compositional equilibration with the surrounding magma within 10 days, and across all temperature and pressure conditions of experimentation. Due to the apparent fast-nature of the equilibration it is proposed that these features are a consequence of a rapid and efficient dissolution-precipitation mechanism as illustrated in Figure 15 (pg.80). Figure 16 (above) indicates the pressure and temperature regions in which the 'peritectic' plagioclase is

predicted to be stable, and either out of compositional equilibrium (orange shaded region) or in compositional equilibrium (red shaded region) with the surrounding I-type granitic magma composition.

Initially the 'peritectic' plagioclase compositions within the experimental bulk starting composition were metastable, but were out of compositional equilibrium with the surrounding magma. In an attempt to reduce the free energy of the system, and ultimately achieve equilibrium, the plagioclase crystals reacted spontaneously with the surrounding melt. As a result of their compositional disequilibrium within the magma, the 'peritectic' plagioclase crystals dissolved within the melt according to a coupled dissolution-precipitation mechanism. During the dissolution stages Na, Ca, Al, Si from the plagioclase crystals are transferred across a narrow, mineral-melt reaction interface into the surrounding melt. These liberated components from the 'peritectic' plagioclase crystals are mobilized via advection within the melt substrate. The transported components within the melt substrate bond with each other and components of the silicate melt to form nuclei upon which a new, equilibrium plagioclase phase can grow. These nuclei form within the melt at sites of compositional fluctuations or impurities (Vernon, 2004). In the experiments small plagioclase crystals (<2 $\mu$ m long) appear to have nucleated and grown along the reaction rims of biotite that surround the experimental garnets and orthopyroxenes. In this case, plagioclase growth can largely be ascribed to the depletion of H<sub>2</sub>O within the surrounding melt resulting from biotite growth at the expense of H<sub>2</sub>O. Previous experimental studies have indicated that for a wide variety of starting compositions (granites, granodiorites, dacites and rhyolites) the growth rate of plagioclase is on average between 10<sup>-7</sup> to 10<sup>-9</sup> cm/s depending on the temperature and pressure conditions (Agostini et al., 2013 and references therein).

Both textural and compositional evidence exists, which indicates that the initial 'peritectic' plagioclase has dissolved and re-precipitated with a composition better equilibrated with the experimental conditions. The most compelling textural evidence to support this hypothesis is the presence of primary melt inclusions along the edges of the newly formed plagioclase crystals, particularly in the higher pressure experiments (e.g., 1.90kbar, 733°C). These inclusions are proposed to be the result of: rapid growth of the plagioclase crystals, minor melt compositional changes, and the deposition of foreign particles along the crystal surface (Samson et al., 2003). Lower pressure experiments (1.40kbar) show plagioclase crystals with etch pits along their surfaces. These etch pits are proposed to be suitable to entrap free fluid phases on the surface of the crystals (Samson et al., 2003).

From a compositional perspective at each pressure and temperature condition of experimentation the experimental plagioclase appears homogeneous, exhibiting no chemical

or structural zonation. However, the experimental plagioclase varies in its composition dramatically between experiments with different temperature conditions. The most noteworthy compositional change is the increasingly sodic nature of the plagioclases with decreasing temperatures. The initial 'peritectic' plagioclase composition was  $X_{Ab} = 0.64$ , whilst at the highest temperature experiment (763°C; 1.90kbar) the albitic component of the newly precipitated plagioclases was considerably lower at 43.08 mol. %. This value increases at lower experimental temperatures, with the highest albite content (62.28 mol. %) at 723°C. It is significant to note that the lowest temperature plagioclases retained a similar composition to that of the initial 'peritectic' plagioclase crystals, with a difference of only  $\pm 1.68$  mol. %. The change in plagioclase composition across different pressure and temperature conditions of experimentation is evidence that the dissolution-precipitation mechanism brings the initial 'peritectic' plagioclase minerals into compositional equilibrium with the surrounding magma.

Newly formed plagioclase crystals in the higher temperature experiments (763-733°C; 1.90kbar) are small (<5 $\mu$ m length) and exhibit high levels of dispersion within the melt. The aforementioned may be ascribed to the low entropy of fusion of plagioclase when compared to the mafic minerals, such as garnet and pyroxene. Despite the fact that the plagioclase crystals appear spatially isolated from one another, their compositions remain homogeneous throughout the experiments. This geochemical homogeneity is probably due to the fact that the experimental melt in which the plagioclase is both dissolved and precipitated is similarly homogeneous in composition.

All the aforementioned compositional and textural features indicate that the experimental plagioclase has undergone highly efficient recycling to the lower temperature conditions of the surrounding melt, at pressure and temperature ranges appropriate to granitic magma emplacement in the upper crust. From the experimental findings, the mechanism of dissolution-precipitation is inferred to be rapid, occurring within the 10-day time frame of the experimental runs. Further discussions relating to the dissolution and growth rates of the experimental plagioclases are outlined in the 'Dissolution Rates' subsection (pg.86).

### ***Clinopyroxene***

In a similar manner to the 'peritectic' plagioclase, the 'peritectic' clinopyroxene added to the starting bulk composition is out of compositional equilibrium with the surrounding magma. Figure 17 (pg.85) illustrates the pressure and temperature conditions for which clinopyroxene is predicted to be stable within the I-type granitic magma, and where the 'peritectic' clinopyroxene differs in composition from the predicted clinopyroxene phase. It is proposed that across these pressure-temperature ranges the experimental clinopyroxenes have undergone a localized, coupled dissolution-precipitation mechanism that has allowed for the

precipitation of a new clinopyroxene phase along the 'peritectic' clinopyroxene surface. Textural and compositional evidence of this mechanism is observed in the form of simple compositional zonation, which can be seen in the mid-temperature, higher pressure experiment (733°C at 1.90kbar). In this experiment the clinopyroxene core is compositionally equivalent to the initial 'peritectic' clinopyroxene used in the starting powder. In contrast the clinopyroxene rim differs quite significantly with an  $X_{Di}$  of 0.94 and a  $X_{Jd}$  of 0.06. This zonation pattern is evidence of a localized, coupled dissolution-precipitation mechanism that has facilitated the partial equilibration of the 'peritectic' clinopyroxene crystal. Unlike the dissolution-precipitation mechanism responsible for plagioclase equilibration that involves mass transfer within the melt phase, new clinopyroxene growth occurs along the surface of the dissolving 'peritectic' clinopyroxene crystal. The growth of the new clinopyroxene phase is facilitated by the transfer of ions between the melt and 'peritectic' clinopyroxene across a nanoscale mineral-melt reaction interface (Ruiz-Agudo et al., 2014). Consequently, this reaction interface can have thermodynamic and physical properties; such as composition, viscosity and solute adsorption, that differ vastly from the bulk melt composition (Ruiz-Agudo et al., 2014). Precipitation along the 'peritectic' clinopyroxene crystal cores is triggered by the supersaturation of the new clinopyroxene phase within the reaction interface (Ruiz-Agudo et al., 2014).

Although Figure 17 (overleaf) suggests that clinopyroxene will undergo a dissolution-precipitation mechanism across all of the investigated pressures and temperatures, it is clear from the experimental findings that this is not always the case. At temperatures of 743°C and 730°C at 1.40kbar, and at 723°C at 1.90kbar the 'peritectic' clinopyroxene has a narrow reaction rim of clinoamphibole. It should be noted that, at the lower experimental pressure of 1.40kbar, clinoamphibole is predicted by the phase equilibrium modelling to be a stable phase. Interestingly, the composition of the 'peritectic' clinopyroxene remains unchanged within the 1.40kbar experiments, which indicates that a dissolution-precipitation mechanism is not at work within these minerals. The experiments in which a reaction rim of clinoamphibole is observed around the 'peritectic' clinopyroxene are the only experiments predicted by the modelling software to have an aqueous fluid phase. Further examination of these experimental run products seems to show vesicles that contain quench, hydrous crystals, which indicates agreement between the modelled and experimental findings. The reaction below illustrates a potential reaction between clinopyroxene and the melt portion to produce clinoamphibole.

*Diopside + Melt Components (Anorthite + Water)  $\rightleftharpoons$  Hornblende + Quartz + Ca-enriched melt*

## CHAPTER 6: DISCUSSION AND INTERPRETATION

The reaction rims of clinopyroxene around clinopyroxene are significantly narrower than the biotite reaction rims surrounding both orthopyroxene and garnet at corresponding pressure and temperature conditions. This suggests that the reaction involving clinopyroxene and melt is significantly slower than the reactions involving orthopyroxene and melt, and garnet and melt. This may be a consequence of the low anorthite component in the melt, compared to the K-feldspar component that is a major reactant in the formation of biotite.

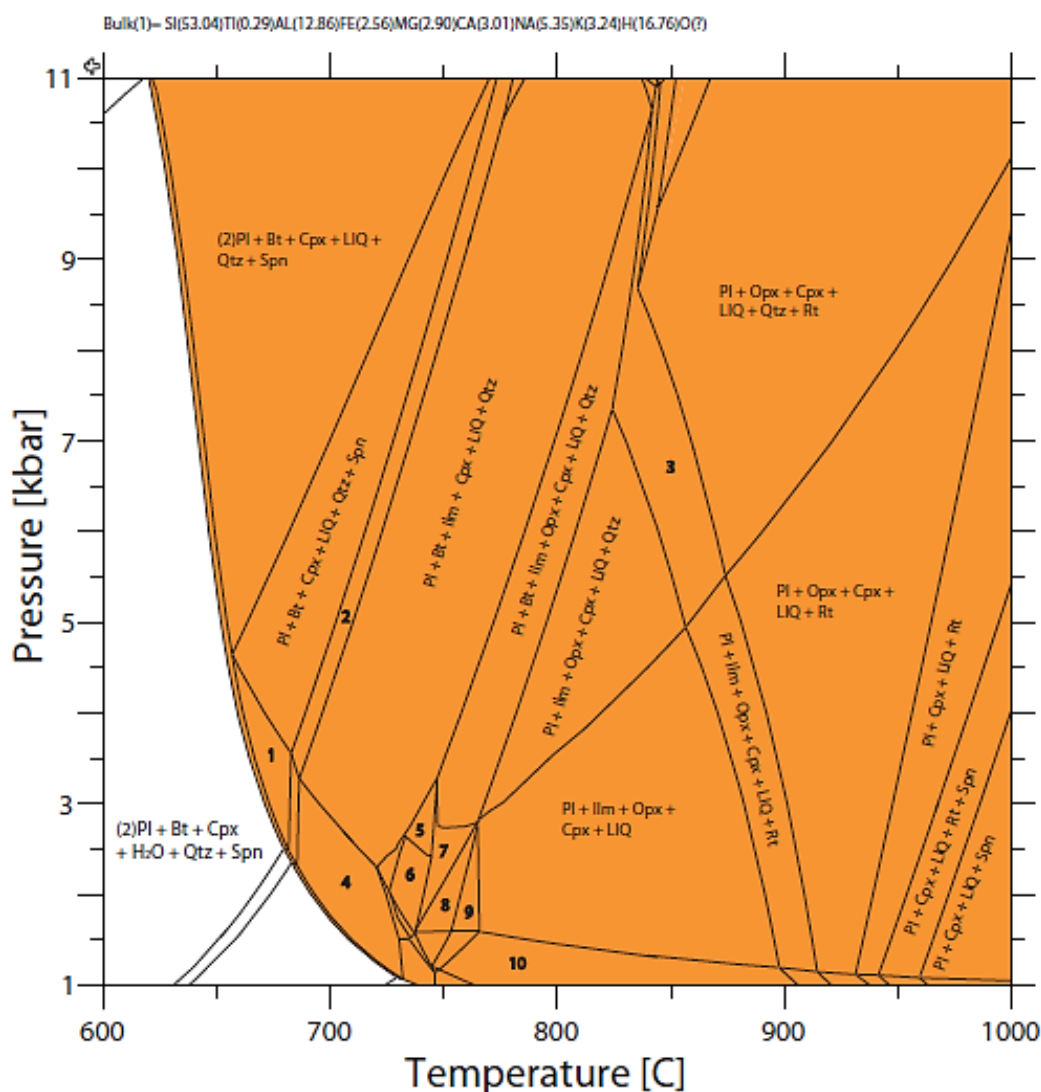


**Figure 17 - Clinopyroxene Hypersolidus Stability Fields for an Average I-type Granitic Magma Composition.** Clinopyroxene is predicted to be stable across the entire hypersolidus region (orange shaded regions). The composition of the 'peritectic' clinopyroxene mineral used within this research is out of compositional equilibrium with the surrounding magma across all hypersolidus conditions in which clinopyroxene is predicted to be a stable phase. The 'peritectic' clinopyroxene has a considerably higher diopside component (> 92 mol. %) compared to the predicted clinopyroxene composition, which in some cases is predicted to only contain 45 mol. % diopside. In a similar manner to 'peritectic' plagioclase, the 'peritectic' clinopyroxene is proposed to undergo a coupled dissolution—precipitation mechanism at the investigated pressures and temperatures of this research. However, low temperature, fluid saturated experiments appear to show clinopyroxene reacting with melt to produce a hydrous phase, i.e. clinopyroxene.



### ***Dissolution Rates***

In a multicomponent system the rate of reactions are regulated by the nucleation and growth of new, more thermodynamically stable phases (Koga, 1999). There are several factors that limit the growth of these stable phases, such as impeded ion transport through the melt substrate, or the potentially slow rate of atomic bonding at the surface of the newly precipitated phase (Koga, 1999). Previous experimental studies on the Sierra Nevada granites and granodiorites determined the equilibration rate of feldspars with granitic and granodioritic compositions exposed to similar pressure (2kbar) and temperature (725°C) conditions as this study, to be incredibly slow, requiring an experimental run time of 4 to 6 months to equilibrate fully (Piwinski, 1968).

Unlike the previous experimental study mentioned above, the localized equilibration of granitic components within the experiments conducted in this research is inferred to be rapid. The most noteworthy evidence of this is the equilibration of 'peritectic' plagioclase to the P-T-X conditions of the surrounding magma by an efficient, coupled, dissolution-precipitation mechanism. The dissolution and precipitation stages of this mechanism are controlled by different rate limiting factors. The dissolution stage of this mechanism is rate-controlled by the slowest diffusing components in the surrounding melt portion, typically Si (Lo Cascio et al., 2008) and Al in the case of plagioclase. Conversely, the rate of precipitation of new phases is controlled by the "fastest major diffusing component in a crystal" (Lo Cascio et al., 2008). The dissolution-precipitation mechanism is a simultaneous process (e.g., Putnis, 2002; Villaros et al., 2009). In fluid (H<sub>2</sub>O) -saturated experiments the dissolution of plagioclase is proposed to be more efficient as H<sub>2</sub>O is able to act as a carrier of relevant ions, such as Na<sup>+</sup> and Ca<sup>2+</sup>, or in the case of K-feldspar, K<sup>+</sup>. H<sub>2</sub>O also influences the degree to which feldspathic material is able to grow and develop within a magma. In the case of continuous decompression experiments a sufficiently high H<sub>2</sub>O content at initial pressure temperatures encourages crystal growth over nucleation (Arzilli and Carroll, 2013). Fluid (H<sub>2</sub>O) – saturated systems also favour dissolution-precipitation over solid-state diffusion processes (Putnis, 2009).

In this research the duration of each experiment was 10 days, and in that time the experimental plagioclase no longer texturally or compositionally resembled the higher pressure and temperature 'peritectic' plagioclases. It is therefore presumed that the dissolution-precipitation mechanism responsible for the formation of a new plagioclase composition occurs in under 10 days, particularly as no intermediary steps, such as mineral breakdown or zonation, are observed within the experimental plagioclases. As a 10-day experimental run time was maintained throughout the five experiments, the exact point in time at which plagioclase equilibrated with the melt could not be determined.

Figure 18 (below) illustrates a theoretical dissolution rate for plagioclase crystals of varying lengths. The first point on the plagioclase line represents the length of initial ‘peritectic’ plagioclase (0.04cm) which was a constituent of the bulk starting composition of the experiments. Previous experimental studies conducted at 1bar and 1kbar and  $>1000^{\circ}\text{C}$  indicate a minimum dissolution rate for plagioclase in the order of  $10^{-7}$  cm/s for basaltic melts (Agostini et al., 2013; Donaldson, 1985). There is a lack of dissolution data for plagioclase within granitic systems at appropriate pressure and temperature conditions that correspond with this research. However, experimental studies on various starting materials (granites, granodiorites, rhyolites and dacites) determined the plagioclase growth rate to also be in the order of  $10^{-7}$  cm/s at similar pressure and temperatures to this research (Agostini et al., 2013 and references therein). It is unlikely that the ‘peritectic’ plagioclase is able to dissolve entirely within the melt phase, therefore the rate limiting step appears to be the crystallization of the new plagioclase phase. Consequently,  $1 \times 10^{-7}$ cm/s was deemed an appropriate approximation for plagioclase dissolution within the experiments. This growth rate is linear, as opposed to volumetric. 4.62 days was calculated to be the length of time for dissolution to occur in plagioclase mineral of 0.04cm (length).

From the graph below it can be determined that a plagioclase crystal of size 1cm would take approximately 116 days to dissolve in an emplaced I-type magma ( $\sim 720\text{-}770^{\circ}\text{C}$ ; 2kbar).

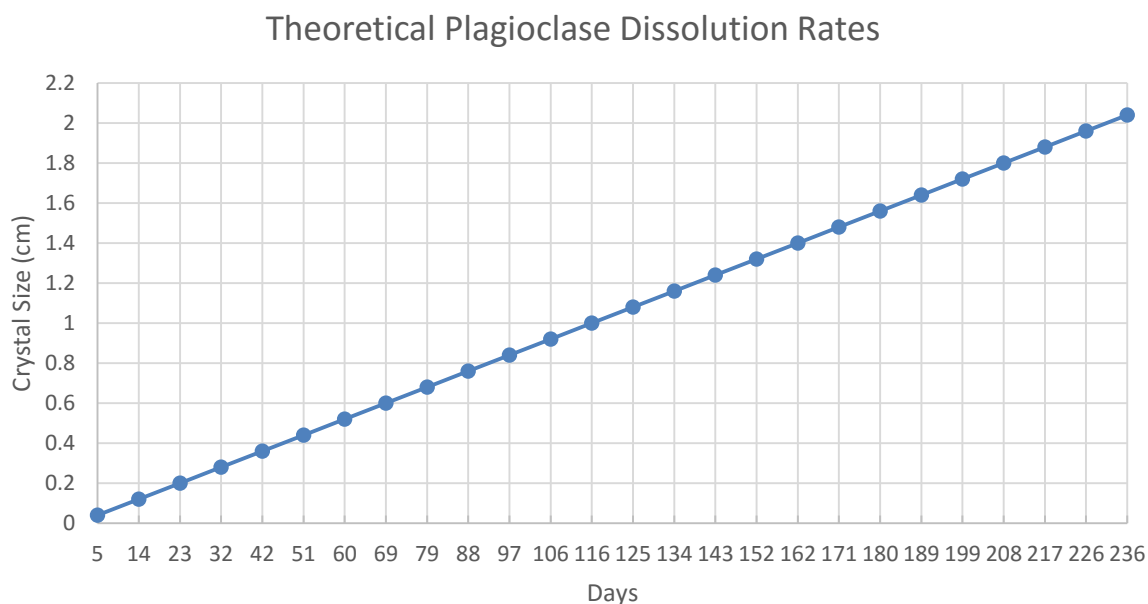


**Figure 18 - Theoretical Dissolution Rates for ‘Peritectic’ Plagioclase**

Calculations were also conducted to determine the minimum dissolution rate in g/hr for the initial ‘peritectic’ plagioclase materials over a time period of 10 days. This was calculated by determining the mass of plagioclase (g) that was placed within each experimental capsule.

These masses were then averaged ( $9.42 \times 10^{-4}$  g), and divided by the hypothetical dissolution time (4.62 days) for plagioclase in the experiments. The average minimum dissolution rate was determined to be  $8.49 \times 10^{-6}$  g/hr, assuming a constant dissolution rate.

## 6.2.2 Mineral-Melt Reactions

### Garnet - Biotite

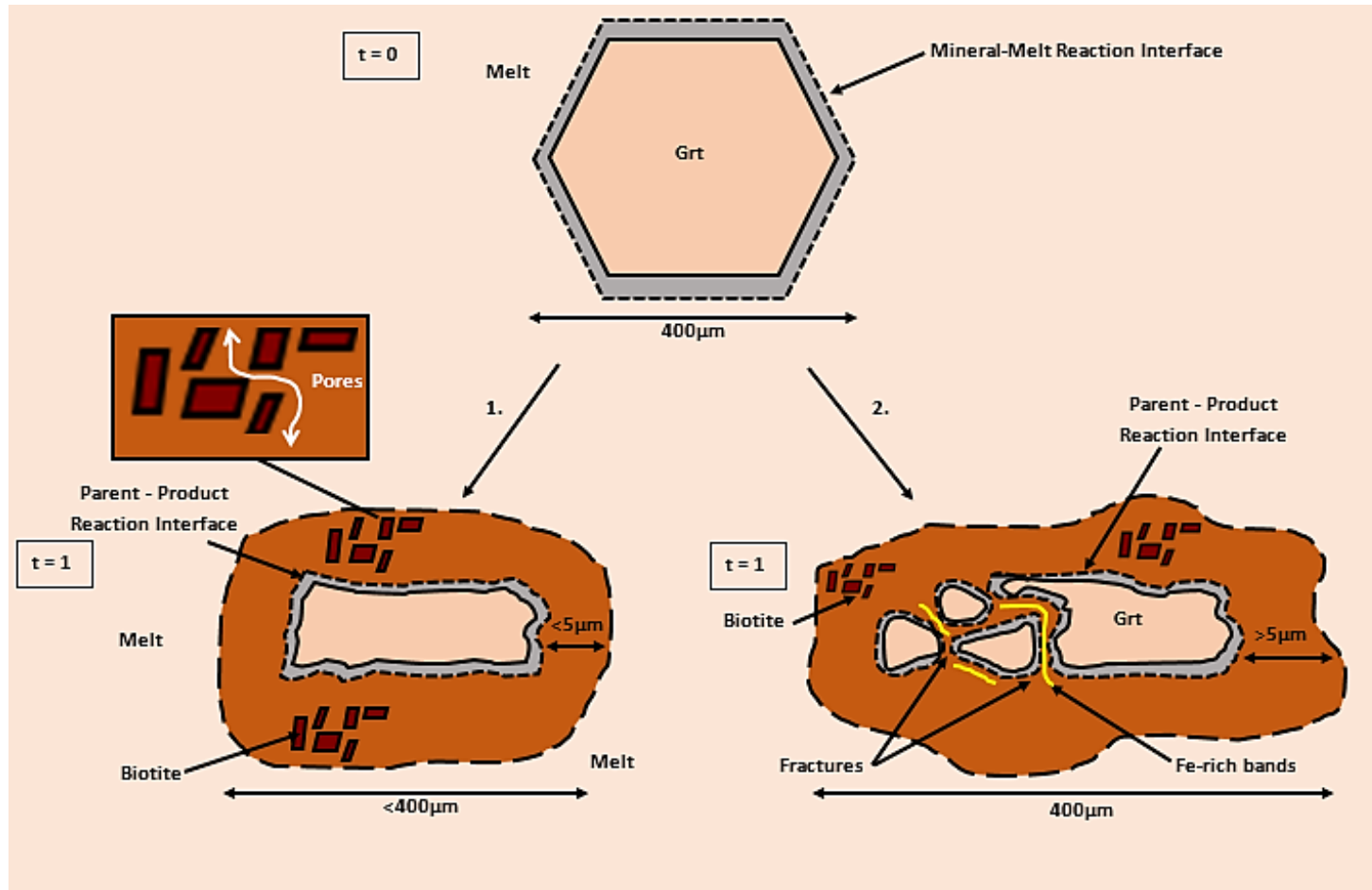


Figure 19 - Schematic of Reaction between Garnet and Melt to Produce Biotite

As this research focuses only on pressure-temperature conditions appropriate to magma emplacement at upper crustal levels, it is plausible that during the magma's ascent garnet would have reacted out of the surrounding magma. Figure 20 (pg.92) shows the various pressure and temperature regions of garnet stability within an average I-type granitic magma composition. It is evident from the figure that the 'peritectic' garnet used within this research is unstable with respects to the surrounding magma for much of the relevant hypersolidus pressure and temperature conditions. Narrow regions exists between 700 and 900°C and between ~9 and 11kbar, in which the 'peritectic' garnet would be a stable phase. However, the 'peritectic' garnets are compositionally dissimilar to the garnet compositions predicted for these pressure-temperature ranges by the phase equilibrium modelling (orange shaded regions). In this region it is proposed that 'peritectic' garnet would react with the surrounding melt portion according to a dissolution-precipitation mechanism. Consequently, at these pressure-temperature conditions the 'peritectic' garnets would behave in a similar manner to those found within the garnets of the Cape Granite Suite (CGS), South Africa. The garnets of the CGS were suggested to have undergone an extremely fast, coupled, dissolution-precipitation mechanism that caused the entrained garnet crystals to partially equilibrate to the lower pressure and temperature conditions of the surrounding S-type granitic magma. Textural evidence of this partial equilibration was observed as chemically zoned garnet crystals, with Mn-rich rims and Mn-poor cores (Villaros et al., 2009a).

As garnet stability appears to be highly pressure dependent, the reaction processes at the pressure-temperature conditions of the source are different to those during magma ascent, as well as those during final magma emplacement at higher crustal levels. At the investigated pressure and temperature conditions the experimental garnets appear homogeneous in composition, and all appear to have reaction rims of biotite. In the experimental run products, biotite armours the garnets, preventing the reaction from running to completion, and ultimately preserving garnet crystals at near subsolidus pressure and temperature conditions. I-type granites are typically devoid of high pressure and temperature minerals, such as garnet (Clemens et al., 2011). However, where garnet exists in these rocks it is characteristically surrounded by biotite (e.g., Maas et al., 1997; Villaros et al., 2009a). The results of the experiments, phase equilibrium modelling (Figure 20, pg. 92), as well as analysis of natural S-type granites shows them to be in good agreement with one another. Figure 20 (pg. 92) indicates that at the pressure-temperature conditions of this research garnet is unstable, and consequently is unable to react according to a dissolution-precipitation mechanism. Instead, within these pressure-temperature regions (blue shaded region) it is proposed that the insoluble components of the 'peritectic' garnet, namely Fe, Mg, Ca, will be taken up by hydrous minerals, such as biotite and clinoamphiboles (tremolite/hornblende) during mineral-melt

reactions. Whilst at corresponding pressures, and higher temperatures (green shaded region) the insoluble components resulting from the 'peritectic' garnet breakdown will be taken up by anhydrous phases, such as; clinopyroxene, orthopyroxene and plagioclase. Consequently, the types of garnet breakdown reactions and the minerals into which insoluble components of the garnets partition is strongly controlled by the pressure and temperature conditions of the surrounding magma.

The experimental garnets, although compositionally homogeneous, no longer resemble the initial 'peritectic' garnets that were seeded into the experimental starting material either texturally or compositionally. Minor changes to the original 'peritectic' garnet composition are evident. There is an overall decrease in the almandine component (58.7 to 55.75 mol. %), which relates to the  $\pm 0.1$  apfu variation in the  $\text{Fe}^{2+}$  component of the garnets across the different high pressure experiments. It is possible that the compositional changes to garnet are the results of an efficient, coupled, dissolution-precipitation mechanism. If this is the case it can be inferred that the dissolution-precipitation mechanism is faster than the transport of  $\text{K}_2\text{O}$  through the melt, as  $\text{K}_2\text{O}$  is an essential component in the production of the biotite reaction rims. However, there is a lack of textural evidence, such as chemical zonation or melt inclusions, within the experimental garnets to support this suggestion. The lack of textural evidence appears to argue for diffusion-related processes between the 'peritectic' garnet composition and the newly precipitated biotite being responsible for the change in garnet geochemistry at the low pressures and temperatures of the experiments. Further evidence supporting this model is the fact that the Fe component of the melt remains steady over all experiments ranging only from 0.5 to 0.6 wt. %. It can, therefore, be inferred that the Fe is partitioned into the biotite rather than the melt portion. Calculations to determine the hypothetical  $\text{FeO} + \text{MgO}$  value within the experimental melts assuming the complete dissolution of garnet were carried out. The findings of the calculations indicate  $\text{FeO} + \text{MgO}$  values in the range of 1.34 to 5.04 across the four experiments in which garnet is evident. These hypothetical values are significantly higher than the  $\text{FeO} + \text{MgO}$  values for the experimental melts which range from 0.57 to 0.68. Textural evidence of the Fe enrichment of biotite includes the existence of Fe-rich bands within the newly precipitated biotite phase (Figure 19, pg.89).

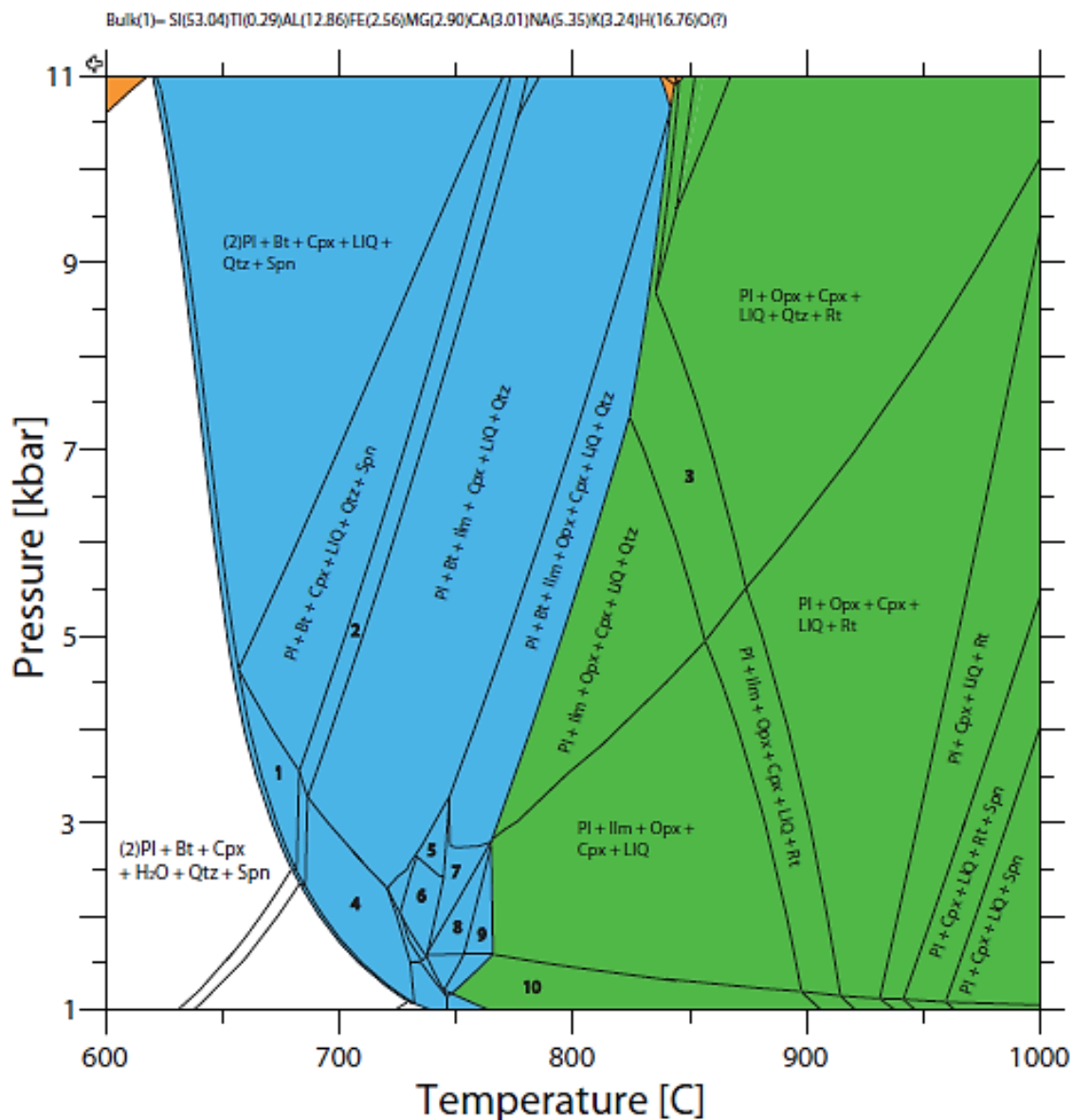


Figure 20 - Garnet Hypersolidus Stability Fields for an Average I-type Granitic Magma Composition. The orange shaded regions are where garnet is stable, but is out of compositional equilibrium with the magma. The green shaded regions indicate where the 'peritectic' garnet is unstable within the magma. At these PT ranges it is proposed that insoluble components (Fe, Mg, Ca) of the garnet will be taken up by anhydrous minerals, such as clinopyroxene, orthopyroxene and plagioclase. The blue shaded area indicates where garnet is similarly unstable, however it is suggested at these PT ranges the insoluble components of the garnet will be taken up by hydrous phases, such as biotite and clinopyroxenes. Across the blue shaded regions, i.e. where garnet is both unstable and out of compositional equilibrium with the magma, garnet will react with the surrounding melt to produce hydrous minerals.

Figure 19 (pg. 89) illustrates the reactions between the experimental garnet and surrounding melt portion at the investigated pressure and temperatures. The image illustrates the two possible outcomes of the mineral-melt reaction process as observed through experimentation. These two outcomes are discussed in detail below.

### **Porosity and Fluid Migration**

Process 1 as illustrated in Figure 19 (pg. 89) shows the outcome of reactions involving the 'peritectic' garnet and the melt phase that has allowed for the precipitation of biotite upon the dissolving 'peritectic' garnet crystal. It is important to note that phase equilibrium modelling predicts that biotite is stable across all pressure-temperature conditions of experimentation, suggesting that the newly precipitated biotite is likely to be in equilibrium with the surrounding magma.

Garnet appears only to be evident in Experiments 2 (1.90kbar and 763°C) to 5 (1.40kbar and 730°C). The lack of garnet in Experiment 1 is probably due to the fact that the analysed section plane was devoid of garnets. The dissolution of garnet appears to be driven by the interaction of the garnet minerals with the surrounding melt through a nanoscale mineral-melt reaction interface (Ruiz-Agudo et al., 2014). The interfacial melt enables the transport of ions (Fe, Mg, Al and Si) both to and from the garnet crystal surface and the surrounding melt. In the case of fluid-saturated conditions this is proposed to be more efficient, as melts with a higher dissolved O-H component have lower viscosities, which results in higher diffusion rates. During this process the interfacial melt becomes supersaturated with respects to a stable product phase, in this case biotite. This supersaturation allows for the biotite to both nucleate and precipitate along the garnet crystal surface (Ruiz-Agudo et al., 2014). The growth of this new phase is therefore interface-controlled (Hammer, 2008). It should be noted that the reaction interface exists parallel to the surface of the garnet crystal, thus producing pseudomorphic replacement of garnet by biotite. The reaction involving garnet and the leucocratic melt is outlined below:



From the experimental results it is clear that the Al component of the surrounding melt remains relatively stable ( $\sigma = 0.50$  wt. %) across the variable temperatures and pressures of experimentation. However, further examination of the biotite shows an increased Al component within its structure, with the Al apfu ranging from 1.60 to 3.59. It is proposed that the Al enrichment observed within the biotite crystals is actually evidence of a trapped Al enriched melt. This enriched melt remains isolated away from the bulk melt composition due to the armouring effects of the newly precipitated biotite phase. This conclusion has been drawn as the biotite crystals are small ( $<2\mu\text{m}$ ), and anhedral in some cases which means that



the uncharacteristically high Al apfu values within the biotite are a consequence of contamination from the high-Al interfacial melt during SEM analysis. Overall the growth of a stable, biotite phase along the experimental garnet surfaces has no effect on the overall bulk melt compositions within the experiments. This may be attributed to the fact that the overall volume of biotite formed within the experiments is relatively small in comparison to the volume of melt.

Although relatively rapid a process, the reaction of the metastable garnet with the melt portion is unable to run to completion during the 10 day experimental run, and consequently garnet is preserved at near-solidus temperatures. The incomplete reaction of garnet can be attributed to two main factors. The first is that the relatively low temperature conditions of the experiments are probably inadequate to allow for a sufficiently fast reaction rate. Secondly, the armouring of garnet by biotite may inhibit the interaction between the garnet and the melt portion. Porosity within the precipitated biotite is essential to allow for reaction between the garnets and melt phases of the system. The amount of porosity is a consequence of the relative proportion of parent to product minerals, as well as their relative solubilities in the interfacial melt (Putnis, 2014; Putnis, 2009; Ruiz-Agudo et al., 2014). If the pore network with the biotite remained open it is plausible that the reaction would have run to completion in spite of the low temperatures of experimentation.

### **Fracturing**

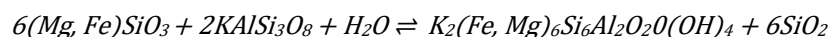
Process 2 (Figure 19, pg. 89) shows the result of stress on the garnet crystal resulting from molar volume differences between the parent mineral (garnet) and the product mineral (biotite). In this case the molar volume of the product, biotite, exceeds that of the parent, garnet, causing the development and propagation of internal fractures within the garnet structure. These fractures result in the formation of small, anhedral garnet fragments. Textural evidence of the stress is observed in the form of biotite growth between the garnet fragments, as well as the development of Fe-rich bands along the fracture planes. The fracturing of the garnet could also be a result of the crushing and milling processes used to prepare the starting bulk composition.

### ***Orthopyroxene - Biotite***

Pyroxenes are rare in exposed I-type granites, but they play an integral role in generating their chemical compositions (Clemens et al., 2011). The 'peritectic' orthopyroxene has a similar fate to that of 'peritectic' garnet, in that it is dissolved by interaction with the melt and a stable, hydrous phase is precipitated along its surface. Similar reactions involving the 'peritectic' orthopyroxene and melt components are observed in the experiments. The balanced reaction (Clemens and Wall, 1988) is outlined overleaf:

## CHAPTER 6: DISCUSSION AND INTERPRETATION

*Orthopyroxene + Melt Components (K-feldspar + Water)  $\rightleftharpoons$  Biotite + Quartz*

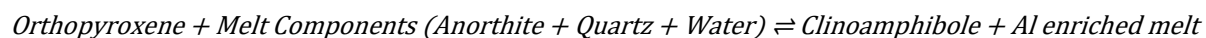


Unlike the experimental garnet, the experimental orthopyroxene completely breaks down and is replaced by biotite in fluid-saturated experiments, at near subsolidus temperatures. The various temperature conditions of the 1.90kbar experiments provide a window into this process. At higher temperatures (763°C) there is an abundance of large orthopyroxene crystals surrounded by narrow rims of biotite (<5µm diameter), whilst in the low-temperature experiments (723°C) the biotite rims are larger at ~10µm width, and the orthopyroxene appears to be almost completely dissolved (<5µm diameter). At this low temperature there are also subhedral masses of biotite plates that appear to be pseudomorphs of the original orthopyroxene crystals. In the higher (743°C) temperature experiment conducted at 1.40kbar orthopyroxene is absent, despite it being predicted over these conditions by the modelling software. These orthopyroxene crystals appear to have completely reacted with the melt to form biotite in a similar manner to those in the higher-pressure experiments (1.90kbar). The small size and complete breakdown of some of the experimental orthopyroxene crystals at low temperatures and pressures supports findings in natural rocks that indicate that orthopyroxenes are rare in I-type granites.

Examination of the stability of 'peritectic' orthopyroxene compositions within the phase equilibrium modelling indicates that at the investigated pressures and temperatures two reaction processes should be evident. In Experiments 1 (733°C and 1.90kbar), 3 (723°C and 1.90kbar) and 5 (730°C and 1.40kbar) the 'peritectic' orthopyroxene is suggested to be unstable, and consequently reacts with the melt phase to form hydrous minerals, such as biotite or clinopyroxene (tremolite/hornblende). Further discrepancies between the inferred reaction processes of the phase equilibrium modelling and those observed within the experiments can be observed across both the higher and lower experimental pressure conditions. In Experiment 2 (763°C at 1.90kbar) and Experiment 4 (743°C at 1.40kbar) the 'peritectic' orthopyroxene is stable, but differs in composition from the orthopyroxene composition predicted by phase equilibrium modelling. At these pressures it is therefore inferred that the dominant reaction process should be dissolution-precipitation. However, examination of the experimental run products indicates that at these pressure and temperature conditions orthopyroxene undergoes reactions with the surrounding melt to precipitate a biotite phase along its surface, and consequently can be considered to be an unstable phase within the magma.

Orthopyroxene reaction to clinopyroxene in natural granitic systems is common (e.g., Clemens and Wall, 1988), although in the case of this research it appears that the reaction of

orthopyroxene to biotite is favoured over clinoamphibole production. The reaction below illustrates a potential reaction involving orthopyroxene and melt components to produce clinoamphibole within the experimental system.



The above reaction, although plausible, appears not to occur within the experimental run products. The reason for this may be due to the fact that the anorthitic component within the melt is too low to facilitate the production of clinoamphibole from orthopyroxene as in the above reaction, whilst the K-feldspar component of the melt is sufficiently high to allow for the reactions between orthopyroxene and melt to produce biotite.

The disconnect between the stability of orthopyroxene as predicted by the phase equilibrium modelling in Figure 21 (overleaf), and as seen in the experimental results is of particular interest. Previous examination of minerals such as garnet, plagioclase and clinopyroxene have shown good agreement between the findings of the two techniques. However, in the case of orthopyroxene it is plausible that the phase equilibrium modelling software overestimates the stability of this mineral phase within the magma. Why this overestimation of orthopyroxene occurs is more difficult to constrain. The fact that biotite appears to be stable at temperatures and pressures above its predicted stability zone (Experiment 2, 763°C and 1.90kbar), suggests that the modelling software has underestimated the stability of biotite as well. This underestimation of biotite within the modelling may be ascribed to the manner in which the biotite model (BI05, White et al., 2005) that was utilized to create the phase equilibrium model, handles the Ti component within the biotite phase. How Ti is handled within the model exerts a strong control on the pressure and temperature stability of phases within the phase equilibrium models (White et al., 2007). As there is a complex interplay between the various mineral models used to develop the phase equilibrium diagram it is likely that the over- and underestimation of these two minerals are interlinked, and that this can account for the deviation between the phase equilibrium modelling and experimental results.

## CHAPTER 6: DISCUSSION AND INTERPRETATION

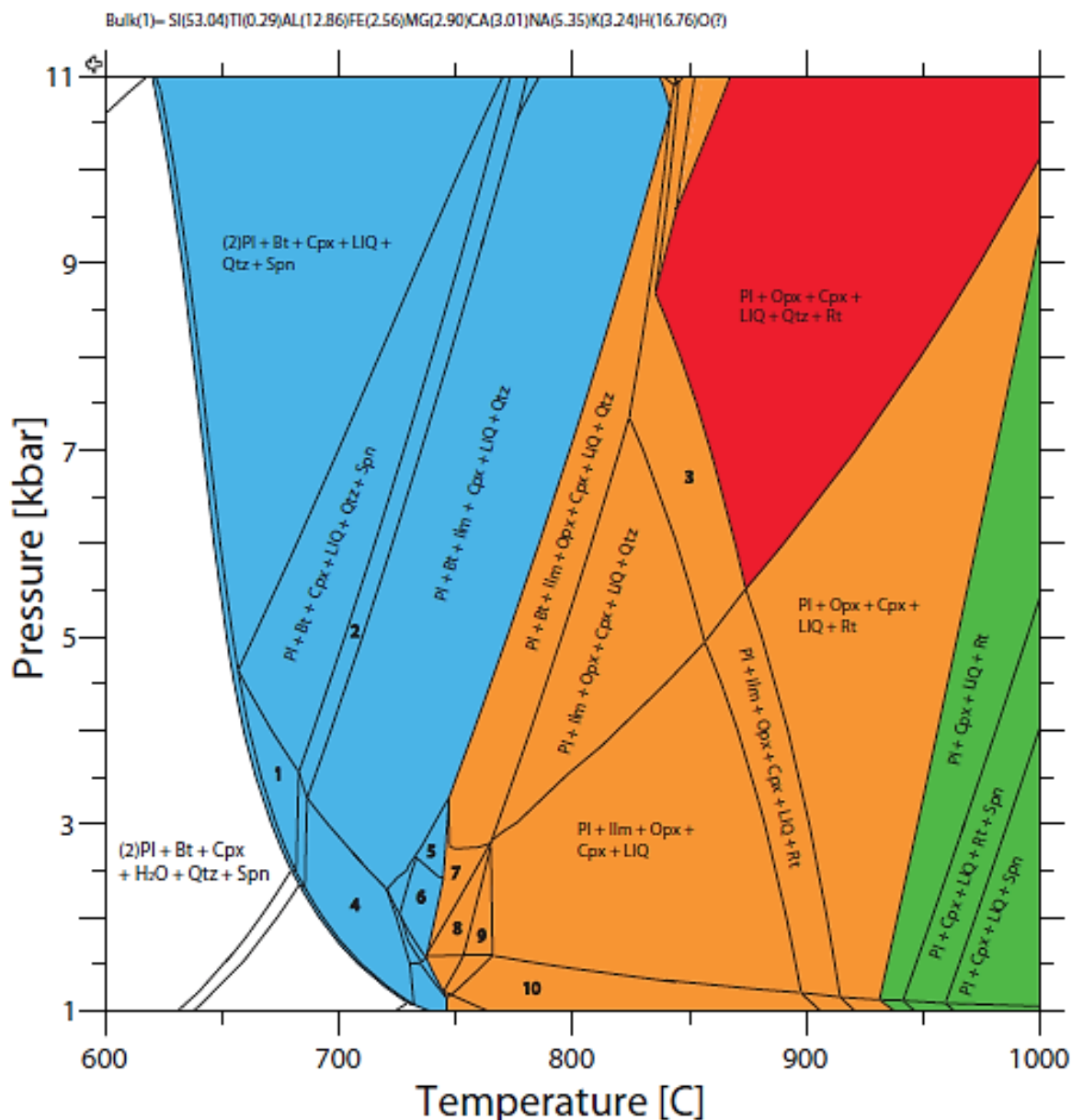


Figure 21 -Orthopyroxene Hypersolidus Stability Fields for an Average I-type Granitic Magma Composition The red shaded region indicates where orthopyroxene is a stable phase, and where the 'peritectic' orthopyroxene is similar in composition ( $X_{En} = \pm 0.02$ ) to the predicted orthopyroxene composition. The orange shaded regions display where orthopyroxene is predicted to be a stable phase, but where the 'peritectic' orthopyroxene has a composition significantly different to that of the predicted orthopyroxene. The blue shaded pressure-temperature regions indicate where orthopyroxene is unstable, and out of compositional equilibrium with the surrounding magma. Across these pressure-temperature ranges the 'peritectic' orthopyroxene is proposed to react with the surrounding melt to form hydrous minerals, biotite or hornblende, in a similar manner to the 'peritectic' garnet.

### 6.3 Melt Compositions

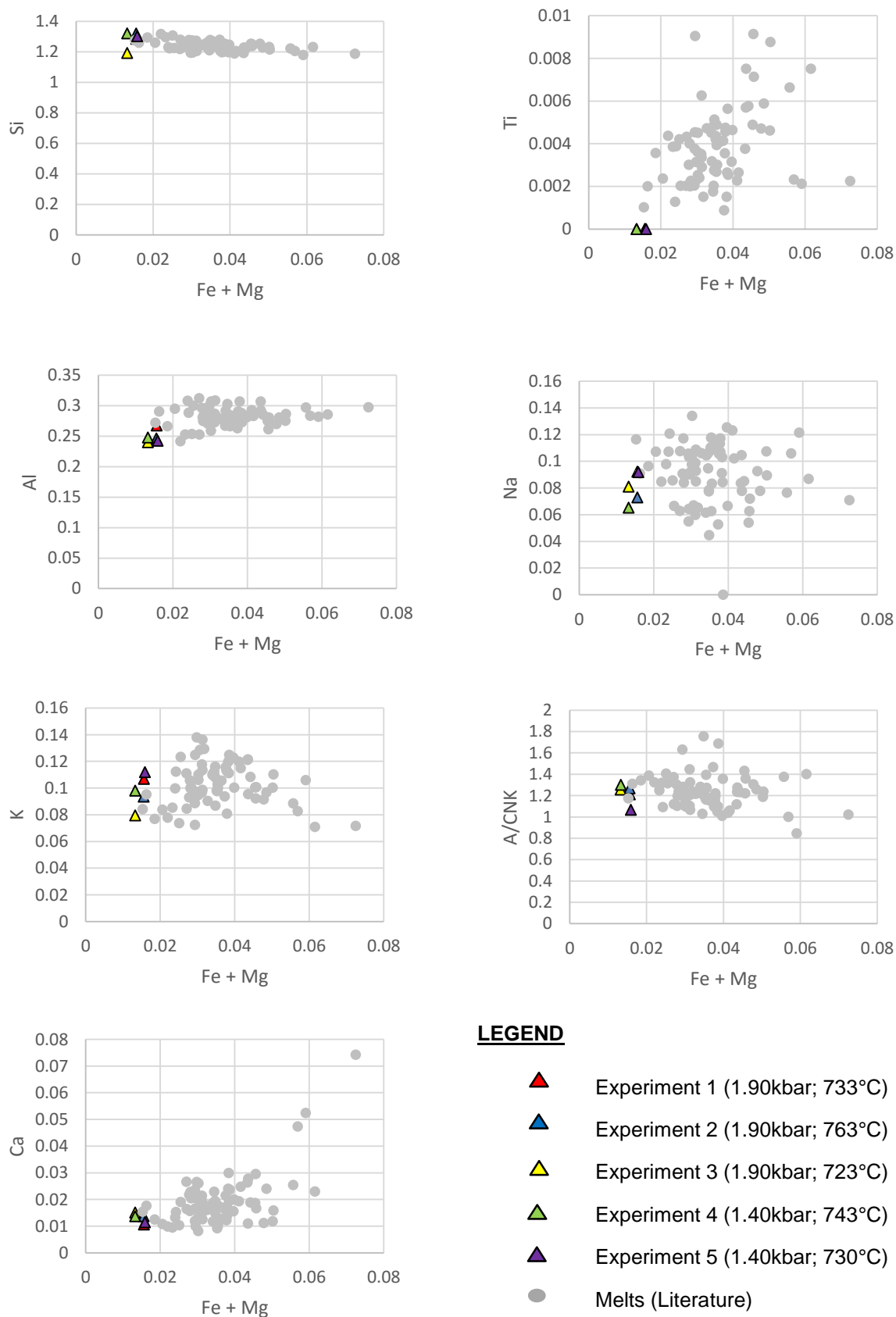


Figure 22 - Bivariate Plots of Melt Major Element Compositions

\*Melt values are normalized anhydrous.

## CHAPTER 6: DISCUSSION AND INTERPRETATION

Figure 22 (pg. 98) shows plots of various elements (moles of element per 100g of rock) against maficity (atomic Fe + Mg per 100g of rock) for the experimental melts, along with compositionally similar melts from the literature. The compositions of the experimental melts are relatively consistent and appears to be largely independent of pressure or temperature. This is evident from the clustered nature of the experimental data presented above. The similarity in the melt compositions suggests that they are largely unaffected by the mineralogical changes to the system that result from multiple, concurrent mineral reactions involving garnet and melt, orthopyroxene and melt, clinopyroxene and melt, and plagioclase and melt.

The compositions of the melts from the literature are strongly peraluminous. They have been generated experimentally by the partial melting of metagreywackes, biotite gneisses and pelites. These compositions were taken from Gardien et al., 1995; Montel and Vielzeuf, 1997; Patiño-Douce and Beard, 1996 and Stevens et al., 2007. Examination of the graphs and melt analyses show that the melt produced in this research is strongly peraluminous. Examination of the Ti versus maficity graph (Figure 22, pg. 98) shows the experimental melts to have no Ti within their compositions. This correlates well with the findings of Clemens et al., (2011) that suggest that the Ti component of an I-type granite magma is concentrated within the peritectic mineral assemblage. Conversely, Clemens et al., (2011) suggest that the K component of the magma is largely present within the melt portion. However, the experimental melt compositions seem to have a low K<sub>2</sub>O component (4.10 to 5.28 wt. % range) when contrasted against other oxides, such as Al<sub>2</sub>O<sub>3</sub>. Steps were taken to reduce the effects of Na and K counting losses during melt analysis on the SEM, in particular the use of liquid nitrogen to freeze the sample at approximately -180°C. The Al composition of the melt remains relatively stable across the investigated pressure and temperature range.

Further analysis of the graphs in Figure 22 (pg. 98) shows the experimental melts to be slightly more leucocratic than the melts taken from the literature. This can be attributed to the different protolithic material used to generate the melts, the low temperature of experimentation, as well as the fact that a significant proportion of the Fe and Mg component within the experimental run products remains within garnet and orthopyroxene minerals that are metastable at the investigated pressures and temperatures of experimentation. The leucocratic nature of these experimental melts is consistent with previous experimental findings by Montel and Vielzeuf, 1997; Stevens et al., 2007; Taylor and Stevens, 2010, that suggest that granitic melts are significantly more leucocratic than average I-type granite compositions. In a similar manner to the findings of Villaros et al., (2009) the melts produced in this research never contain sufficient FeO + MgO to completely digest the entrained ferromagnesian phases, such as garnet. This is one proposal that can potentially account for

the persistence of garnets at the low pressure and temperatures of experimentation. This research demonstrates experimentally, as well as with phase equilibrium modelling, that to recreate a bulk composition aligned with an average to mafic granite composition a leucocratic melt must co-exist with some entrained residuum of mafic composition throughout its magmatic history. And it is the entrainment of this more mafic mineral assemblage that facilitates the formation of AFM mineral components within the granitic melt.

### **6.4 Phase Equilibrium Modelling vs. Experimental Findings**

Theoretical models allow insight into what occurs in a particular geological system if equilibrium is obtained over a range of pressure and temperature conditions. Drawing comparisons between the modelling and experimental techniques is instrumental in understanding the degree to which an experimental run has deviated from the 'ideal' scenario. The experiments conducted in this research are in a non-equilibrium state upon their completion, with disequilibrium features preserved at near-solidus conditions. Anderson (2002, pg. 180) states that it is possible that "no real system ever reaches equilibrium by the criteria applied to modelled systems." The experiments in this research are closed-systems, and therefore cannot replicate certain aspects of natural systems (e.g. external fluid interactions) that can further shift the system away from to towards equilibrium. This fact makes assessing the equilibrium state of experiments in terms of modelling more practicable. The subsections that follow examine the similarities and differences between modelling and experimental results in terms of mineral assemblages, proportions and compositions.



**Modelled vs. Experimental Mineral Assemblages**

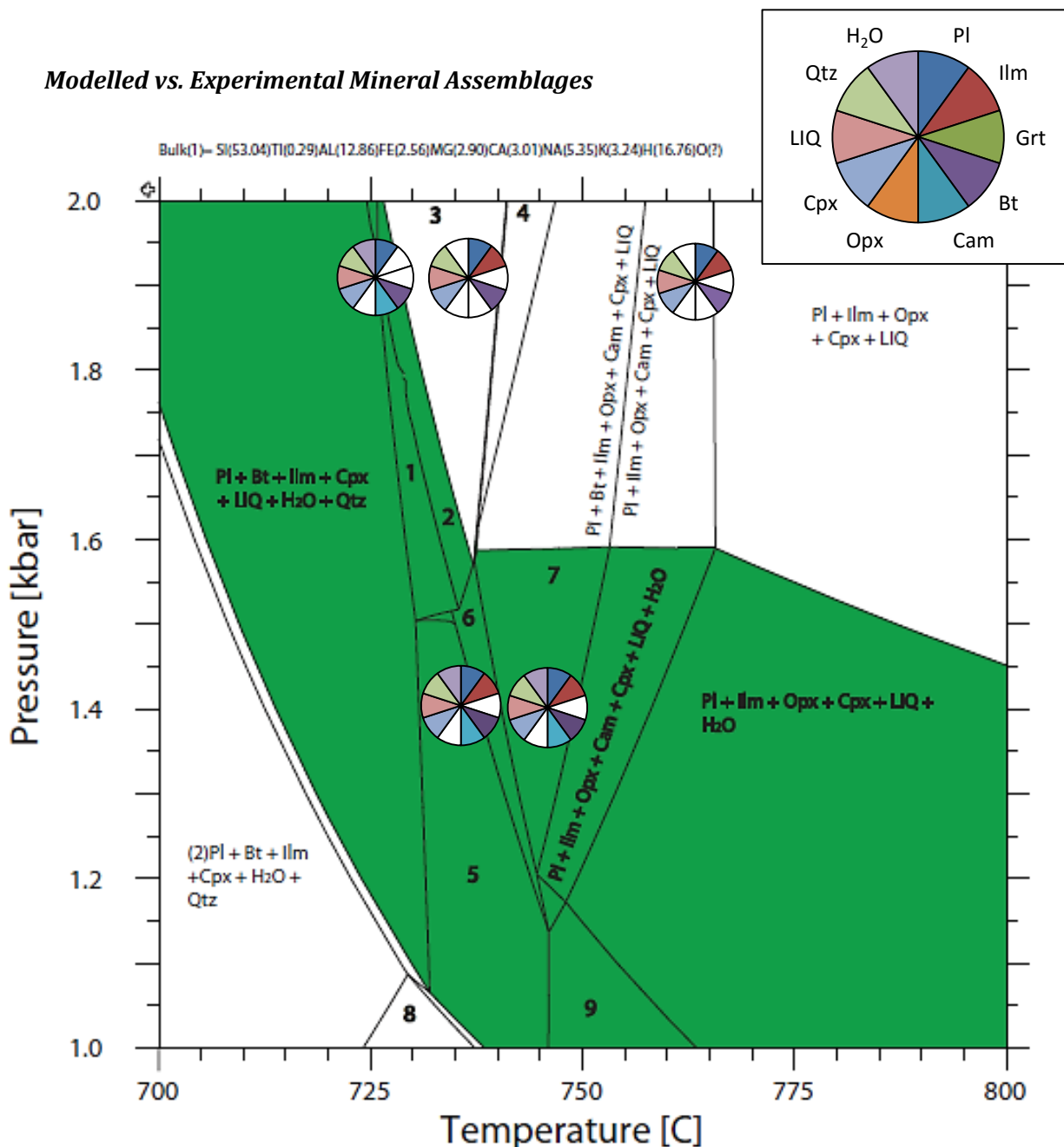


Figure 23 - Modelled vs. Experimental Mineral Assemblages

H<sub>2</sub>O – Melt Saturation Band

- 1 PI + Bt + Ilm + Cam + Cpx + LIQ + H<sub>2</sub>O + Qtz
- 2 PI + Bt + Ilm + (2)Cam + Cpx + LIQ + H<sub>2</sub>O + Qtz
- 3 PI + Bt + Ilm + (2)Cam + Cpx + LIQ + Qtz
- 4 PI + Bt + Ilm + Opx + Cam + Cpx + LIQ + Qtz
- 5 PI + Bt + Ilm + Opx + Cpx + LIQ + H<sub>2</sub>O + Qtz
- 6 PI + Bt + Ilm + Opx + Cam + Cpx + LIQ + H<sub>2</sub>O + Qtz
- 7 PI + Bt + Ilm + Opx + Cam + Cpx + LIQ + H<sub>2</sub>O
- 8 (2)PI + Bt + Ilm + Opx + Cpx + H<sub>2</sub>O + Qtz
- 9 PI + Ilm + Opx + Cpx + LIQ + H<sub>2</sub>O + Qtz

## CHAPTER 6: DISCUSSION AND INTERPRETATION

Figure 23 (pg.102) provides the reader with a visual comparison between the mineral assemblages predicted by the phase equilibrium modelling and those produced by experimentation. In the diagram, phases such as metastable orthopyroxene and metastable garnet have not been included in order to draw more appropriate comparisons between the mineral assemblages produced by the two different approaches. However, the exclusion of these phases from the diagram will mean there is a small mismatch between the modelled bulk composition and the effective bulk composition that applies to the experiments. Examination of Figure 23 (pg. 102) shows that for an average I-type granitic composition exposed to relatively low temperatures and pressure conditions pseudosection modelling is an appropriate tool to predict experimental outcomes. In particular, phases such as Pl, Cpx, and LIQ appear to be both predicted for by the phase equilibrium modelling, as well as evident within the experimental run products across the range of investigated pressures and temperatures. This would suggest that in regards to the aforementioned phases the phase equilibrium modelling and experimental results are in good agreement. The complication arises when one considers the metastable phases in the experimental run products that are not accounted for by the modelling.

The table below provides a further breakdown of the mineral assemblages predicted for by phase equilibrium modelling and those produced through experimentation. Unlike Figure 23 (pg. 102) the table below accounts for the metastable phases within the experimental mineral assemblages. The metastable phases are denoted in red.

**Table 14 - Mineral Assemblage Summary**

Experiment	P (kbar)	T (°C)	Predicted Assemblage	Experimental Assemblage
1	1.90	733	Pl + Bt + Ilm + (2)Cam + Cpx + LIQ + Qtz	Pl + Bt + Ilm + Cpx + LIQ + Qtz
2	1.90	763	Pl + Ilm + Opx + Cam + Cpx + LIQ	Pl + Ilm + <b>Grt</b> + Bt + Ilm + <b>Opx</b> + Cpx + LIQ + Qtz
3	1.90	723	Pl + Bt + Ilm + Cpx + H <sub>2</sub> O + LIQ + Qtz	Pl + Bt + <b>Grt</b> + <b>Opx</b> + Cpx + Cam + LIQ + H <sub>2</sub> O + Qtz
4	1.40	743	Pl + Bt + Ilm + Opx + Cam + Cpx + LIQ + H <sub>2</sub> O	Pl + Ilm + Cpx + <b>Grt</b> + Bt + Cam + LIQ + H <sub>2</sub> O + Qtz
5	1.40	730	Pl + Bt + Ilm + Cpx + LIQ + H <sub>2</sub> O + Qtz	Pl + <b>Grt</b> + Ilm + Cpx + Bt + Cam + LIQ + H <sub>2</sub> O + Qtz

\*Metastable phases are indicated in red.

The differences between the phase equilibrium modelling and the experimental outputs can be attributed to the presence of metastable phases, such as garnet and orthopyroxene. This occurs because the modelling is unable to account for the kinetics, i.e. the reaction rates and reaction pathways, of minerals that have been introduced into a system with which they are out of compositional equilibrium. As the 'peritectic' garnet is out of compositional equilibrium

with the surrounding magma at the investigated pressures and temperatures it reacts to produce biotite. The aforementioned accounts for why biotite is evident in Experiment 2 (1.90kbar; 763°C), which was conducted at pressures and temperatures outside its predicted stability field. The lack of clinoamphibole within Experiment 1 (1.90kbar; 733°C) and Experiment 2 (1.90kbar; 733°C) may relate to the low anorthite melt component, as well as the fact that these experiments lack a free fluid (H<sub>2</sub>O) phase. Similarly, orthopyroxene reacts with the surrounding melt to form biotite. At the pressure and temperature condition of Experiment 4 (1.40kbar and 743°C), orthopyroxene is predicted to be stable, although it appears to be absent in the experimental run products (Table 14, pg.103). This may relate to the compositional difference between the predicted and 'peritectic' orthopyroxene used within the starting bulk composition, or it may be attributable to issues with the modelling that overestimates the stability of orthopyroxene (as discussed previously in the 'Orthopyroxene - Biotite' subsection, pg. 94-97).

### ***Mineral Proportions***

Table 15 (overleaf) compares the volume percentage between the minerals predicted by phase equilibrium modelling and those produced by experimentation. The volume percentage of the experimental minerals was determined using Microsoft Excel Solver Add-In. The most apparent inconsistency between the modelled and experimental data is the presence of metastable garnet and orthopyroxene, along with the absence of clinoamphibole within some of the higher pressure and temperature (1.90kbar; 763°C and 733°C) experimental assemblages. The persistence of garnet and orthopyroxene to pressure-temperature conditions outside their stability field has been discussed in the 'Mineral-Melt Reactions' section (pg. 89).

**Table 15 - Predicted vs. Experimental Mineral Volume Percentages**

Exp.	P (kbar)	T (°C)	Predicted Assemblage	Experimental Assemblage	SSR Values
1	1.90	733	25.3PI + 6.0Bt + 0.4Ilm + 4.3(2)Cam + 2.1Cpx + 56.9LIQ + 5.0Qtz	29.6PI + 1.2Ilm + 4.5Cpx + 14.6Bt + 32.7LIQ + 17.5Qtz	0.76
2	1.90	763	21.2PI + 0.5Ilm + 5.2Opx + 0.7Cam + 3.0Cpx + 69.4LIQ	11.8PI + 0.0Grt + 18.2Bt + 1.5Ilm + 0.2Opx + 6.8Cpx + 55.4LIQ + 6.0Qtz	1.99
3	1.90	723	29.4PI + 10.9Bt + 0.4Ilm + 3.4Cpx + H <sub>2</sub> O + 43.6LIQ + 12.3Qtz	14.3PI + 6.7Bt + 7.5Grt + 0.0Opx + 7.1Cpx + 0.0Cam + 63.5LIQ + H <sub>2</sub> O + 1.0Qtz	1.24
4	1.40	743	24.5PI + 0.8Bt + 0.5Ilm + 4.0Opx + 3.5Cam + 1.8Cpx + 64.9LIQ + H <sub>2</sub> O	19.3PI + 0.8Ilm + 0.0Grt + 8.4Bt + 10.6Cam + 7.0Cpx + 42.0LIQ + H <sub>2</sub> O + 11.9Qtz	1.15
5	1.40	730	32.6PI + 11.2Bt + 0.4Ilm + 3.4Cpx + 38.0LIQ + H <sub>2</sub> O + 14.4Qtz	13.9PI + 18.1Bt + 0.0Grt + 1.1Ilm + 6.8Cpx + 50.1LIQ + H <sub>2</sub> O + 1.0Cam + 9.1Qtz	0.43

\*Metastable phases are indicated in red.

\*Experimental assemblage proportions calculated using Excel Solver Add-in.

\*SSR values show minimized deviation between the predicted and experimental mineral proportions.

Hornblende is the dominant clin amphibole mineral of I-type granitic rocks (Clemens et al., 2011), and has a general mineral formula of  $\text{Ca}_2(\text{Mg,Fe,Al})_5(\text{Al, Si})_8\text{O}_{22}(\text{OH})_2$ . The low modal proportion of clin amphibole in the experimental run products is likely to be a consequence of high Al, Fe and Mg minerals, specifically garnet, orthopyroxene and biotite, being present in considerably greater proportions than predicted for by the modelling software. It is possible that had the experimental assemblage been exposed to pressure-temperature conditions aligned with magma ascent, the digestion of garnet and orthopyroxene through mineral-melt reactions would have run to completion, thus allowing for greater proportions of clin amphibole to be produced. The lack of clin amphibole produced in Experiment 1 (733°C and 1.90kbar) and Experiment 2 (763°C and 1.90kbar) will have minimal effect on the equilibrium nature of the experimental magma, as only a small percentage of clin amphibole was predicted at the pressure-temperature conditions of experimentation (max. predicted vol. % = 4.3 % in Experiment 1).

In the case of Experiment 3 (1.90kbar; 723°C) the Excel solver determined that 0% orthopyroxene existed in the experimental run product. Analysis of the run product of the same experiment shows minor quantities of metastable orthopyroxene. In general the quantities of orthopyroxene are lower in the experiments than anticipated. The greatest deviation from the predicted proportion can be seen in Experiment 2 at 0.2 vol. %, instead of the predicted 5.2 vol. %. Conversely, clinopyroxene exists in significantly higher quantities than predicted. At 1.90kbar the phase equilibrium modelling predicts ranges of 2.1 to 3.4 vol. % for clinopyroxene, whilst the experimental proportion is significantly higher, ranging between 4.5

to 7.1 vol. %. Similar discrepancies can be seen in the 1.40kbar experiments which predict ranges of 1.8 to 3.4 vol. % clinopyroxene, whilst the experimental proportions range between 6.8 to 7.0 vol. % clinopyroxene.

The proportion of plagioclase predicted and the volume produced through experimentation appears similar at 1.90kbar and 733°C. However, the proportion of plagioclase in the high and low temperature experiments run at 1.90kbar differ dramatically ( $\pm 15.1$  vol. %). In the case of the lowest-temperature experiment (723°C) the phase equilibrium modelling placed the pressure-temperature conditions of the experiment within the H<sub>2</sub>O-melt saturation band. The high volumes of silicate melt within this experiment would inhibit the formation of a large portion of plagioclase at these pressure-temperature conditions, as it is Si, Al and Na rich. In much the same way, the availability of Si in the melt is considered to vary narrowly ( $\pm 2.18$  wt. % SiO<sub>2</sub>) with the growth of newly precipitated minerals, such as biotite, and across varying experimental temperature conditions. If insufficient Si is available within the melt the proportion of magmatic quartz that is precipitated will be limited. This is evident in Experiment 3 (1.90kbar and 723°C) where 12.3 vol. % quartz was predicted, but only 1.0 vol. % was present in the experimental run product.

Comparisons between the volume percent melt in the model versus the experiments indicate that the values are relatively consistent. The greatest variation between the two is seen in Experiment 1 (1.90kbar and 723°C) and Experiment 4 (1.40kbar and 730°C) with the predicted volume percentage of melt being 22.9 to 24.2 vol. % lower than the experimental results.

The SSR Values within Table 15 (pg.105) indicate the minimized deviation between the predicted and experimental mineral proportions. As these values are low ( $<1.99$ ) it suggests that there is a strong level of agreement between the predicted mineral proportions and the proportions of minerals produced within the experimental run products. It is suggested that without the presence of metastable phases, such as orthopyroxene and garnet in the experiments, these SSR values would be even lower.

### ***Mineral Compositions***

Table 16 (pg.109) and Table 17 (pg.110) illustrate the compositional differences between the predicted and experimental minerals for each experiment. The tables show both the mineral formulae and the mol. % values (where applicable) of the predicted and experimental mineral assemblages to allow for comparisons to be drawn between the two. It is essential to note that as modelling software represents an 'ideal' scenario it cannot account for mineral impurities and heterogeneities that may exist within the experimental mineral phases (Anderson, 2002).

These mineral impurities and heterogeneities can, in part, account for the minor discrepancies between the predicted and experimental compositions.

There are a few major deviations between the experimental results and phase equilibrium modelling outputs. The most significant is the presence metastable garnet and orthopyroxene in some of the experimental assemblages. Another discrepancy is fact that the analysis of experimental biotite and clinopyroxene were contaminated by surrounding crystals and/or quenched melt. Where biotite crystals were large enough to analyse, the needle-like network of the crystals meant the surface was not flat enough to obtain an accurate analysis. Thus these mineral compositions have been excluded from Table 16 (pg. 109) and Table 17 (pg. 110). There is also a considerable difference in the mol. % formula of the clinopyroxenes (diopside) predicted for the 1.90kbar experiments and those in the experiments themselves. The experimental clinopyroxenes have  $X_{Di}$  values greater than 0.92, compared to the 0.46 to 0.62 predicted for by the modelling software at corresponding temperatures and pressures. At the approximate conditions of the source (~9kbar and 850°C) the phase equilibrium modelling predicts a clinopyroxene composition of 61.49 mol. % diopside. Therefore the discrepancy between the two values is likely ascribed to the fact that an ideal diopside was used as the 'peritectic' clinopyroxene phase within the starting bulk composition of the experiments. This is the case for all of the 'peritectic' phases seeded into the starting bulk composition, and its effects are widespread. As described by White et al., (2011), differences between modelled mineral compositions and those in experiments can account for the differences in the mineral proportions and assemblages produced by the two techniques. This is suggested to be because experiments are closed systems, and thus "mass balance requirements" must be maintained within the set experimental bulk composition (White et al., 2011, pg. 244).

At first glance the mol. % formula of the experimental orthopyroxene is considered to differ significantly from the predicted data. This is due to the Theriak-Domino modelling software accounting for a theoretically 'ordered' orthopyroxene known as 'Fm', which the software automatically includes in the mol. % breakdown of the orthopyroxene mineral composition. By not taking this 'Fm' component into account the normalized enstatite component is still significantly lower (50.0 to 58.4) than the corresponding enstatite mol. % of the experimental orthopyroxenes (65.5 to 78.8).

### ***Concluding Remarks***

The mineral assemblages, proportions and compositions of the modelled and experimental datasets have been shown to be similar. The correlation between the two research media would strongly suggest that modelling in the case of I-type granites is an appropriate method to formulate, as well as interpret experiments. However, it appears that caution must be

exercised in drawing parallels between the experimental and modelled findings, particularly in the use of biotite and amphibole solution models. It appears that for an average I-type granite composition subjected to low pressures (~2kbar) and temperatures (~720 - 770°C) these models significantly misjudge the stability of mineral phases, such as clinopyroxene, biotite and orthopyroxene. Where the compositions and proportions of minerals differ between the two methods it can largely be attributed to the presence of metastable garnet and orthopyroxene in the experimental run products. The felsic minerals appear to be the most in keeping with the modelled equilibrium data in terms of composition and proportions, whereas minerals with a higher ferromagnesian component, such as orthopyroxene, differ substantially. Textural and compositional evidence both through the analysis of the experimental run products and phase equilibrium modelling would argue for grain-scale disequilibrium in the I-type granitic magma of this research.

Table 16 - Predicted vs. Experimental Mineral Compositions (1.90kbar)

Higher Pressure Isobaric Cooling Path (1.90kbar)								
	Experiment 1 - 733°C			Experiment 2 - 763°C			Experiment 3 - 723°C	
	Predicted	Experimental		Predicted	Experimental		Predicted	Experimental
Pl	NaAlSi <sub>2.5</sub> O <sub>8</sub> X <sub>Ab</sub> = 0.57	Na <sub>0.6</sub> Ca <sub>0.4</sub> Al <sub>1.4</sub> Si <sub>2.7</sub> O <sub>8</sub> X <sub>Ab</sub> = 0.61	Pl	NaAlSi <sub>2.5</sub> O <sub>8</sub> X <sub>Ab</sub> = 0.52	Na <sub>0.4</sub> Ca <sub>0.5</sub> Al <sub>1.5</sub> Si <sub>2.6</sub> O <sub>8</sub> X <sub>Ab</sub> = 0.43	Pl	NaAlSi <sub>2.6</sub> O <sub>8</sub> X <sub>Ab</sub> = 0.61	Na <sub>0.6</sub> Al <sub>1.3</sub> Si <sub>2.7</sub> O <sub>8</sub> X <sub>Ab</sub> = 0.62
Ilm	FeTiO <sub>3</sub>	Fe <sup>2+</sup> <sub>0.9</sub> Fe <sup>3+</sup> <sub>0.1</sub> Mn <sub>0.1</sub> Mg <sub>0.1</sub> Ti <sub>0.9</sub> O <sub>3</sub>	Ilm	FeTiO <sub>3</sub>	Fe <sup>2+</sup> <sub>0.8</sub> Fe <sup>3+</sup> <sub>0.2</sub> Mn <sub>0.1</sub> Ti <sub>0.9</sub> O <sub>3</sub>	Ilm	FeTiO <sub>3</sub>	-
Opx	-	-	Opx	FeMgSi <sub>2.0</sub> O <sub>6</sub> X <sub>En</sub> = 0.58	Mg <sub>1.5</sub> Fe <sub>0.4</sub> Si <sub>1.6</sub> O <sub>6</sub> X <sub>En</sub> = 0.78	Opx	-	Mg <sub>1.3</sub> Fe <sub>0.7</sub> Si <sub>1.9</sub> O <sub>6</sub> X <sub>En</sub> = 0.65
Cpx	CaMgSi <sub>2.0</sub> O <sub>6</sub> X <sub>Di</sub> = 0.49	Ca <sub>0.9</sub> Mg <sub>0.9</sub> Fe <sub>0.2</sub> Si <sub>1.9</sub> O <sub>6</sub> X <sub>Di</sub> = 1.00	Cpx	CaMgSi <sub>2.0</sub> O <sub>6</sub> X <sub>Di</sub> = 0.62	Ca <sub>0.8</sub> Mg <sub>0.9</sub> Fe <sub>0.4</sub> Si <sub>2.0</sub> O <sub>6</sub> X <sub>Di</sub> = 0.98	Cpx	CaMgSi <sub>2.0</sub> O <sub>6</sub> X <sub>Di</sub> = 0.46	Ca <sub>0.9</sub> Mg <sub>0.8</sub> Si <sub>1.9</sub> O <sub>6</sub> X <sub>Di</sub> = 0.92
Grt	-	-	Grt	-	Al <sub>2.0</sub> Fe <sub>1.7</sub> MgSi <sub>3.0</sub> O <sub>12</sub>	Grt	-	Al <sub>2.0</sub> Fe <sub>1.6</sub> MgSi <sub>3.0</sub> O <sub>12</sub>
Bt	KFeMg <sub>2</sub> AlSi <sub>3.0</sub> O <sub>10</sub> (OH) <sub>2</sub>	***	Bt	-	***	Bt	KFeMg <sub>2</sub> AlSi <sub>3.0</sub> O <sub>10</sub>	***
Cam	Ca <sub>2</sub> Mg <sub>5</sub> Si <sub>7.9</sub> O <sub>22</sub>	-	Cam	Ca <sub>2</sub> Mg <sub>5</sub> Si <sub>7.9</sub> O <sub>22</sub>	-	Cam	-	***

\*\*\* Mineral phases have been identified using SEM analysis, although the exact compositions of these phases are unknown. Small crystal sizes has meant analysis of these phases are contaminated by surrounding minerals and/or quenched melt.



Table 17 - Predicted vs. Experimental Mineral Compositions (1.40kbar)

Lower Pressure Isobaric Cooling Path (1.40kbar)					
	Experiment 4 - 743°C			Experiment 5 - 730°C	
	Predicted	Experimental		Predicted	Experimental
Pl	$(\text{Na}_{0.5}\text{Ca}_{0.4})\text{AlSi}_{2.6}\text{O}_8$ $X_{\text{Ab}} = 0.55$	$(\text{Na}_{0.6}\text{Ca}_{0.4})\text{Al}_{1.3}\text{Si}_{2.7}\text{O}_8$ $X_{\text{Ab}} = 0.63$	Pl	$\text{NaAlSi}_{2.7}\text{O}_8$ $X_{\text{Ab}} = 0.62$	$\text{Na}_{0.6}\text{Ca}_{0.4}\text{Al}_{1.4}\text{Si}_{2.6}\text{O}_8$ $X_{\text{Ab}} = 0.62$
Ilm	$\text{FeTiO}_3$	$\text{Fe}^{2+}_{0.5}\text{Fe}^{3+}_{0.8}\text{Ti}_{0.4}\text{O}_3$	Ilm	$\text{FeTiO}_3$	$\text{Fe}^{2+}_{0.8}\text{Fe}^{3+}_{0.2}\text{Mn}_{0.1}\text{Ti}_{0.9}\text{O}_3$
Opx	$\text{FeMgSi}_{2.0}\text{O}_6$ $X_{\text{En}} = 0.50$	-	Opx	-	-
Cpx	$\text{CaMgSi}_{2.0}\text{O}_6$ $X_{\text{Di}} = 0.56$	$\text{Ca}_{0.5}\text{Mg}_{1.1}\text{Fe}^{2+}_{0.3}\text{Si}_{1.9}\text{O}_6 /$ $\text{Ca}_{0.9}\text{Mg}_{0.9}\text{Fe}^{2+}_{0.2}\text{Si}_{1.9}\text{O}_6$ $X_{\text{Di}} = 1.00$	Cpx	$\text{CaMgSi}_{2.0}\text{O}_6$ $X_{\text{Di}} = 0.46$	$\text{CaMgSi}_{2.0}\text{O}_6$ $X_{\text{Di}} = 1.00$
Grt	-	$\text{Al}_{3.0}\text{Fe}_{2.0}\text{Mg}_{0.8}\text{Si}_{3.0}\text{O}_{12}$	Grt	-	$\text{Al}_{2.0}\text{Fe}_{1.7}\text{Mg}_{0.9}\text{Si}_{3.0}\text{O}_{12}$
Bt	$\text{FeMg}_2\text{AlSi}_{3.0}\text{O}_{10}$	***	Bt	$\text{FeMg}_2\text{AlSi}_{3.0}\text{O}_{10}$	***
Cam	$\text{Ca}_2\text{Mg}_5\text{Si}_{7.9}\text{O}_{22}$	***	Cam	-	***

\*\*\* Mineral phases have been identified using SEM analysis, although the exact compositions of these phases are unknown. Small crystal sizes has meant analysis of these phases are contaminated by surrounding minerals and/or quenched melt.

## 6.5 Implications for Natural Systems

The findings of this research have important implications for the 'fates' of entrained high pressure and temperature mineral phases within granitic magmas in general. The following discussion relates the experimental results to; the 'fate' of entrained crystals in granitic magmas, the compositional and textural features of granitic rocks, the ascent and emplacement mechanisms of felsic magmas, and the implications for volcanic magmas.

### *Fate of Entrained Minerals*

The fate of entrained 'peritectic' minerals, as observed within this research, has far-reaching consequences that extend beyond both the peritectic assemblage entrainment model and plutonic rocks. Formational models such as fractional crystallization, magma mixing, peritectic entrainment and restite entrainment are all based on the principle of a crystal-rich magma ascending through the crust. The findings of this research suggest that irrespective of the process responsible for the formation of granite magmas, the entrained crystal load is able to equilibrate rapidly and effectively during magma ascent and final emplacement at upper crustal levels. The lack of observable compositional and textural evidence of peritectic material is a common feature of granitic rocks, and is hypothesized to result from the fact that the crystals, although abundant within granitic magmas, are small when they are entrained (Clemens and Stevens, 2012). These peritectic crystals are thought to re-equilibrate to the pressure, temperature and compositional conditions of the surrounding magma during the magma's ascent (Clemens and Stevens, 2012). This research has shown this to be true at the low pressure and temperature ranges appropriate to granitic magma emplacement within the higher crust.

The most prominent evidence of mineral re-equilibration in the experimental results is the textural and compositional disappearance of the originally entrained 'peritectic' phases. 'Peritectic' phases re-equilibrate either partially or fully, in the experiments according to two key reaction processes, a coupled dissolution-precipitation mechanism, and mineral-melt reactions. Which of the two processes is responsible for changing both the compositional and textural features of the 'peritectic' phases is largely dependent on the stability and equilibrium characteristics of the mineral phases in the surrounding magma. Minerals that are stable, but out of compositional equilibrium with the surrounding magma will react according to a coupled dissolution-precipitation mechanism. Unstable phases react with the melt by mineral-melt reactions to produce reaction rims of more stable, hydrous phases, such as biotite and clinoamphibole. These mineral-melt reactions are 'sluggish' in comparison to the dissolution-precipitation mechanism, and their slower rates allow for the persistence of high-pressure and -temperature phases, such as garnet and orthopyroxene, to near-solidus conditions (~ 730°C

at 1.40kbar; ~720°C at 1.90kbar). Although these phases may be present in crystalline granitic rocks, they bear no compositional or textural resemblance to the originally entrained 'peritectic' phases, due to their continual re-equilibration to the surrounding magmatic conditions. This supports petrographic findings in both I- and S-type granitic rocks that show them to be typically devoid of entrained residuum, early magmatic phases, and peritectic phases (Clemens et al., 2011). However, where these phases are evident within natural granitic rocks, they appear to be armoured by reaction rims of minerals, such as biotite and quartz (e.g., Villaros et al., 2009a).

Discrepancies between this experimental study and phase equilibrium modelling can be attributed to two main factors. The first is that the starting bulk composition was never exposed to the higher-pressure conditions of magma ascent. Points along a hypothetical magma ascent path were not recreated experimentally, as this was beyond the scope of the study. The cold-seal pressure vessel was also unable to attain geologically relevant pressure and temperature conditions to recreate various points along an isothermal decompression adiabat. Instead, the experimental results were generated assuming instantaneous ascent mechanisms, and are each appropriate only to pressure and temperature conditions of granitic magma emplacement within the upper crust. It is proposed that had the 'peritectic' mineral phases been exposed to the higher-pressure conditions associated with granite magma ascent they would have been completely replaced by hydrous phases by mineral-melt reactions.

The second discrepancy between the two techniques relates to the fact the natural minerals used to develop the synthetic 'peritectic' mineral assemblage, were compositionally different to those predicted by the modelling software at conditions of the source (~10kbar and 850°C), as well as at conditions of initial emplacement (~2kbar and 800°C). However, the fact that the experimental results appear to correlate well with natural findings in granitic rocks, particularly in terms of re-equilibration and new mineral growth, suggests that entrained phases or early-formed magmatic phases are also out of compositional equilibrium with their surrounding magma at some point within the magmatic history. Consequently, these minerals are constantly re-equilibrated, either through dissolution-precipitation mechanisms or through mineral-melt reactions, to the conditions of the surrounding magma throughout its ascent and emplacement.

### ***Magma Ascent and Emplacement***

Unlike models involving diapiric methods of vertical magma transport, ascent through dykes and shear zones has been shown to be both a viable and fast process (~0.01 m/s for a dyke of 3-13 m width) (Clemens, 2012). The emplacement of granitic magmas involves a shift flow from a vertical to a horizontal plane (Petford et al., 2000). According to recent literature it is

not feasible to suggest that magma ascends and is emplaced in a solitary event, due to the fact that there is insufficient space available in the upper crust to accommodate the massive influx of magma (Petford et al., 2000). Instead it is proposed that plutons are built up in successive magma pulses that can ascend from the source to emplacement levels in a matter of weeks or months (Clemens, 2012). These pulses of magma are suggested to account for the small- to large- scale chemical heterogeneities observed within many granites. In the field I-type granites typically display petrographic evidence of being emplaced in pulses of magma, as discussed above. They appear as fine-grained dykes, and within these dyke structures crystal masses form according to gravity and flow driven processes (Clemens et al., 2011).

It is proposed that if continuous decompression experiments (at rates corresponding to Clemens (2012)) were conducted on the starting bulk composition of this research they would produce well equilibrated run products. The assumption is based on the observed rapid equilibration of minerals, such as plagioclase, in under 10 days at low pressure and temperature ranges, e.g. 1.40kbar; 730°C. The findings of this research would therefore suggest a fast ascension rate (weeks to months timescale), is unlikely to inhibit the partial or full equilibration of entrained residuum or early magmatic phases within a granitic magma. The findings of this research appear to support fast ascent rates being feasible to aid in the production of both the textural and geochemical characteristics of granitic rocks, in particular their distinct lack of compositional and textural evidence of high-temperature and -pressure source, and near-source, mineral components.

### ***Mineral Textures***

Beyond the mode of ascent the idea that a granite body's geochemical and textural features, such as large crystal sizes, are a product of long residency times and slow cooling rates has been shown by the experimental research to be unnecessary. In a period of 10 days feldspathic, and some ferromagnesian components, of the experimental magma were able to fully dissolve and precipitate as/more equilibrated phases. Newly precipitated minerals, such as biotite, plagioclase and magmatic quartz, displayed rapid growth rates across variable, low temperatures (~720 - 770°C) and pressures (~2kbar). Similar experiments by Swanson (1977) on the nucleation and growth rates of minerals in the simple  $\text{KAlSi}_3\text{O}_8$  -  $\text{NaAlSi}_3\text{O}_8$  -  $\text{CaAlSi}_3\text{O}_8$  system showed the average crystal growth rates in a synthetic granite/granodiorite composition exposed to 400- 900°C at 8kbar to be in the range of 3 mm per day to 1 mm per year depending on  $\text{H}_2\text{O}$  contents and the degree of undercooling. Emplaced magmas do not require long residency times or slow cooling rates within the magma chamber to produce the distinct compositional, or typical textural features of granitic rocks.

***Implications for Volcanic Magmas***

Finally, the concepts mentioned above have implications for the development of volcanic rocks, such as dacites and rhyolites, as well. The geochemistry of these volcanic magmas, the mode and pressure-temperature conditions of their formation, as well as the mechanisms of their ascent are considered to be similar to those of granitic rocks (Clemens, 2012 and references therein). Thus it is likely that volcanic magmas exist as a combination of crystals and melt throughout their magmatic history in much the same way as granitic magmas. The similarities between the formation and ascent of granitic and volcanic magmas, suggests that the entrained crystals within volcanic magmas can attain equilibrium at a similarly fast rate to mineral phases within ascending granitic magmas. The proposed rapid equilibration of the entrained minerals and early magmatic phases during the volcanic magma's ascent through the crust, along with the rapid cooling rate of the magma upon its eruption at the surface, supports the lack of compositional and textural evidence of this entrained residuum within these rocks (Clemens et al., 2011). However, volcanic and plutonic rocks differ significantly in their texture. The aphanitic textures of volcanic rocks, along with the evidence of mineral disequilibrium features, such as sieve textures and resorption features within plagioclases (e.g., Hosseini et al., 2014), are a consequence of rapid decompression associated with eruption (Nelson and Montana, 1992). Consequently, the 'fate' of minerals in volcanic magmas can largely be ascribed to the conditions and rates of eruption.

## Chapter 7: Conclusions and Recommendations

### 7.1 Conclusions

The generation of average to mafic granite compositions can be ascribed to the entrainment of mafic minerals in a leucogranitic melt (Clemens et al., 2011). Phase equilibrium modelling, combined with the experimental findings of this research have validated this premise, particularly in terms of the formation of an average I-type granodioritic composition. Experimental results have indicated that even at the low pressure (~2kbar) and temperature conditions (>700°C) appropriate to magma emplacement within the upper crust, a granitic magma will have the capacity to either partially or fully equilibrate any crystal component that is out of compositional equilibrium with the surrounding magma. This will hold true for any petrogenetic process that is responsible for the formation of crystal-rich granitic magmas, such as; peritectic phase entrainment, magma mixing at depth, fractional crystallization at depth, assimilation and restite entrainment.

The 'fate' of minerals in an I-type granite magma intruded at a pressure below 2kbar has been shown to be primarily controlled by two main reaction processes; coupled dissolution-precipitation mechanism, and mineral-melt reactions. The type of reaction processes experienced by each mineral phase is largely controlled by three factors. The first relates to the stability of the mineral phase in the magma. The second relates to whether the mineral is in compositional equilibrium with the surrounding magma. Finally, the type of reaction is also strongly dependent on the pressure and temperature conditions of the surrounding magma. Both reaction mechanisms drive the entrained 'peritectic' mineral phases in the direction of compositional and textural equilibrium at low magmatic temperatures.

The findings of this research suggest that it would be incorrect to assume that mineral phases in granitic rocks directly reflect the compositions or textures of the same mineral phases entrained at or near source levels. Granites, in this regard, do not appear to image their sources. Instead, the compositional and textural 'fates' of entrained and early magmatic mineral phases are a result of complex interrelationships between pressure, temperature, mineral stability and the degree of compositional equilibrium of the mineral phases in a granitic magma.

### 7.2 Summary of Contributions

- Experimentally verified the types of reaction processes responsible for the partial/full equilibration of entrained mineral phases within I-type granite magmas.

- Established a relative time frame for dissolution-precipitation mechanisms in I-type granite magmas, particularly in the case of plagioclase.
- Demonstrated that originally entrained high pressure and temperature minerals are texturally and compositionally distinct from mineral phases observed at low pressures (~2kbar) and temperatures (~700-770°C).
- Determined the key similarities and differences, in terms of an average I-type granitic magma composition, between the equilibrium (phase equilibrium modelling) and disequilibrium scenarios (experimental and real-world examples).

### **7.3 Future Research**

Further research into the 'fates' of entrained minerals in granitic magmas is essential. A number of key aspects relating to granitic magmas have not been included here due to time constraints and the pressure-temperature limitations of the experimental apparatus. One point of departure would be to look at varying the time scale of the experiments to determine the exact point at which fast-equilibrating minerals, such as plagioclase, begin to succumb to dissolution-precipitation mechanisms. Another relevant approach would be to run experiments at constant pressure, but to decrease the temperature conditions incrementally throughout the experimental run time. This would provide a more 'realistic' approach to determine the compositional and textural changes to 'peritectic' mineral phases in a progressively cooling magma. Finally, further experimental research into the 'fates' of peritectic minerals in an I-type magma during its ascent would be valuable, as the findings would either corroborate or challenge the findings of this research.

## References

- Agostini, C., Fortunati, A., Arzilli, F., Landi, P. and Carroll, M. (2013). Kinetics of crystal evolution as a probe to magmatism at Stromboli (Aeolian Archipelago, Italy). *Geochimica et Cosmochimica Acta*, 110, pp.135-151.
- Almeida, M., Macambira, M. and Oliveira, E. (2007). Geochemistry and zircon geochronology of the I-type high-K calc-alkaline and S-type granitoid rocks from southeastern Roraima, Brazil: Orosirian collisional magmatism evidence (1.97–1.96Ga) in central portion of Guyana Shield. *Precambrian Research*, 155(1-2), pp.69-97.
- Anderson, G.M. (2002) Stable and metastable equilibrium: The third constraint. *The Geochemical Society, Special Publications*. (7), pp. 181-187.
- Annen, C., Blundy, J and Sparks, R., (2006). The genesis of intermediate and silicic magmas in deep crustal hot zones. *Journal of Petrology*. 47 (3), pp. 505-539.
- Antunes, I., Neiva, A., Silva, M. and Corfu, F. (2008). Geochemistry of S-type granitic rocks from the reversely zoned Castelo Branco pluton (central Portugal). *Lithos*, 103(3-4), pp.445-465.
- Arzilli, F. and Carroll, M. (2013). Crystallization kinetics of alkali feldspars in cooling and decompression-induced crystallization experiments in trachytic melt. *Contributions to Mineralogy and Petrology*, 166(4), pp.1011-1027.
- Athari, S., Sepahi, A. and Moazzen, M. (2007). Petrology of leucocratic granitoids in the northwest of Iran with emphasis on leucocratic I-type granites from SW Saqqez. *Neues Jahrbuch für Mineralogie - Abhandlungen*, 184(2), pp.169-179.
- Barbarin, B. (1999). A review of the relationships between granitoid types, their origins and their geodynamic environments. *Lithos*. 46 (3). pp. 605--626.
- Beard, J., Ragland, P. and Crawford, M. (2005). Reactive bulk assimilation: A model for crust-mantle mixing in silicic magmas. *Geol*, 33(8), p.681.
- Best, M. (1982). *Igneous and metamorphic petrology*. San Francisco: Freeman.
- Broska, I. (2003). REE accessory minerals in the felsic silicic rocks of the west-Carpathians: their distribution, composition and stability. *Acta Mineralogica-Petrographica*. [Abstract]
- Brown, M. (2004). The mechanism of melt extraction from lower continental crust of orogens. *Transactions of the Royal Society of Edinburgh: Earth Sciences*, 95(1-2).
- Brown, M. (2013). Granite: From genesis to emplacement. *Geological Society of America Bulletin*.
- Carlson, W. (2006). Rates of Fe, Mg, Mn, and Ca diffusion in garnet. *American Mineralogist*, 91(1), pp.1-11.
- Carmichael, I., Turner, F. and Verhoogen, J. (1974). *Igneous petrology*. New York: McGraw-Hill.
- Castro, A. (2014). The off-crust origin of granite batholiths. *Geoscience Frontiers*, 5(1), pp.63-75.
- Castro, A., Patino Douce, A.E., Corretge, L.G., de la Rosa, J.D., El-Biad, M., El-Hmidi, H. (1999). Origin of peraluminous granites and granodiorites, Iberian massif, Spain: an experimental test of granite petrogenesis. *Contributions to Mineralogy and Petrology*. 135, pp. 255-276.
- Chappell, B. (1996). Magma Mixing and the Production of Compositional Variation within Granite Suites: Evidence from the Granites of Southeastern Australia. *Journal of Petrology*, 37(3), pp.449-470.
- Chappell, B. (1999). Aluminium saturation in I- and S-type granites and the characterization of fractionated haplogranites. *Lithos*, 46 (3), pp. 535--551.
- Chappell, B., Bryant, C., Wyborn, D., White, A. and Williams, I. (1998). High- and Low-Temperature I-type Granites. *Resource Geology*, 48 (4), pp. 225--



## REFERENCES

- 235.
- Chappell, B. and White, A. (2001). Two contrasting granite types: 25 years later. *Australian Journal of Earth Sciences*, 48(4), pp.489-499.
- Chappell, B. and White, A. (1974). Two contrasting granite types. *Pacific Geology*, 8, pp.173 -174.
- Chappell, B., White, A. and Wyborn, D. (1987). The Importance of Residual Source Material (Restite) in Granite Petrogenesis. *Journal of Petrology*, 28(6), pp.1111-1138. [Abstract]
- Clarke, D. (1981). The Mineralogy of Peraluminous Granites: A Review. *Canadian Mineralogist*, (19), pp. 3-17.
- Clemens, J. (2012). Granitic magmatism, from source to emplacement: a personal view. *Applied Earth Science*, 121(3), pp.107-136.
- Clemens, J. (2003). S-type granitic magmas—petrogenetic issues, models and evidence. *Earth-Science Reviews*, 61(1-2), pp.1-18.
- Clemens, J., Darbyshire, D. and Flinders, J. (2009a). Sources of post-orogenic calcalkaline magmas: The Arrochar and Garabal Hill–Glen Fyne complexes, Scotland. *Lithos*, 112(3-4), pp.524-542.
- Clemens, J., Helps, P. and Stevens, G. (2009b). Chemical structure in granitic magmas – a signal from the source?. *Earth and Environmental Science Transactions of the Royal Society of Edinburgh*, 100(1-2), pp.159-172.
- Clemens, J. and Mawer, C. (1992). Granitic magma transport by fracture propagation. *Tectonophysics*, 204(3-4), pp.339-360.
- Clemens, J. and Stevens, G. (2012). What controls chemical variation in granitic magmas?. *Lithos*, 134 pp. 317--329.
- Clemens, J., Stevens, G. and Farina, F. (2011). The enigmatic sources of I-type granites: the peritectic connexion. *Lithos*, 126 (3), pp. 174--181.
- Clemens, J. and Vielzeuf, D. (1987). Constraints on melting and magma production in the crust. *Earth and Planetary Science Letters*, 86(2-4), pp.287-306.
- Clemens, J. and Wall, V. (1981). Origin and crystallization of some peraluminous (S-type) granitic magmas. *The Canadian Mineralogist*, 19 (1), pp. 111—131.
- Clemens, J. and Wall, V. (1988). Controls on the mineralogy of S-type volcanic and plutonic rocks. *Lithos*, 21(1), pp.53-66.
- de Capitani, C. and Petrakakis, K. (2010). The computation of equilibrium assemblage diagrams with Theriak/Domino software. *American Mineralogist*, 95(7), pp.1006-1016.
- Diener, J. and Powell, R. (2011). Revised activity-composition models for clinopyroxene and amphibole. *Journal of Metamorphic Geology*, 30(2), pp.131-142.
- Donaldson, C. (1985). The Rates of Dissolution of Olivine, Plagioclase, and Quartz in a Basalt Melt. *Mineralogical Magazine*, 49(354), pp.683-693.
- Droop, G. (1987). A General Equation for Estimating Fe<sup>3+</sup> Concentrations in Ferromagnesian Silicates and Oxides from Microprobe Analyses, Using Stoichiometric Criteria. *Mineralogical Magazine*, 51(361), pp.431-435.
- Finger, F. and Steyrer, H. (1990). I-type granitoids as indicators of a late Paleozoic convergent ocean-continent margin along the southern flank of the central European Variscan orogen. *Geology*. 18 (12). pp. 1207--1210.
- Franke, W. (1989). Variscan plate tectonics in Central Europe—current ideas and open questions. *Tectonophysics*, 169(4), pp.221-228.
- Gardien, V., Thompson, A., Grujic, D. and Ulmer, P. (1995). Experimental melting of biotite + plagioclase + quartz ± muscovite assemblages and implications for crustal melting. *Journal of*

- Geophysical Research.*, 100(B8), pp.15581 – 15591.
- Giddings, J. (1991). *Unified separation science*. New York: Wiley.
- Gill, R. (2015). *Chemical Fundamentals of Geology and Environmental Geosciences*. 3rd ed. Sussex: Wiley Blackwell, pp.43-44.
- Glazner, A. (2007). Thermal limitations on incorporation of wall rock into magma. *Geol*, 35(4), p.319. [Abstract].
- Glazner, A., Bartley, J., Coleman, D., Gray, W. and Taylor, R. (2004). Are plutons assembled over millions of years by amalgamation from small magma chambers?. *GSA Today*, 14(4), pp.4 --11.
- Hammer, J. (2008). Experimental Studies of the Kinetics and Energetics of Magma Crystallization. *Reviews in Mineralogy and Geochemistry*, 69(1), pp.9-59.
- Harris, C., Faure, K., Diamond, R. E. and Scheepers, R. (1997). Oxygen and hydrogen isotope geochemistry of S-and I-type granitoids: the Cape Granite suite, South Africa. *Chemical geology*, 143 (1), pp. 95--114.
- Hine, R., Williams, I., Chappell, B. and White, A. (1978). Contrasts between I-and S-type of the Kosciusko Batholith. *Journal of the Geological Society of Australia*. 25 (3-4), pp. 219--234.
- Holland, T. and Powell, R. (2003). Activity composition relations for phases in petrological calculations: an asymmetric multicomponent formulation. *Contributions to Mineralogy and Petrology*, 145(4), pp.492-501.
- Hosseini, E., Ardalan, A., Emami, M. and Razavi, M. (2014). Mineral Chemistry and Thermobarometry of the Volcanic Rocks in Torud, Iran. *OJG*, 04(09), pp.425-435.
- Karsli, O., Dokuz, A., Uysal, İ., Aydin, F., Chen, B., Kandemir, R. and Wijbrans, J. (2010). Relative contributions of crust and mantle to generation of Campanian high-K calc-alkaline I-type granitoids in a subduction setting, with special reference to the Harşit Pluton, Eastern Turkey. *Contributions to Mineralogy and Petrology*, 160(4), pp.467-487.
- Kay, S., Godoy, E. and Jurtz, A. (2005). Episodic arc migration, crustal thickening, subduction erosion, and magmatism in the south-central Andes. *GSA Bulletin*. 117(1/2), pp. 67-88.
- Kemp, A., Hawkesworth, C., Foster, G., Paterson, B., Woodhead, J., Hergt, J., Gray, C. and Whitehouse, M. (2007). Magmatic and crustal differentiation history of granitic rocks from Hf-O isotopes in zircon. *Science*, 315 (5814), pp. 980--983.
- Koga, K. (2000). *Kinetic Processes of Mantle Minerals*. Ph.D. Massachusetts Institute of Technology.
- Lo Cascio, M., Liang, Y., Shimizu, N. and Hess, P. (2008). An experimental study of the grain-scale processes of peridotite melting: implications for major and trace element distribution during equilibrium and disequilibrium melting. *Contributions to Mineralogy and Petrology*, 156(1), pp.87-102.
- Maas, R., Nicholls, I. and Legg, C. (1997). Igneous and Metamorphic Enclaves in the S-type Deddick Granodiorite, Lachlan Fold Belt, SE Australia: Petrographic, Geochemical and Nd-Sr Isotopic Evidence for Crustal Melting and Magma Mixing. *Journal of Petrology*, 38(7), pp.815-841.
- McLeod, C., Davidson, J., Nowell, G. and de Silva, S. (2012). Disequilibrium melting during crustal anatexis and implications for modeling open magmatic systems. *Geology*, 40(5), pp.435-438.
- McCulloch, M. T. and Chappell, B. W. (1982). Nd isotopic characteristics of S-and I-type granites. *Earth and Planetary Science Letters*, 58 (1), pp. 51-64.
- McDonough, W. and Sun, S. (1995). The composition of the Earth. *Chemical Geology*, 120(3-4), pp.223-253.
- Metcalf, R., Smith, E., Walker, J., Reed, R. and Gonzales,

## REFERENCES

- D. (1995). Isotopic Disequilibrium among Commingled Hybrid Magmas: Evidence for a Two-Stage Magma Mixing-Commingling Process in the Mt. Perkins Pluton, Arizona. *The Journal of Geology*, 103(5), pp.509-527.
- Montel, J. and Vielzeuf, D. (1997). Partial melting of metagreywackes, Part II. Compositions of minerals and melts. *Contributions to Mineralogy and Petrology*, 128(2-3), pp.176-196.
- Moyen, J. and Stevens, G. (2006). Experimental constraints on TTG petrogenesis: implications for Archean geodynamics. *Archean geodynamics and environments*. pp.149-175.
- Nédélec, A., Bouchez, J. and Bowden, P. (2015). *Granites*. Oxford University Press. New York.
- Neilsen, C. and Sigurdsson, H. (1981). Quantitative methods for electron microprobe analysis of sodium in natural and synthetic glasses. *American Mineralogist*. 77, pp. 1242 – 1249.
- Nelson, S. and Montana, A. (1992). Sieve-textured plagioclase in volcanic rocks produced by rapid decompression. *American Mineralogist*. 77, pp. 1242 – 1249.
- O'Neil, J. and Chappell, B. (1977). Oxygen and hydrogen isotope relations in the Berridale batholith. *Journal of the Geological Society*. 133 (6). pp. 559--571.
- Paterson, S., and Ducea, M. (2015). Arc magmatic tempos: gathering the evidence. *Elements*, 11(2), pp.91-98.
- Patiño-Douce, A. and Beard, J. (1996). Effects of P, f (O<sub>2</sub>) and Mg/Fe Ratio on Dehydration Melting of Model Metagreywackes. *J Petrology*, 37(5), pp.999-1024.
- Pearce, J. (1996). Sources and settings of granitic rocks. *Episodes*. 19 (4). pp. 120 -125.
- Pearce, J., Harris, N. and Tindle, A. (1984). Trace Element Discrimination Diagrams for the Tectonic Interpretation of Granitic Rocks. *Journal of Petrology*, 25(4), pp.956-983.
- Petford, N., Cruden, A.R, McCaffrey, K.J.W and Vigneresse, J.L. (2000) Granite magma formation, transport and emplacement in the Earth's crust. *Nature*, 408 (6813), pp. 669-673.
- Piwinskii, A. (1968). Experimental Studies of Igneous Rock Series Central Sierra Nevada Batholith, California. *The Journal of Geology*, 76(5), pp.548-570.
- Putnis, A. (2014). Why Mineral Interfaces Matter. *Science*, 343(6178), pp.1441-1442.
- Putnis, A. (2009). Mineral Replacement Reactions. *Reviews in Mineralogy and Geochemistry*, 70(1), pp.87-124.
- Putnis, A. (2002). Mineral replacement reactions: from macroscopic observations to microscopic mechanisms. *Mineralogical Magazine*, 66(5), pp.689-708.
- Ratajeski, K. and Sisson, T.W. (1999) Loss of iron to gold capsules in rock melting experiments. *American Mineralogist*. 84, pp. 1521--1527.
- Reid, Jr., J., Murray, D., Hermes, O. and Steig, E. (1993). Fractional crystallization in granites of the Sierra Nevada: How important is it?. *Geol*, 21(7), pp. 587 -- 590.
- Roberts, M. P. and Clemens, J. D. (1993). Origin of high-potassium, talc-alkaline, I-type granitoids. *Geology*, 21 (9), pp. 825--828.
- Rudnick, R. (1992). Restites, Eu anomalies and the lower continental crust. *Geochimica et Cosmochimica Acta*, 56(3), pp.963-970.
- Ruiz-Agudo, E., Putnis, C. and Putnis, A. (2014). Coupled dissolution and precipitation at mineral–fluid interfaces. *Chemical Geology*, 383, pp.132-146.
- Rutherford, M. (2008). Magma Ascent Rates. *Reviews in Mineralogy and Geochemistry*, 69(1), pp.241-271.
- Samson, I., Anderson, A. and Marshall, D. (2003). *Fluid inclusions*. Ottawa, Ont., Canada: Mineralogical Association of Canada.

- Scheepers, R. (1995). Geology, geochemistry and petrogenesis of Late Precambrian S-, I- and A-type granitoids in the Saldania belt, Western Cape Province, South Africa. *Journal of African Earth Sciences*, 21 (1), pp. 35—58.
- Scheepers, R. and Poujal, M. (2002). U-Pb zircon age of Cape Granite Suite ignimbrites: characteristics of the last phases of the Saldanian magmatism. *South African Journal of Geology*, 105 (2), pp. 163—178.
- Sen, C. and Dunn, T. (1994). Dehydration melting of a basaltic composition amphibolite at 1.5 and 2.0 GPa: implications for the origin of adakites. *Contrib. Mineral. and Petrol.*, 117(4), pp.394-409.
- Soesoo, A. (2000). Fractional crystallization of mantle-derived melts as a mechanism for some I-type granite petrogenesis: an example from Lachlan Fold Belt, Australia. *Journal of the Geological Society*, 157(1), pp.135-149.
- Stephens, W. (2001). Polycrystalline amphibole aggregates (clots) in granites as potential I-type restite: An ion microprobe study of rare-earth distributions. *Australian Journal of Earth Sciences*, 48(4), pp.591-601.
- Stevens, G. and Clemens, J. (in press). The 'DNA' of granite magmas. *Unpublished*. pp. 1--13
- Stevens, G., Villaros, A. and Moyen, J. (2007). Selective peritectic garnet entrainment as the origin of geochemical diversity in S-type granites. *Geology*, 35 (1), pp. 9--12.
- Swanson, S. (1977). Relation of nucleation and crystal growth rate to the development of granitic textures. *American Mineralogist*, 62, pp. 966 -978.
- Taylor, J. and Stevens, G. (2010). Selective entrainment of peritectic garnet into S-type granitic magmas: evidence from Archaean mid-crustal anatexites. *Lithos*, 120(3), pp.277--292.
- Thompson, A. and Connolly, J. (1995). Melting of the continental crust: Some thermal and petrological constraints on anatexis in continental collision zones and other tectonic settings. *J. Geophys. Res.*, 100(B8), p.15565.
- Tropper, P. and Hauzenberger, C. (2015). How well do pseudosection calculations reproduce simple experiments using natural rocks: an example from high-P high-T granulites of the Bohemian Massif. *Austrian Journal of Earth Sciences*, 108(1), pp.123-138.
- Tropper, P., Konzett, J. and Finger, F. (2005). Experimental constraints on the formation of high-P/high-T granulites in the Southern Bohemian Massif. *European Journal of Mineralogy*, 17(2), pp.343-356.
- Vernon, R. (2004). *A practical guide to rock microstructure*. Cambridge, UK: Cambridge University Press.
- Vernon, R. H. (2007). Problems in identifying restite in S-type granites of southeastern Australia, with speculations on sources of magma and enclaves. *The Canadian Mineralogist*, 45 (1), pp. 147--178.
- Villaseca, C., Bellido, F., Pérez-Soba, C. and Billström, K. (2009). Multiple crustal sources for post-tectonic I-type granites in the Hercynian Iberian Belt. *Mineralogy and Petrology*, 96(3-4), pp.197-211.
- Villaros, A., Stevens, G. and Buick, I. S. (2009a). Tracking S-type granite from source to emplacement: clues from garnet in the Cape Granite Suite. *Lithos*, 112 (3), pp. 217--235.
- Villaros, A., Stevens, G., Moyen, F., Buick, I. S. (2009b). The trace element compositions of S-type granites: evidence for disequilibrium melting and accessory phase entrainment in the source. *Contributions to Mineral Petrology*, 158 (4), pp. 543--561.
- White, A. and Chappell, B. (1977). Ultrametamorphism and granitoid genesis. *Tectonophysics*, 43(1-2), pp. 7-22.
- White, A., Chappell, B. and Wyborn, D. (1999). Application of the Restite Model to the Deddick

## REFERENCES

- Granodiorite and its Enclaves --a Reinterpretation of the Observations and Data of Maas et al. (1997). *Journal of Petrology*, 40(3), pp.413-421.
- White, R., Pomroy, N. and Powell, R. (2005). An in situ metatexite-diatexite transition in upper amphibolite facies rocks from Broken Hill, Australia. *Journal of Metamorphic Geology*, 23(7), pp.579-602.
- White, R., Powell, R. and Clarke, G. (2002). The interpretation of reaction textures in Fe-rich metapelitic granulites of the Musgrave Block, central Australia: constraints from mineral equilibria calculations in the system K<sub>2</sub>O-FeO-MgO-Al<sub>2</sub>O<sub>3</sub>-SiO<sub>2</sub>-H<sub>2</sub>O-TiO<sub>2</sub>-Fe<sub>2</sub>O<sub>3</sub>. *Journal of Metamorphic Geology*, 20(1), pp.41-55.
- White, R., Powell, R. and Holland, T. (2007). Progress relating to calculation of partial melting equilibria for metapelites. *Journal of Metamorphic Geology*, 25(5), pp.511-527.
- White, R., Powell, R., Holland, T., and Worley, B. (2000). The effect of TiO<sub>2</sub> and Fe<sub>2</sub>O<sub>3</sub> on metapelitic assemblages at greenschist and amphibolite facies conditions: mineral equilibria calculations in the system K<sub>2</sub>O-FeO-MgO-Al<sub>2</sub>O<sub>3</sub>-SiO<sub>2</sub>-H<sub>2</sub>O-TiO<sub>2</sub>-Fe<sub>2</sub>O<sub>3</sub>. *Journal of Metamorphic Geology*, 18(5), pp.497-511.
- White, R., Stevens, G. and Johnson, T. (2011). Is the Crucible Reproducible? Reconciling Melting Experiments with Thermodynamic Calculations. *Elements*, 7(4), pp.241-246.
- Whitney, J. (1988). The origin of granite: The role and source of water in the evolution of granitic magmas. *Geological Society of America Bulletin*, 100(12), pp.1886-1897.
- Whitney, D. and Evans, B. (2010). Abbreviations for names of rock-forming minerals. *American Mineralogist*, 95(1), pp. 185-187.
- Yakymchuk, C., Horhonen, F., and Brown, M. (2011). Decompression melting in tectonics: Where's the melt? *Mineralogical Magazine*, 75(3), pp. 2200.
- Zhu, C. and Anderson, G. (2002). *Environmental applications of geochemical modeling*. Cambridge: Cambridge University Press.
- Zorpi, M., Coulon, C., Orsini, J. and Cocirca, C. (1989). Magma mingling, zoning and emplacement in calc-alkaline granitoid plutons. *Tectonophysics*, 157(4), pp.315-329.

## Appendix

### Zeiss® EVO MA 15 Scanning Electron Microscope Mineral Standards

<b>Garnet</b>	<b>STANDARD</b>	<b>MINERAL FORMULA</b>
<i>SiO<sub>2</sub></i>	Pyrope Garnet	Mg <sub>3</sub> Al <sub>2</sub> Si <sub>3</sub> O <sub>12</sub>
<i>TiO<sub>2</sub></i>	Biotite	K(Mg,Fe) <sub>3</sub> AlSi <sub>3</sub> O <sub>10</sub> (OH) <sub>2</sub>
<i>Al<sub>2</sub>O<sub>3</sub></i>	Pyrope Garnet	Mg <sub>3</sub> Al <sub>2</sub> Si <sub>3</sub> O <sub>12</sub>
<i>FeO</i>	Ilmenite	FeTiO <sub>3</sub>
<i>MnO</i>	Ilmenite	FeTiO <sub>3</sub>
<i>MgO</i>	Pyrope Garnet	Mg <sub>3</sub> Al <sub>2</sub> Si <sub>3</sub> O <sub>12</sub>
<i>CaO</i>	Diopside	CaMgSi <sub>2</sub> O <sub>6</sub>
<i>Na<sub>2</sub>O</i>	Anorthite 65	CaAl <sub>2</sub> Si <sub>2</sub> O <sub>8</sub>
<i>K<sub>2</sub>O</i>	Biotite	K(Mg,Fe) <sub>3</sub> AlSi <sub>3</sub> O <sub>10</sub> (OH) <sub>2</sub>

<b>Plagioclase</b>	<b>STANDARD</b>	<b>MINERAL FORMULA</b>
<i>SiO<sub>2</sub></i>	Albite/Sanidine	NaAlSi <sub>3</sub> O <sub>8</sub> / KAlSi <sub>3</sub> O <sub>8</sub>
<i>TiO<sub>2</sub></i>	Biotite/Ilmenite	K(Mg,Fe) <sub>3</sub> AlSi <sub>3</sub> O <sub>10</sub> (OH) <sub>2</sub> / FeTiO <sub>3</sub>
<i>Al<sub>2</sub>O<sub>3</sub></i>	Anorthite 65	CaAl <sub>2</sub> Si <sub>2</sub> O <sub>8</sub>
<i>FeO</i>	Ilmenite	FeTiO <sub>3</sub>
<i>MgO</i>	Pyrope Garnet	Mg <sub>3</sub> Al <sub>2</sub> Si <sub>3</sub> O <sub>12</sub>
<i>CaO</i>	Anorthite 65/Diopside	CaAl <sub>2</sub> Si <sub>2</sub> O <sub>8</sub> / CaMgSi <sub>2</sub> O <sub>6</sub>
<i>Na<sub>2</sub>O</i>	Albite	NaAlSi <sub>3</sub> O <sub>8</sub>
<i>K<sub>2</sub>O</i>	Sanidine	KAlSi <sub>3</sub> O <sub>8</sub>

<b>Pyroxene</b>	<b>STANDARD</b>	<b>MINERAL FORMULA</b>
<i>SiO<sub>2</sub></i>	Sanidine	KAlSi <sub>3</sub> O <sub>8</sub>
<i>TiO<sub>2</sub></i>	Kaersutite	NaCa <sub>2</sub> (Mg <sub>3</sub> Ti <sup>4+</sup> Al)Si <sub>6</sub> Al <sub>2</sub> O <sub>22</sub> (OH) <sub>2</sub>
<i>Al<sub>2</sub>O<sub>3</sub></i>	Spodumene	LiAlSi <sub>2</sub> O <sub>6</sub>
<i>FeO</i>	Almandine Garnet	Fe <sub>3</sub> Al <sub>2</sub> Si <sub>3</sub> O <sub>12</sub>
<i>MnO</i>	Almandine Garnet	Fe <sub>3</sub> Al <sub>2</sub> Si <sub>3</sub> O <sub>12</sub>
<i>MgO</i>	Diopside/Olivine	CaMgSi <sub>2</sub> O <sub>6</sub> /
<i>CaO</i>	Diopside	CaMgSi <sub>2</sub> O <sub>6</sub>
<i>Na<sub>2</sub>O</i>	Jadeite	NaAlSi <sub>2</sub> O <sub>6</sub>
<i>K<sub>2</sub>O</i>	Sanidine	KAlSi <sub>3</sub> O <sub>8</sub>

## APPENDIX

<b>Biotite</b>	<b>STANDARD</b>	<b>MINERAL FORMULA</b>
<i>SiO<sub>2</sub></i>	Pyrope Garnet	Mg <sub>3</sub> Al <sub>2</sub> Si <sub>3</sub> O <sub>12</sub>
<i>TiO<sub>2</sub></i>	Biotite	K(Mg,Fe) <sub>3</sub> AlSi <sub>3</sub> O <sub>10</sub> (OH) <sub>2</sub>
<i>Al<sub>2</sub>O<sub>3</sub></i>	Pyrope Garnet	Mg <sub>3</sub> Al <sub>2</sub> Si <sub>3</sub> O <sub>12</sub>
<i>FeO</i>	Almandine Garnet	Fe <sub>3</sub> Al <sub>2</sub> Si <sub>3</sub> O <sub>12</sub>
<i>MgO</i>	Pyrope Garnet	Mg <sub>3</sub> Al <sub>2</sub> Si <sub>3</sub> O <sub>12</sub>
<i>CaO</i>	Anorthite 65	CaAl <sub>2</sub> Si <sub>2</sub> O <sub>8</sub>
<i>Na<sub>2</sub>O</i>	Anorthite 65	CaAl <sub>2</sub> Si <sub>2</sub> O <sub>8</sub>
<i>K<sub>2</sub>O</i>	Biotite	K(Mg,Fe) <sub>3</sub> AlSi <sub>3</sub> O <sub>10</sub> (OH) <sub>2</sub>

<b>Ilmenite</b>	<b>STANDARD</b>	<b>MINERAL FORMULA</b>
<i>SiO<sub>2</sub></i>	Pyrope Garnet	Mg <sub>3</sub> Al <sub>2</sub> Si <sub>3</sub> O <sub>12</sub>
<i>TiO<sub>2</sub></i>	Ilmenite	FeTiO <sub>3</sub>
<i>Al<sub>2</sub>O<sub>3</sub></i>	Pyrope Garnet	Mg <sub>3</sub> Al <sub>2</sub> Si <sub>3</sub> O <sub>12</sub>
<i>FeO</i>	Ilmenite	FeTiO <sub>3</sub>
<i>MnO</i>	Ilmenite	FeTiO <sub>3</sub>
<i>MgO</i>	Pyrope Garnet	Mg <sub>3</sub> Al <sub>2</sub> Si <sub>3</sub> O <sub>12</sub>

<b>Quartz</b>	<b>STANDARD</b>	<b>MINERAL FORMULA</b>
<i>SiO<sub>2</sub></i>	Quartz	SiO <sub>2</sub>

<b>Melt</b>	<b>STANDARD</b>	<b>MINERAL FORMULA</b>
<i>SiO<sub>2</sub></i>	Quartz	SiO <sub>2</sub>
<i>TiO<sub>2</sub></i>	Biotite	K(Mg,Fe) <sub>3</sub> AlSi <sub>3</sub> O <sub>10</sub> (OH) <sub>2</sub>
<i>Al<sub>2</sub>O<sub>3</sub></i>	Anorthite 65	CaAl <sub>2</sub> Si <sub>2</sub> O <sub>8</sub>
<i>FeO</i>	Biotite	K(Mg,Fe) <sub>3</sub> AlSi <sub>3</sub> O <sub>10</sub> (OH) <sub>2</sub>
<i>MnO</i>	Biotite	K(Mg,Fe) <sub>3</sub> AlSi <sub>3</sub> O <sub>10</sub> (OH) <sub>2</sub>
<i>MgO</i>	Anorthite 65	CaAl <sub>2</sub> Si <sub>2</sub> O <sub>8</sub>
<i>CaO</i>	Anorthite 65	CaAl <sub>2</sub> Si <sub>2</sub> O <sub>8</sub>
<i>Na<sub>2</sub>O</i>	Albite	NaAlSi <sub>3</sub> O <sub>8</sub>
<i>K<sub>2</sub>O</i>	Sanidine	KAlSi <sub>3</sub> O <sub>8</sub>

\*Reference materials (qtz/plg) were analysed intermittently throughout the melt analysis to test beam stability and ensure accurate melt results